LMSC-D678772

DEVELOPMENT OF ADVANCED ALUMINUM ALLOYS FROM RAPIDLY SOLIDIFIED POWDERS FOR AEROSPACE STRUCTURAL APPLICATIONS

R. E. Lewis
Lockheed Palo Alto Research Laboratory
3251 Hanover Street
Palo Alto, California 94304

September 1979

Interim Technical Report for Period March 1979 – September 1979

Approved for public release; distribution unlimited.

Sponsored by
DEFENSE ADVANCED RESEARCH PROJECTS AGENCY
Arlington, Virginia 22209

Monitored by
AIR FORCE MATERIALS LABORATORY
AIR FORCE WRIGHT AERONAUTICAL LABORATORIES
AIR FORCE SYSTEMS COMMAND
Wright-Patterson Air Force Base, Ohio 45433

"The views and conclusions contained in this document are those of the authors and should not be interpreted as representing the offical policies, either expressed or implied, of the Defense Advanced Research Projects Agency or the U. S. Government."

UNCLASSIFIED
SECURITY CLASSIFICATION OF THIS PAGE (When Data Entered)

REPORT DOCUMENTATION PAGE

READ INSTRUCTIONS BEFORE COMPLETING FORM

1. REPORT NUMBER	2. GOVT ACCESSION NO. / 3. RECIPIENT'S CATALOG NUMBER
4. TITLE (and Subtitle): DEVELOPMENT OF ADVANCED ALUMINUM ALLOYS FROM RAPIDLY SOLIDIFIED POWDERS FOR AEROSPACE STRUCTURAL APPLICATIONS.	5. TYPE OF REPORT & PERIOD COVERED: Interim Technical Report, for Period 5 Mar[illegible]-4 Sept[illegible]79
	6. PERFORMING ORG. REPORT NUMBER: LMSC-D678772
7. AUTHOR(s): R. E. Lewis	8. CONTRACT OR GRANT NUMBER(s): ARPA Order 3575; Contract F33615-78-C-5203; ARPA Order-3575
9. PERFORMING ORGANIZATION NAME AND ADDRESS: Lockheed Palo Alto Research Laboratory, Lockheed Missiles & Space Company, Inc., 3251 Hanover Street, Palo Alto, CA 94304	10. PROGRAM ELEMENT, PROJECT, TASK AREA & WORK UNIT NUMBERS: Project 3575
11. CONTROLLING OFFICE NAME AND ADDRESS: Defense Advanced Research Projects Agency (DoD), 1400 Wilson Boulevard, Arlington, VA 22209	12. REPORT DATE: September 1979 / 13. NUMBER OF PAGES: 133
14. MONITORING AGENCY NAME & ADDRESS (if different from Controlling Office): Air Force Materials Laboratory, Air Force Systems Command, Wright-Patterson Air Force Base, Ohio 45433	15. SECURITY CLASS. (of this report): UNCLASSIFIED / 15a. DECLASSIFICATION DOWNGRADING SCHEDULE

16. DISTRIBUTION STATEMENT (of this Report)

Approved for public release; distribution unlimited.

17. DISTRIBUTION STATEMENT (of the abstract entered in Block 20, if different from Report)

18. SUPPLEMENTARY NOTES

Other principal contributors are: I. G. Palmer and D. D. Crooks, LMSC, Inc., W. Cebulak. H. Paris, and F. Billman, ALCOA; E. A. Starke, Jr., E. E. Underwood. T. H. Sanders, Jr. and R. Crooks, Georgia Institute of Technology; and E. Rhodes, G. Wald, and R. Simenz, Lockheed-California Company.

19. KEY WORDS (Continue on reverse side if necessary and identify by block number)

aerospace structures	Al-Li-Mn	microstructures
rapidly solidified powders	Al-Li-Zr	mechanical properties
aluminum alloy	Al-Fe-Ni-Co	methodology for predicting weight savings
Al-Li	Al-Mn-Si	Al-Li-Fe-Ni
Al-Cu-Li	alloy development	Al-Li-Fe-Co

20. ABSTRACT (Continue on reverse side if necessary and identify by block number)

Advanced aluminum alloys are being developed that will provide major payoffs in terms of weight savings for new aerospace structures. The two property goals are: (1) a 30-percent increase in modulus of elasticity-to-density ratio, and (2) a 20-percent increase in modulus of elasticity-to-density ratio plus a 20-percent increase in strength-to-density ratio, when compared to Al 7075-T76 and without a significant loss in other properties important for structural applications.

The program is organized into three phases: 1 – a fundamental alloy and process development study; 2 – scale-up of two best alloys and evaluation of mill product forms;

DD FORM 1 JAN 73 1473 EDITION OF 1 NOV 65 IS OBSOLETE

210 118

UNCLASSIFIED
SECURITY CLASSIFICATION OF THIS PAGE (When Data Entered)

3 – design evaluation involving selected redesign of aerospace components, analysis of payoffs, and recommendations for manufacturing technology development. Phase 1 activity, to be completed in the first two years, is organized into four Tasks: 1 – development of advanced aluminum alloys containing lithium; 2 – development of advanced aluminum alloys that do not contain lithium; 3 – quantitative microstructural analyses and mechanical property correlations; 4 – study of aerospace structural applications for advanced aluminum alloys including development and application of a method for predicting weight savings. Phase 1 activity is described below; Phases 2 and 3 have not been initiated.

In the development of aluminum alloys containing lithium, argon atomized splat particulate was prepared for the eight first-iteration alloys. The first four contain 3 wt % Li, 2 to 4 wt % Cu, and Zr or Mn as grain refiners, and the second four contain 3 wt % Li and approximately 1 wt % of various dispersoid-forming elements. Extrusions were prepared for each alloy, and longitudinal tensile properties were obtained for peak-aged material. Modulus-to-density ratios were all about 30 percent higher than 7075-T76, and strength was close to 7075-T76 typical values for seven of the alloys. Tensile elongation was 2.7 to 5.7 percent. Metallographic and fractographic studies of these alloys are being conducted to relate microstructure and properties. Procedures have been identified for evaluation to obtain improvement in properties, particularly ductility.

In the development of nonlithium-containing aluminum alloys, a total of 23 lots of air and argon atomized splat particulate and air atomized fine powder was prepared for the eight first-iteration alloys. The first four alloys contain Fe, Ni, and Co, the second four contain Mn or Mn and Si. Suitable cold compaction procedures were developed. Thermal stability studies were conducted to provide a basis for planning hot compaction and extrusion processing. Microstructural and compositional studies of the splat and powder have been conducted.

Microstructures, aging behavior, tensile properties, and fracture features of PM Al-Li splat alloys and IM alloys of similar composition were compared. Crystallographic textures (pole figures) of PM and IM Al-Li extrusions were obtained; the results indicate that at a low (8:1) extrusion ratio the PM alloys develop sharp, well-defined texture. Higher extrusion ratios are probably required to develop optimum bonding of the splat particulate interfaces.

The model for prediction of weight savings for application of advanced aluminum alloys was adapted to an advanced tactical fighter (ATF). The effect of secondary structural criteria on payoff in terms of weight savings was also evaluated. The minimum acceptable values of damage tolerance assessment properties required for compression critical structures were derived for fighter, patrol, and transport aircraft.

FOREWORD

This Interim Technical Report was prepared by Lockheed Missiles & Space Company, Inc., Palo Alto, California, under USAF Contract F33615-78-C-5203. The work is sponsored by the Defense Advanced Research Projects Agency (DoD), Arlington, Virgina, under ARPA Order 3575 and is administered by the Air Force Materials Laboratory, Wright-Patterson Air Force Base, Ohio, with Dr. Lawrence R. Bidwell (AFML/LLS) as Program Manager.

This report covers the period 5 March 1979 to 4 September 1979 as part of an ongoing program to develop advanced aluminum alloys from rapidly solidified powders for aerospace structural applications.

Mr. R. E. Lewis of LMSC, is the Principal Investigator on this program. Other principal contributors to this report are as follows:

I. G. Palmer and D. D. Crooks – LMSC
Section 2.1, Development of Alloys Containing Lithium

W. Cebulak, H. Paris, and F. Billman – ALCOA Laboratories
Section 2.2, Development of Nonlithium-Containing Alloys

E. A. Starke, Jr., E. E. Underwood, R. Crooks, and T. H. Sanders
Georgia Institute of Technology
Section 2.3, Quantitative Microstructural Analysis and Mechanical Property Correlations

E. Rhodes, G. Wald, and R. Simenz – Lockheed-California Co.
Section 2.4, Application Studies
Appendix A: Minimum Property Requirements for Highly Compression-Loaded Structures

We wish to thank Dr. T. E. Tietz, Manager of the Metallurgy and Composites Laboratory, LMSC, for his helpful guidance in the conduct of this study. We wish to also thank Drs. L. R. Bidwell (AFML), E. C. van Reuth, and A. Bement (DARPA) for their guidance and support of the subject study.

SUMMARY

Advanced aluminum alloys are to be developed that will provide major payoffs for important new aircraft, spacecraft, and missile systems in the next decade. Payoffs will result from weight savings of structural components which, in turn, lead to increased range, payload, service life, and decreased life-cycle cost. Recently conducted feasibility and design tradeoff studies provide a basis for selecting certain property goals for improved aluminum alloys that will result in significant weight savings. These property goals are as follows:

- Goal A. Specific Elastic Modulus: 33.1 $MNmkg^{-1}$ (133×10^6 in. *)
- Goal B. Specific Elastic Modulus: 30.4 $MNmkg^{-1}$ (122×10^6 in. *)
  Specific Yield Strength: 198 $kNmkg^{-1}$ (796×10^3 in. *)

OBJECTIVE

The objective of this program is to develop advanced aluminum alloys from rapidly solidified powders that meet specific property goals. In addition, the program is to establish a metallurgical basis suitable for manufacturing scaleup and application to new weapon systems.

SCOPE

The program is divided into three phases, each consisting of a number of tasks. Phase 1 involves fundamental alloy development studies and consolidation process development and optimization. The most promising alloys are to be selected, produced in simple mill form, and evaluated in Phase 2. Phase 3 will be a design evaluation involving selected redesign of aerospace components, analysis of payoffs, and recommendations for manufacturing technology.

---

*Units are actually (lbf/lbm) in.

The effort during the first two years is devoted solely to Phase 1.

TECHNICAL PROGRESS

Summary of activity to date for this program follows:

- TASK 1, Development of Aluminum Alloys Containing Lithium

  A sufficient amount, 125 kg (276 lb) in total, of argon atomized splat particulate was prepared for evaluation of the eight first-iteration alloys. all containing approximately 3 wt % Li and either 2 to 4 wt % Cu or approximately 1 wt % of various dispersoid-forming elements. Melt compositions along with size distribution and morphology of the splat have been obtained; microstructure of some of the alloys in splat form has been characterized. Extrusions have been prepared from unsegregated splat for all eight alloys, and mechanical and physical properties were measured for the aged to peak-hardness condition. Metallographic and fractographic studies of these alloys have been conducted to relate microstructure and properties. Procedures have been identified for evaluation to obtain improvement in properties, particularly ductility.

- TASK 2. Development of Nonlithium-Containing Aluminum Alloys

  A total of 1112 kg (2452 lb) of powder and splat particulate was prepared for the eight first-iteration alloys, and include both air and argon atomized splat and air atomized powder lots. These include Fe-Ni-Co, Mn. or Mn + Si alloying additions. Melt compositions along witn screen fraction analysis, morphology and microstructure of the splat and atomized powder have been obtained. Thermal stability of the rapidly solidified alloys was studied by Guinier analysis and transmission electron microscopy of aged particulate. The results of this study provide the basis to plan hot pressing and extrusion thermal cycles. Cold compaction of the various alloys was successfully accomplished.

- TASK 3. Quantitative Microstructural Analysis and Mechanical Property Correlations

  A preliminary investigation of microstructures, mechanical behavior, and other properties was undertaken for two alloys (Al-4Cu-3Li and Al-3Li-1.5Mn) extruded from splat particulate, and selected comparisons made with comparable ingot metallurgy material, when possible. Comparisons were made of grain size and shape, crystallographic texture (pole figures), and aging response (hardness versus aging time). Tensile tests were conducted of the Al-Cu-Li alloy, and fractographic features were analyzed. Auger electron spectroscopy of fracture surfaces of IM and PM Al-Li-Mn alloys, broken in situ, was performed.

- TASK 4. Application Studies

  The model for prediction of weight saving in aircraft by application of advanced aluminum alloys was adapted to an advanced tactical fighter (ATF). The effect of secondary structural material property criteria on payoff in terms of weight savings was also evaluated. The minimum acceptable values of damage tolerance assessment (DADTA) properties required for compression critical structures were derived for fighter, patrol. and transport aircraft.

IMPORTANT FINDINGS AND CONCLUSIONS

Melting and atomization to produce splat or fine atomized powder was readily achieved for 15 of the first 16 alloys. both with and without lithium. One alloy, Al-3Li-1Zr, posed significant difficulties because of the high chemical activity in the liquid state and incomplete solubility of Zr at practical melt temperatures.

From metallographic examination of the alloy splats, rapid cooling rates from 10^6 to over 10^7 Ks^{-1} appear to have been achieved. In the Al-Fe-Ni-Co, Al-Mn, and Al-Mn-Si alloys, a number of unique solidification features and phases have been produced by the nonequilibrium solidification conditions.

Examination of particulate in the splat lots reveals the presence of two types of non-splat particles that have not solidified as rapidly as the splat and probably should be removed before subsequent consolidation is performed. The first type is found primarily in the coarsest screen fractions and has a thick oxide surface layer and relatively coarse microstructure. The second type is found in the fine screen fractions and has a thicker oxide film and coarser microstructure than the splat. Most of these particles can be removed by rejecting +8 and -100 or -200 size screen fractions.

The first eight Al-Li alloys in the extruded and peak aged condition exhibit a tensile modulus-to-density ratio 26 to 39 percent higher than 7075-T76, as was expected. The longitudinal tensile yield and ultimate strengths are between 82 and 103 percent of 7075-T76 typical values, except the Al-3Li-0.5Fe-0.5Co alloy which on the same basis exhibited 68 percent yield and 77 percent ultimate strength. Tensile elongation was 2.7 to 5.7 percent, where the minimum goal is 7 percent. For these alloys, four steps have been identified for evaluation to improve the properties, expecially tensile ductility:

- Removal of majority of nonsplat particles by screening
- Higher hot pressing temperatures and pressures
- Higher extrusion ratios
- Underaging and overaging heat treatments

Cold compaction of the lithium-containing splat and the nonlithium-containing fine atomized powder alloys is readily achieved. The nonlithium-containing alloys in splat form do not cold compact by wet-bag isotatic techniques but can be satisfactorily compacted in a steel die using a bottom knockout.

Development of a random texture in Al-Li PM splat alloy extrusions is not likely to be achieved, as sharp, well-defined crystallographic textures were found in two alloys extruded at only an 8:1 reduction ratio. These textures are comparable to those developed in an IM alloy extrusion of similar composition, extruded at a 35:1 reduction ratio.

An extrusion ratio of 8:1 for the lithium-containing splat alloys may be inadequate to obtain optimum interparticle bonding, and higher extrusion ratios may be required to disrupt the oxide particle networks corresponding to splat particulate interfaces.

The relationship between weight savings and change in strength, stiffness, fatigue, or toughness properties for an advanced tactical fighter was found to be similar to that previously derived for a patrol aircraft. For either type aircraft, an optimum combination of properties meeting either contract goal A or B will result in a weight savings of approximately 14 percent.

CONTENTS

ILLUSTRATIONS

TABLES

Section 1
INTRODUCTION

1.1 IMPROVED STRUCTURAL MATERIAL NEEDS FOR AEROSPACE SYSTEMS IN THE NEXT DECADE

Three major new aerospace systems, to be developed in the next decade, will have significantly advanced military capabilities. They are an Advanced Tactical Fighter (Air Force), Vertical/Short Takeoff and Landing Reconnaissance Airplane (Navy), and Advanced Fleet Ballistic Missile (Navy). In each of these, structural materials exhibiting selectively improved properties are needed to realize the desired range, payload, and service-life improvements.

To achieve those property goals that will have a maximum payoff in these new systems, design tradeoff and material development studies have been and are being performed. These studies include advanced aluminum alloys, titanium alloys, and composites. Two important considerations in these studies are pertinent to the subject work reported herein:

(1) Improved aluminum alloys are of major interest to aerospace manufacturers because of the extensive existing manufacturing technology and capability directly suitable for this class of alloys.
(2) The development of improved aluminum alloys that exhibit significantly higher stiffness and/or strength properties has been shown to be technically feasible.

The following subsection highlights recently completed and some ongoing design tradeoff studies that provide a basis for selecting property goals for this alloy/process development program.

1.2 PAYOFFS IN SELECTED AEROSPACE SYSTEMS

1.2.1 Advanced Tactical Fighter

As part of an ongoing study* for the U.S. Air Force for air-to-surface technology in 1985, one aerospace manufacturer analyzed a close-coupled canard supersonic fighter-interceptor aircraft. Analysis was made of payoffs resulting from application of advanced stiffness aluminum alloys, advanced aluminum powder metal alloys such as CT-90 and CT-91, textured titanium, graphite-epoxy composites, FP-aluminum composites, low-cost hybrid composites, beta titanium isothermally forged, and low-temperature formable titanium sheet. These advanced materials were included in the study on the assumption that they would be available by 1985, provided that appropriate development and scaleup attention is directed to them.

A high-stiffness aluminum alloy exhibiting a 30 percent increase in modulus-to-density ratio was identified as the best choice for a number of major structural components. Weight saved and related cost figures for these components were estimated, compared with aluminum alloys commercially available in 1975. The weight saved was projected to a life-cycle cost savings of $469,000 per airplane. These savings were attributed to increased life as well as reduced maintenance and inspection.

The life-cycle cost savings result in a projected total savings of $234 million when applied to a fleet of 500 airplanes. Of the advanced materials concepts considered, the highest payoff 1985 technology identified was the high-modulus, low-density advanced aluminum alloy. Although advanced composites were found to offer competitive weight savings for many complex components such as the fuselage section, they were not recommended for development for such applications because of the high fabrication costs involved, estimated to be more than six times higher than for advanced aluminum alloys.

---

*Advance information was provided by the U. S. Air Force Materials Laboratory, Wright-Patterson AFB, Ohio.

1.2.2 Vertical/Short Takeoff and Landing Airplane

In the preliminary design tradeoff studies of a recently completed contract investigating the feasibility of developing advanced aluminum alloys, the following property goals were considered and weight savings calculated for each of the aluminum alloy major components in the airframe (Ref. 1). One alloy was assumed to have a 20 percent higher modulus and 10 percent lower density, compared to Al 7075-T76, without significant loss in strength, toughness, fatigue behavior, or stress corrosion resistance. The other alloy was assumed to have a 20 percent higher strength and 10 percent lower density, compared to Al 7075-T76, without significant loss in modulus, toughness, fatigue behavior, or stress corrosion resistance.

Selective application of the two advanced aluminum alloys used in the optimum combination would increase payload 44 percent or increase range by 23 percent for a constant takeoff weight airplane. This significant payoff is achieved in a high-performance version of the V/STOL by a 17 percent weight savings in the wing, fuselage, and tail structure. The tradeoff study also indicated that the range of payload improvements is approximately proportional to the percentage improvement in stiffness and strength.

1.2.3 Advanced Fleet Ballistic Missile

In the same feasibility study (Ref. 1), the C-4 Trident FBM forward adaptor shell was analyzed for potential weight savings as applied closely to the D5 Advanced Trident FBM forward adaptor. The critical design criterion for the forward adaptor shell is stiffness. Substitution of a new aluminum alloy exhibiting 33 percent higher specific stiffness resulted in an estimated 16 percent saving in weight of the 56-lb component. Relative significance of weight saved in this portion of the missile is five times the baseline first-stage motor and interstage. Consequently, the 9 lb

---

1 R. E. Lewis, D. Webster, and I. G. Palmer, A Feasibility Study for Development of Structural Aluminum Alloys From Rapidly Solidified Powders for Aerospace Structural Applications, Lockheed Palo Alto Research Laboratory Final Report, Contract F33615-77-C-5186, Technical Report No. AFML-TR-78-102, July 1978.

saved in the component is equivalent to 45 lb saved in the first-stage motor. This saving contributes a significant (classified) addition to range of the missile and is equivalent to about a 15-lb increase in payload. Significant additional weight savings can be expected in other portions of the adaptor section and in the equipment section by application of a high specific stiffness alloy.

1.3 PLAN FOR ALLOY DEVELOPMENT

Based on the above design tradeoff studies and other considerations, a program was formulated to develop advanced aluminum alloys from rapidly quenched particulate. The objective and scope are described in the following paragraphs.

1.3.1 Objective

The objective of this program is to develop advanced aluminum alloys that meet specific property goals. In addition, the program is to establish a metallurgical basis suitable for manufacturing scaleup and application to new weapon systems. Goal A is a 30 percent increase in specific modulus of elasticity relative to Al 7075-T76, without significant loss in strength, toughness, fatigue strength, or stress-corrosion resistance. Goal B is a 20 percent increase in specific modulus of elasticity accompanied by a 20 percent increase in specific strength, without significant loss in toughness, fatigue strength, or stress-corrosion resistance. The resulting property goals are as follows:

- Goal A. Specific elastic modulus: 33.1 $MNmkg^{-1}$ (133×10^6 in.*)
- Goal B. Specific elastic modulus: 30.4 $MNmkg^{-1}$ (122×10^6 in.*)
  Specific yield strength: 1.98 $kNmkg^{-1}$ (796×10^3 in.*)

1.3.2 Scope

The program is divided into three phases, each consisting of a number of tasks. Phase 1 involves fundamental alloy development studies and consolidation process development and optimization. The most promising alloys are to be selected,

*Units are actually (lbf/lbm) in.

produced in simple mill form, and evaluated in Phase 2. Phase 3 will consist of a design evaluation using the properties of the alloys evaluated in Phase 2.

This program was initiated in September 1978 and is scheduled for completion in 3-1/2 years. The effort during the first 2 years will be devoted to Phase 1 only. This report describes activity to date in each of the four tasks comprising Phase 1.

Section 2

EXPERIMENTAL PROCEDURES AND RESULTS

This section describes activities to date on Phase 1, Alloy Development. Activity on Phases 2 and 3 will not be initiated until Phase 1 is completed.

2.1. TASK 1 – DEVELOPMENT OF ALLOYS CONTAINING LITHIUM

This task is being conducted by the Lockheed Palo Alto Research Laboratories. Following is an outline of program Phase 1, Task 1:

- Selection of Alloys
- First Iteration of Alloys
- Characterization of Particulate
- Consolidation and Processing
- Aging Behavior
- Structure and Property Evaluation
- Second Iteration of Alloys
- Solidification Process Comparison
- Consolidation Process Optimization
- Selection of Alloy/Process for Scaleup

2.1.1 Alloy Compositions

The first iteration of eight alloys contain 3 wt% Li to meet program goal A of 30 percent increase in specific modulus; the compositions are given in Table 1. The first four alloys are based on the Al-Cu-Li system. One alloy contains commercial-purity lithium; the other three contain high-purity lithium. Two different Cu levels and two different grain refining elements were selected. The second four alloys

TABLE 1. FIRST ITERATION OF ALLOYS CONTAINING LITHIUM

LPARL Alloy Designation	Target Melt Composition (wt%)
1.1	Al-4Cu-3Li-0.2Zr
1.2	Al-3Li-2Cu-0.2Zr
1.3	Al-4Cu-3Li*-0.2Zr
1.4	Al-4Cu-3Li-0.4Mn
1.5	Al-3Li-1Zr
1.6	Al-3Li-1.5Mn
1.7	Al-3Li-0.5Fe-0.5Ni
1.8	Al-3Li-0.5Fe-0.5Co

*Commercial purity; all other alloys have high-purity lithium.

contain approximately 1 wt% of the following elements, or combinations of two elements: Zr, Mn, Fe + Ni, and Fe + Co, along with 3 wt% Li. These elements were selected to produce a fine dispersion of nondeformable dispersoid particles. The rationale for selection of the alloy compositions has been given previously (Ref. 2).

2.1.2 Generation of Splat Particulate

Argon atomized splat particulate was obtained from Alcoa for all eight first-iteration Al-Li based alloys. Alcoa's proprietary splat-making process is described in section 2.2.2. A total of 125 kg of material was obtained using the procedure outlined in Fig. 1. Applicable production information is given in Table 2.

Recovery levels from the nominal 28-kg-starting Al-Li alloy melts were lower than anticipated, making it impossible to meet the delivery target of 16 kg for each alloy.

2. R. E. Lewis, Development of Advanced Aluminum Alloys From Rapidly Solidified Powders for Aerospace Structural Applications. Interim Technical Report for period Sep 1978 – Mar 1979, Air Force Contract F33615-78-C-5203 DARPA Order 3575, Mar 1979.

TABLE 2. PRODUCTION INFORMATION – Al-Li ALLOY SPLAT

LPARL Alloy No./ Nominal Comp.	Min. Melt Temp. (K)	Starting Melt Wt. (kg)	Amount Li Added (kg)	Net Wt. Splat (kg)	Melt Recovery (%)	Notes
1.1/ Al-4Cu-3Li-0.2Zr	1,058	24.7	0.91	13.8	56	(a)
1.1X/ Al-4Cu-3Li	1,023	29.5	0.91	19	64	(b)
1.2/ Al-3Li-2Cu-0.2Zr	993	29.5	0.91	15	51	(c)
1.3/ Al-4Cu-3Li-0.2Zr	1,143	24	0.91	11	46	(a), (d)
1.4/ Al-4Cu-3Li-0.4Mn	1,143	28	1.14	13.2	47	(a)
1.5/ Al-3Li-1Zr	1,193	28	1.14	0	0	(a), (e)
1.5/ Al-3Li-1Zr	1,143	28	1.14	2.8	10	(a), (f)
1.5/ Al-3Li-1Zr	1,273	34	1.36	5.9	17	(a), (g)
1.6/ Al-3Li-1.5Mn	1,173	28	1.14	16	57	(a)
1.7/ Al-3Li-0.5Fe-0.5Ni	1,143	28	1.14	14.5	52	(a)
1.8/ Al-3Li-0.5Fe-0.5Co	1,143	28	1.14	14.7	52	(a)

(a) Heated tundish.

(b) Unheated tundish. Zr charge addition omitted.

(c) Unheated tundish. Melt temperature somewhat low.

(d) Commercial purity Li.

(e) Three attempts to atomize were unsuccessful.

(f) Inadequate melt temperature.

(g) Omitted special crucible step. Excessive skim generation and tool consumption.

Size limitations of the "special order" lithium-resistant crucibles precluded the use of larger starting melt weights for these first iteration materials.

Recovery levels in the several attempts to produce one of the alloys, Al-1Zr-3Li, were exceptionally poor (8.4-kg total from three 28- to 34-kg starting charges). The

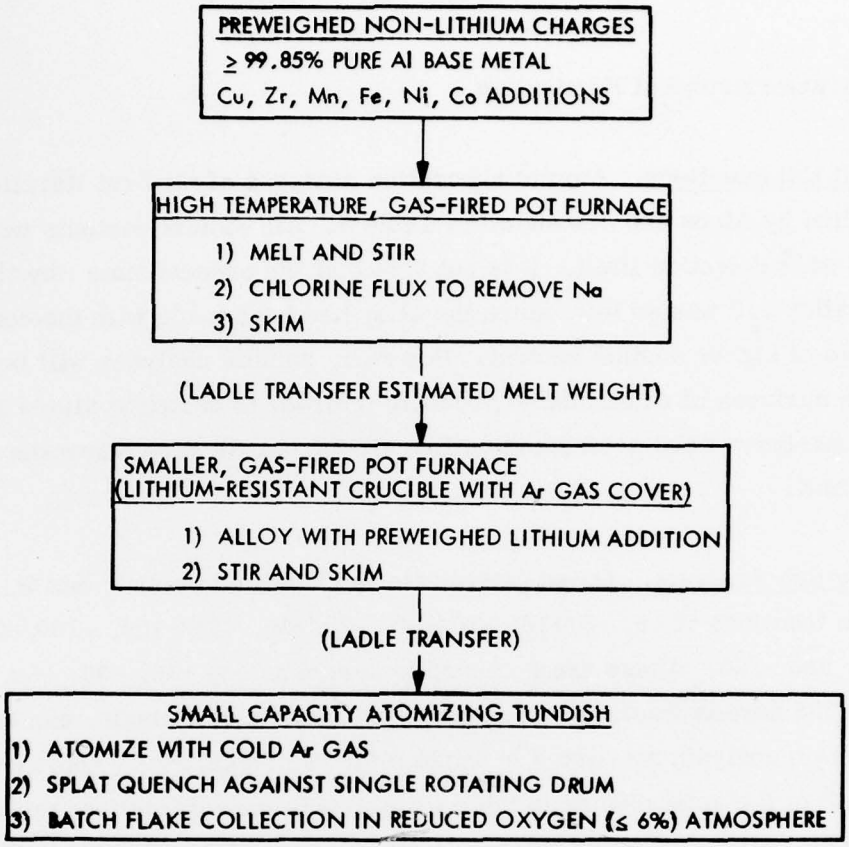

Figure 1. Al-Li alloy particulate preparation sequences

very high melt temperatures (≥ 1,273 K) required to produce splat in this corrosive alloy composition exceeded Alcoa's best current technology. Zirconite-coated stirring, skimming, and ladle transfer tools were rapidly consumed by the melt. Smoke and skim generation were excessive, and sparks were observed intermittently in the argon gas atomized, molten metal spray pattern.

Attempts to maintain adequate tundish metal temperatures without benefit of gas flame heating of the exposed melt surface were discontinued after the alloy 1.1 X and 1.2 runs. For the highest melting range alloy (Al-3Li-1Zr) the 1,227 K maximum melt holding temperature capability of the intermediate, special crucible furnace proved inadequate. In the last attempt with this composition, the lithium addition was made directly to the large high-temperature furnace crucible. This accounts for the larger starting melt weight of this particular run.

2.1.3 Characterization of Particulate

Actual Melt Compositions. Atomic absorption analyses of all first iteration alloys were supplied by Alcoa and are shown in Table 3. All sodium contents were below the 0.0005 wt % detection limit. It is not known at the present time why the sodium content of alloy 1.3 was so low, since the alloy had been made with the commercially pure lithium of higher sodium content. However, sodium analyses will be performed on fracture surfaces of consolidated products in order to compare alloys 1.1 and 1.3. Potassium analyses were performed on five alloys and all were below the 0.0001 wt % detection limit.

Screen Fraction Analysis. Loose particulate is classified by wt % into U. S. Standard screen size fractions of +8, -8/+16, -16/+30, -30/+50, -50/+100, -100/+200, -200/+325, and -325. These are referred to herein as +8, +16, +30, +50, +100, +200, +325, and -325 screen fractions, respectively. Results of a single, random sample screen fraction analysis are listed in Table 4 for each splat run. Approximately 10 to 20 wt % of the splat occurs in the coarsest (+8) screen fraction; this is characteristic of splat produced in the batch collection mode. All bulk materials were received by LPARL in the "as-splat" condition.

Cyclone Processing. A small amount (0.91 kg) of cold "as-splat" flakes was processed by Alcoa through the cyclone collection system normally used for atomized powder and air-processed splat flake production.

Table 5 compares the chemical composition and screen fraction data resulting from Alcoa's and LPARL's evaluation of loose particulate samples representing splat flakes before and after cyclone processing. This study verifies the cyclone's beneficial reduction in plan areas of the larger starting flakes without any substantial change in chemical composition as a result of contamination from prior lots of Al-14Mn and Al-2.5Mg-6Zn powder processed through the same system, and without any substantial increase in oxygen content. Although the Alcoa cyclone system was not available for supplemental processing of bulk Al-Li splat flake quantities in these first iteration alloys, cyclone attrition of future lots might be possible.

TABLE 3. FINAL MELT COMPOSITIONS – Al-Li SPLAT ALLOYS

	LMSC ALLOY	Cu	Fe	Si	Mn	Mg	Zn	Cr	Ti	Ni	Co	Zr	Li	Na	K	Note
1.1	Al-4Cu-3Li-0.2Zr	3.69	.05	.05	–	–	–	–	–	–	–	.21	3.61	<.0005	<.0001	(a)
1.1X	Al-4Cu-3Li	3.63	.05	.04	–	–	–	–	–	–	–	.01	2.49	<.0005	<.0001	(b)
1.2	Al-3Li-2Cu-0.2Zr	1.94	.05	.04	–	–	–	–	–	–	–	.19	2.82	<.0005	–	(c)
1.3	Al-4Cu-3Li*-0.2Zr	3.74	.04	.04	–	–	–	–	–	–	–	.21	3.23	<.0005	<.0001	(d)
1.4	Al-4Cu-3Li-0.4Mn	3.58	.07	.14	.39	–	–	–	–	.01	–	.00	2.62	<.0005	<.0001	(d)
1.5	Al-3Li-1ZR															
	(1)	–	.08	.06	–	–	.01	–	–	.04	–	1.15	4.35	<.0005	–	(e)
	(2)	–	.48	.15	.01	–	.01	–	–	.06	–	1.52	2.77	<.0005	–	(d)
1.6	Al-3Li-1.5Mn	.05	.05	.05	1.32	–	–	–	–	–	–	–	2.97	<.0005	<.0001	(e)
1.7	Al-3Li-0.5Fe-0.5Ni	–	.36	.05	.01	–	–	–	–	.48	–	–	3.56	<.0005	–	(c)
1.8	Al-3Li-0.5Fe-0.5Co	–	.48	.08	–	–	–	–	–	.01	.43	–	3.8	<.0005	–	(f)

(a) Single Analysis
(b) Average of six analyses
(c) Average of five analyses
(d) Average of three analyses
(e) Average of two analyses
(f) Average of four analyses

* Commercial-purity lithium. All others high-purity lithium.

TABLE 4. SCREEN FRACTION ANALYSIS RESULTS OF Al-Li ALLOY SPLAT FLAKES (SINGLE, RANDOM SAMPLE)

		SCREEN SIZE – U.S. STANDARD (PERCENT BY WEIGHT)							
	LMSC ALLOY	+8	-8 +16	-16 +30	-30 +50	-50 +100	-100 +200	-200 +325	-325
1.1	Al-4Cu-3Li-0.2Zr	11.2	35.8	19.2	15.4	9.1	6.6	1.4	1.0
1.1X	Al-4Cu-3Li	22.6	34.7	17.4	15.6	7.2	2.0	0.2	0.2
1.2	Al-3Li-2Cu-0.2Zr	17.4	45.2	19.8	11.4	3.2	1.6	0.6	0.6
1.3	Al-4Cu-3Li-0.2Zr	30.0	37.0	14.2	11.3	4.0	3.0	0.2	0.1
1.4	Al-4Cu-3Li-0.4Mn	21.0	43.0	19.4	10.2	3.8	2.2	0.2	0.2
1.5	Al-3Li-1Zr	16.8	39.4	20.2	14.0	5.4	3.6	0.4	0.2
		14.4	39.6	18.4	16.4	5.4	4.8	0.4	0.4
1.6	Al-3Li-1.5Mn	12.2	23.8	18.0	19.0	10.6	11.2	2.8	2.2
1.7	Al-3Li-0.5Fe-0.5Ni	17.0	37.0	20.6	16.8	5.2	2.4	0.4	0.4
1.8	Al-3Li-0.5Fe-0.5Co	15.2	36.2	18.8	13.6	9.6	4.6	0.8	0.8

TABLE 5. EVALUATION OF SUPPLEMENTAL CYCLONE PROCESSING[a]

COMPARISON OF CHEMICAL COMPOSITION (ATOMIC ABSORPTION ANALYSIS)

Condition		Cu	Fe	Si	Mn	Mg	Zn	Cr	Ti	Ni	Zr	Li
As Splat	(b)	3.67	0.09	0.08	0.00	0.00	0.02	0.00	0.00	0.01	0.17	3.24
	(c)				0.0018	0.0013	0.0030					3.24
As Splat + Cyclone	(b)	3.68	0.09	0.07	0.02	0.00	0.02	0.00	0.00	0.01	0.17	3.34
	(c)				0.0272	0.0084	0.0123					3.50

COMPARISON OF OXYGEN ANALYSIS[d]

Condition	Oxygen (wt %)
As Splat	0.111
As Splat + Cyclone	0.158

SCREEN SIZE COMPARISON

	Screen Size – U.S. Standard (wt %)							
Condition	+8	-8 +16	-16 +30	-30 +50	-50 +100	-100 +200	-200 +325	-325
As Splat	11.2	35.8	19.2	15.4	9.1	6.6	1.4	1.0
As Splat + Cyclone	0.6	18.2	18.4	17.4	14.4	15.0	7.6	8.2
Change in Each Size	-94.6%	-49.2%	-4.2%	+12.9%	+58.2%	+127.2%	+443%	+720%

(a) LMSC Alloy 1.1 Al-4Cu-3Li-0.2Zr.
(b) ALCOA Analysis.
(c) LMSC Analysis, average of two samples each.
(d) Fast neutron activation analyses by IRT Corporation, average of two samples each.

Particulate Morphology. Optical micrographs of three screen fractions of alloy 1.6 (Al-3Li-1.5Mn) are shown in Figs. 2, 3, and 4. The splat morphology ranges from roughly circular to highly elongated flakes. One surface of the flakes is flat (the chilled surface); the other surface is smooth or rippled. Nonsplat powder is found in screen sizes below 50 mesh. The nonsplat particles are rounded and have a dull grey colored surface and can be clearly distinguished from the splats which are flat and have bright shiny surfaces.

Loose Flake Oxygen Analyses. Fast Neutron Activation (FNA) oxygen analyses have been performed by IRT Corp. using duplicate samples from each splat run. Flakes were taken from Al-Li alloy run samples which had been individually stored in sealed 1 gal. containers immediately following their production. Ambient atmospheres were present within these run sample containers. Results are given in Table 6.

A comparison of the oxygen content determined earlier for alloy 1.1 flake sample, packed under residual argon, and analyzed within 3 days following splat quenching,

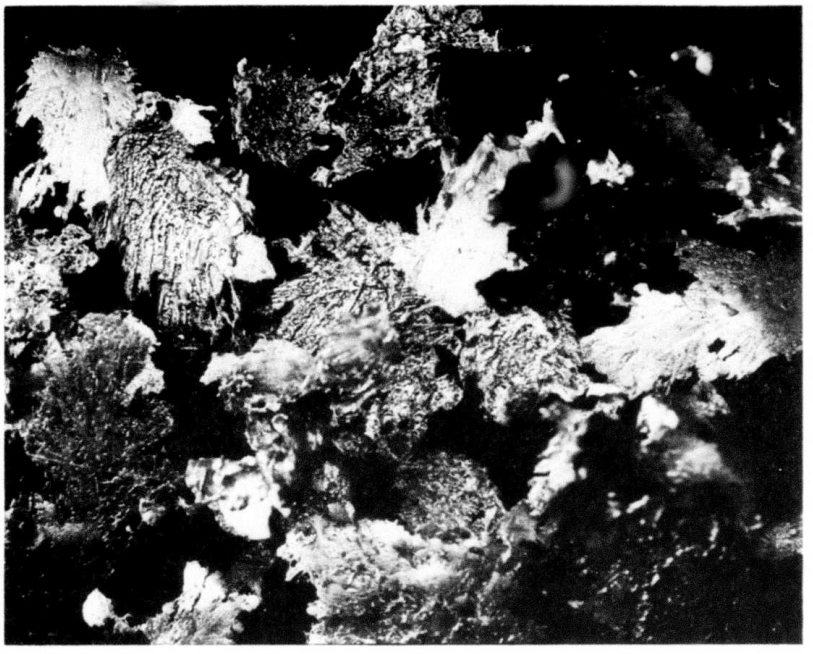

D8334 5×

Figure 2. Representative optical micrograph of alloy 1.6 (Al-3Li-1.5Mn) splat, +8 screen fraction

D8333 5×

Figure 3. Representative optical micrograph of alloy 1.6 (Al-3Li-1.5Mn) splat, +30 screen fraction

D8332 8×

Figure 4. Representative optical micrograph of alloy 1.6 (Al-3Li-1.5Mn) splat, +100 screen fraction

and these subsequent determinations of 8-week old samples of the same production run indicate a factor of 4× difference (0.123 versus 0.524 wt %) in oxygen content. This is a significant increase in oxygen content as an apparent consequence of ambient atmosphere storage within a closed container. Further investigations of this effect will be made. It is noteworthy that the effect is not confined to Al-Li alloys, but is also observed in the Alcoa alloys (see section 2.2.3).

Surface Oxide Content. Auger surface analysis studies are being performed by Perkin-Elmer Surface Sciences Division. Preliminary results on alloy 1.1 (Al-4Cu-3Li-0.2Zr) showed the following. On splat particulate from the +16, +30, and +100 screen fractions, the oxide film thickness was 50 to 75 Å; on nonsplat particles from the +100 screen fraction, the film thickness was 150 to 200 Å. According to Billman, CT-91 (formerly MA-87) alloy fine atomized powder also has an oxide film thickness approximately twice that of splat particulate (Ref. 3).

---

3. F. R. Billman, private communication, 1978.

TABLE 6. OXYGEN CONTENTS OF Al-Li ALLOY SPLAT FLAKES

LMSC ALLOY DESIGNATION		FNA OXYGEN ANALYSES[a] CONCENTRATION (WT. %)	PRECISION (± %)
1.1	Al-4Cu-3Li-0.2Zr	0.524	0.014
1.1X	Al-4Cu-3Li	0.633	0.017
1.2	Al-3Li-2Cu-0.2Zr	0.425	0.012
1.3	Al-4Cu-3Li*-0.2Zr	0.705	0.018
1.4	Al-4Cu-3Li-0.4Mn	0.477	0.013
1.5	Al-3Li-1Zr		
	(1)	0.615	0.016
	(2)	0.307	0.010
1.6	Al-3Li-1.5Mn	0.516	0.014
1.7	Al-3Li-0.5Fe-0.5Ni	0.467	0.013
1.8	Al-3Li-0.5Fe-0.5Co	0.540	0.015

*Commercial-purity lithium.

(a) Average of two analyses of each of two samples.

Further studies, however, made on splat and nonsplat particulate from the +100 screen fraction of alloys 1.1 (Al-4Cu-3Li-0.2Zr), 1.5 (Al-3Li-1Zr), and 1.6 (Al-3Li-1.5Mn) showed greater film thicknesses on some of the nonsplat particles. Adjacent splat and nonsplat particles were selected as shown in Fig. 5, and sputtering was performed on both particles at the same time so that the relative oxide film thicknesses would be more accurately determined. Analyses of the oxide films were also made. The results are shown in Table 7 and it can be seen that the film thicknesses on some of the nonsplat particles are very much greater than on the splats and greater than those found on atomized particles. The reason for these differences is not fully understood. They probably arise from the presence of two types of nonsplat particles. The first type is particles which have been atomized in the correct way but which have then solidified in flight; these particles are analogous to fine atomized powders, but they may be of greater size. The second type is particles which may have resulted from the buildup and unintended subsequent detachment of liquid metal from the tip of the atomizing nozzle. This liquid may be more heavily oxidized and possibly partially solidified at the time of detachment, thus resulting in particles with the thicker oxide films.

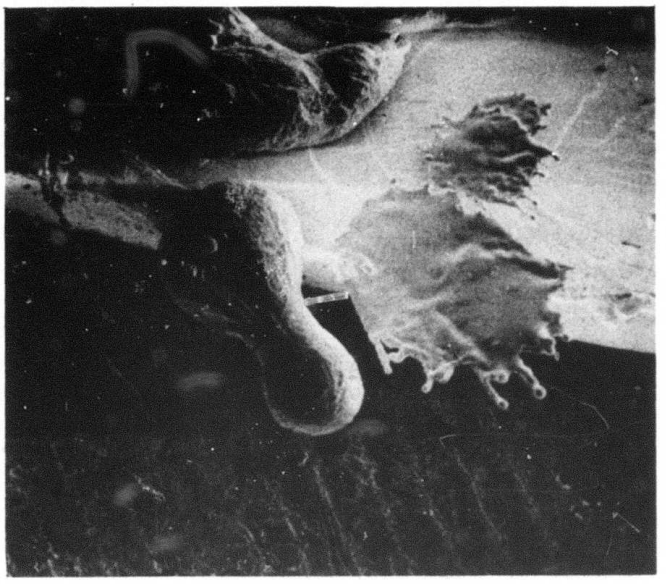

E378 100×

Figure 5. Secondary electron display picture showing adjacent splat and nonsplat particles of alloy 1.1, used for comparison of oxide film thickness

TABLE 7. AUGER ANALYSIS OF SURFACE OXIDE FILMS

Alloy No.	Composition	Screen Fraction	Particle Type	Atomic Concentration (%)				Film Thickness (Å)
				O	Al	Li	Cu	
1.1	Al-4Cu-3Li-0.2Zr	+100	Splat	59	21	17	3	40
				55	23	18	4	35
				57	28	15	0	105
1.1	Al-4Cu-3Li-0.2Zr	+100	Non-Splat	50	35	19	0	510
				63	19	17	1	35†
				50	35	15	0	>600
1.5	Al-3Li-1Zr	+100	Splat	46	35	17	0	40
1.5	Al-3Li-1Zr	+100	Non-Splat	50	25	25	0	>675
1.6	Al-3Li-1.5Mn	+100	Splat	59	21	19	0	65
1.6	Al-3Li-1.5Mn	+100	Non-Splat	47	34	18	0	2950

†Results suggest this particle is a splat.

Chemical analyses of the oxide films show predominantly O, Al, and Li. The relative amounts were analyzed for three particles each of splat and nonsplat particulate from alloy 1.1. The average values were, for splat, 57 at. % O, 24 at. % Al, 17 at. % Li, and 2 at. % Cu and, for nonsplat, 54 at. % O, 29 at. % Al, and 17 at. % Li. The amount of other elements was less than 0.1 at. %.

Microstructure. Microstructural studies are being performed using both light optical and transmission electron microscopy techniques. Optical microstructures of as-splat flakes were prepared by polishing and etching, using a modified Keller's etch consisting of 5-ml nitric acid, 2-ml hydrofluoric acid, 3-ml lactic acid, 50-ml glycerine, and 250-ml water, diluted 5:1 with distilled water prior to use. Optical microstructures of alloy 1.1 (Al-4Cu-3Li-0.2Zr) are shown in Fig. 6, which shows polished and etched transverse structures of flakes in the +30 screen fraction. Thin flakes (20 μm) [Figs. 6(a) and 6(b)] are predominantly free of a dendritic structure and appear to show fine cellular structures. Similar grain structures have been reported in the Alcoa alloy splats (Ref. 2) and in the "splats" formed in atomized powder by the impact and solidification of one particle on the surface of another (Ref. 4). Thicker flakes (30 to 60 μm) [Figs. 6(c) and (d)] show dendritic structures of varying degrees of coarseness. Secondary dendrite arm spacings were observed to range from less than 1 μm in flakes to greater than 10 μm in nonsplat particles. Multiple layered splats were also observed [Fig. 6(c)]. No clear evidence of a nondendritic to dendritic transition was observed as reported by Jones (Ref. 5) and observed in some of the Alcoa flakes (Ref. 2). Such structures are probably only observed in highly supersaturated alloys; e.g., Jones only observed them in Al-Fe alloys of greater than 4 wt% Fe (Ref. 5).

The microstructure of splat particulate of alloys 1.2 and 1.7 has also been characterized by optical metallography. The same general features were observed as seen in alloy 1.1. Characterization of the remaining alloys is continuing.

---

4. B. H. Kear, P. R. Holiday, and A. R. Cox, "On the Microstructure of Rapidly Solidified IN-100 Powders," Met. Trans., Vol. 10A, 1979, p. 191
5. H. Jones, "Observations on a Structural Transition in Aluminum Alloys Hardened by Rapid Solidification," Mater. Sci. Eng., Vol. 5, 1969/70, p. 1

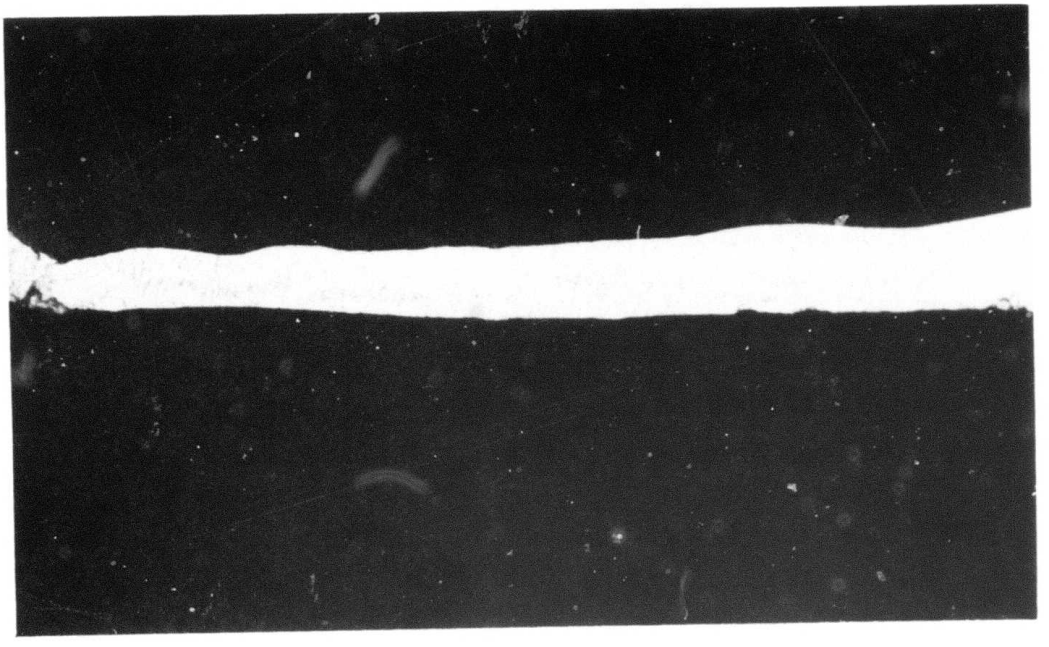

D8300 (a) 500×

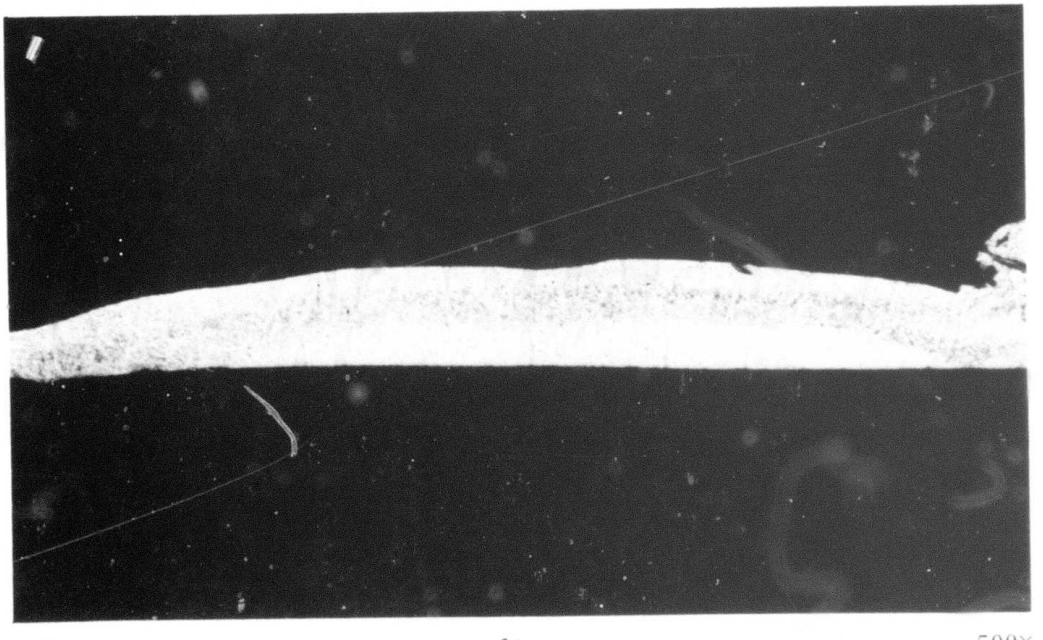

D8301 (b) 500×

Figure 6. Optical microstructure of alloy 1.1 (A1-4Cu-3Li-0.2Zr), showing typical morphology in the +30 screen fraction: (a) and (b) cellular grain structure in thin flakes, (c) multiple layer flake, (d) dendritic structures

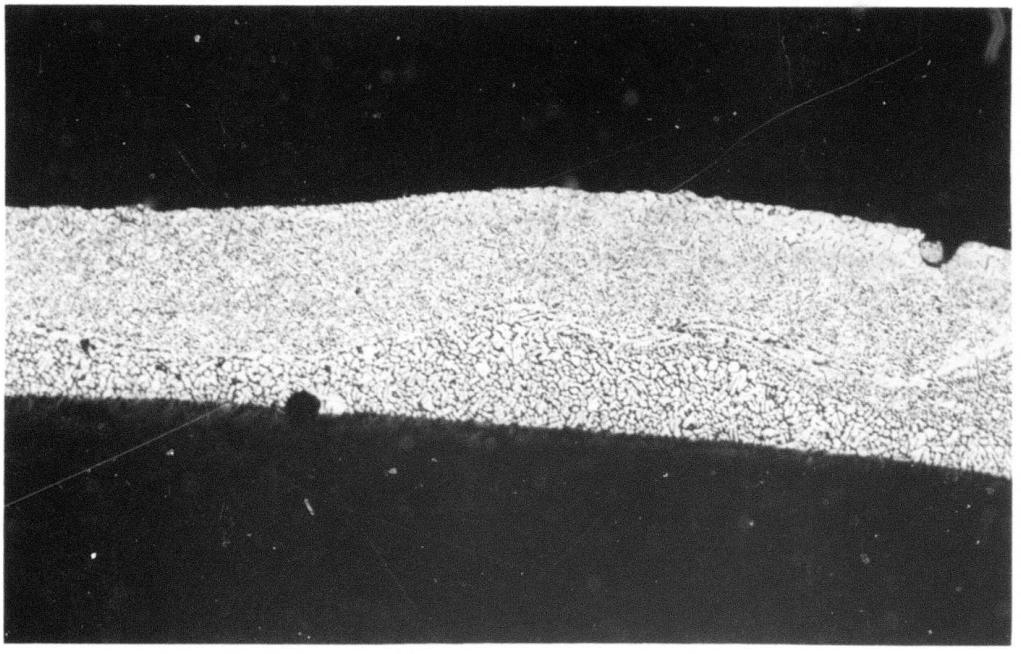

D8303 (c) 500×

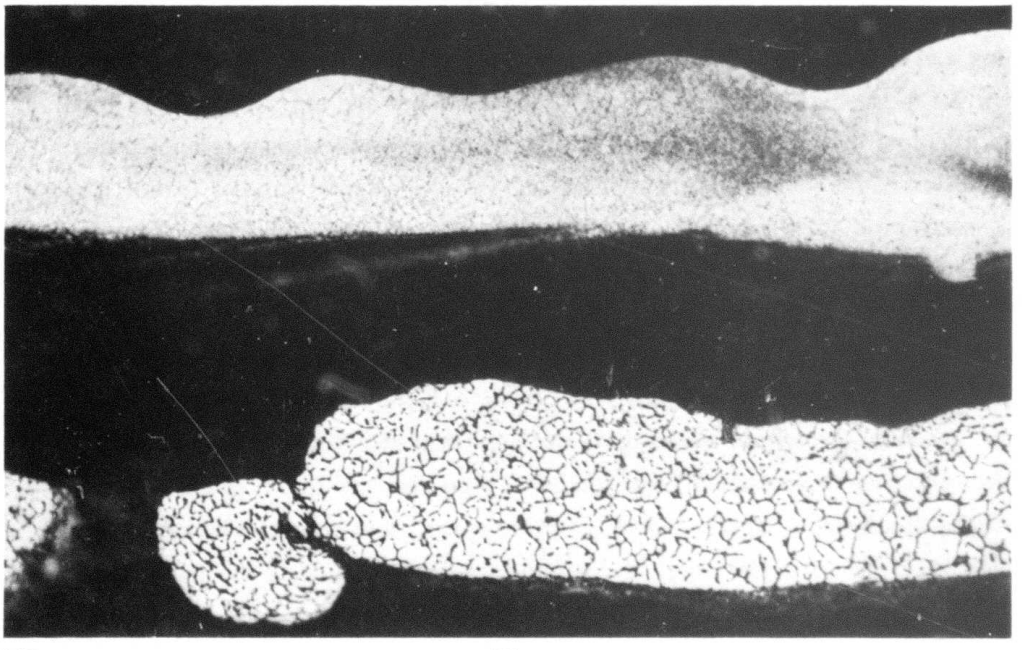

D8302 (d) 500×

Figure 6. (Cont.)

Transmission electron microscopy of the splat flakes has been initiated using thin foils prepared from flakes in the +16 screen fraction of as-received particulate. Disks of 2.3 mm. dia. were cut from the flakes and thinned by twin jet electropolishing using a 33% nitric acid/67% methanol electrolyte at about 253 K (-4°F). Examples of the microstructure of thin foils from alloy 1.1 are shown in Figs. 7 and 8. Figure 7 shows the fine cellular structure of cell size about 1 μm produced by the rapid solidification. Diffraction patterns from the foils showed faint superlattice spots attributed to the δ' precipitate. Figure 8 is a dark-field micrograph taken using one of these spots, which shows a very fine dispersion of δ'. These results show that δ' precipitation occurred either during the quench or during subsequent room-temperature aging. This suggests that it is not possible to prevent precipitation of δ' in these alloys, even by the use of the very high cooling rates achieved in the splat making process.

2.1.4 Consolidation and Processing

General Procedures. Initial consolidations have been made using as-received unscreened particulates to establish baseline mechanical property data. The effects of screening and removal of nonsplat particles from the bulk lots of splat will be assessed in the next stage of the program. Hot pressings and extrusions have been made from all eight of the first iteration alloys. The procedure used is shown in Fig. 9. Samples of the particulate weighing 300 g were weighed out and loaded into a 68-cm long steel pipe, of 5 cm I.D., using an argon back-filled glove box to minimize exposure to ambient air. The pipe was sealed by means of two nylon plugs, and then transferred to a cold compaction press (Fig. 10) where the particulate was compressed from its initial low packing density of about 10 percent to a density of about 40 percent using a pressure of about 27 MPa (4 ksi). A curve showing density as a function of compaction pressure for typical splat material has been shown previously (Ref. 1). The cold compact was then pushed from the steel pipe directly into a graphite-lined steel die. The steel die, graphite liner, graphite plugs, and steel backing plugs are shown in Fig. 11. The die containing the sample was then placed in the induction-heated vacuum hot press, vacuum degassed by slowly heating (1.5 h) to 983 K (950°F) using a vacuum of 2×10^{-5} mm Hg, and then hot pressed at the same temperature for 30 min using a pressure of 55 MPa (8 ksi).

472

1 μm

Figure 7. Transmission electron micrograph of alloy 1.1 (Al-4Cu-3Li-0.2Zr) splat particle, +16 screen fraction

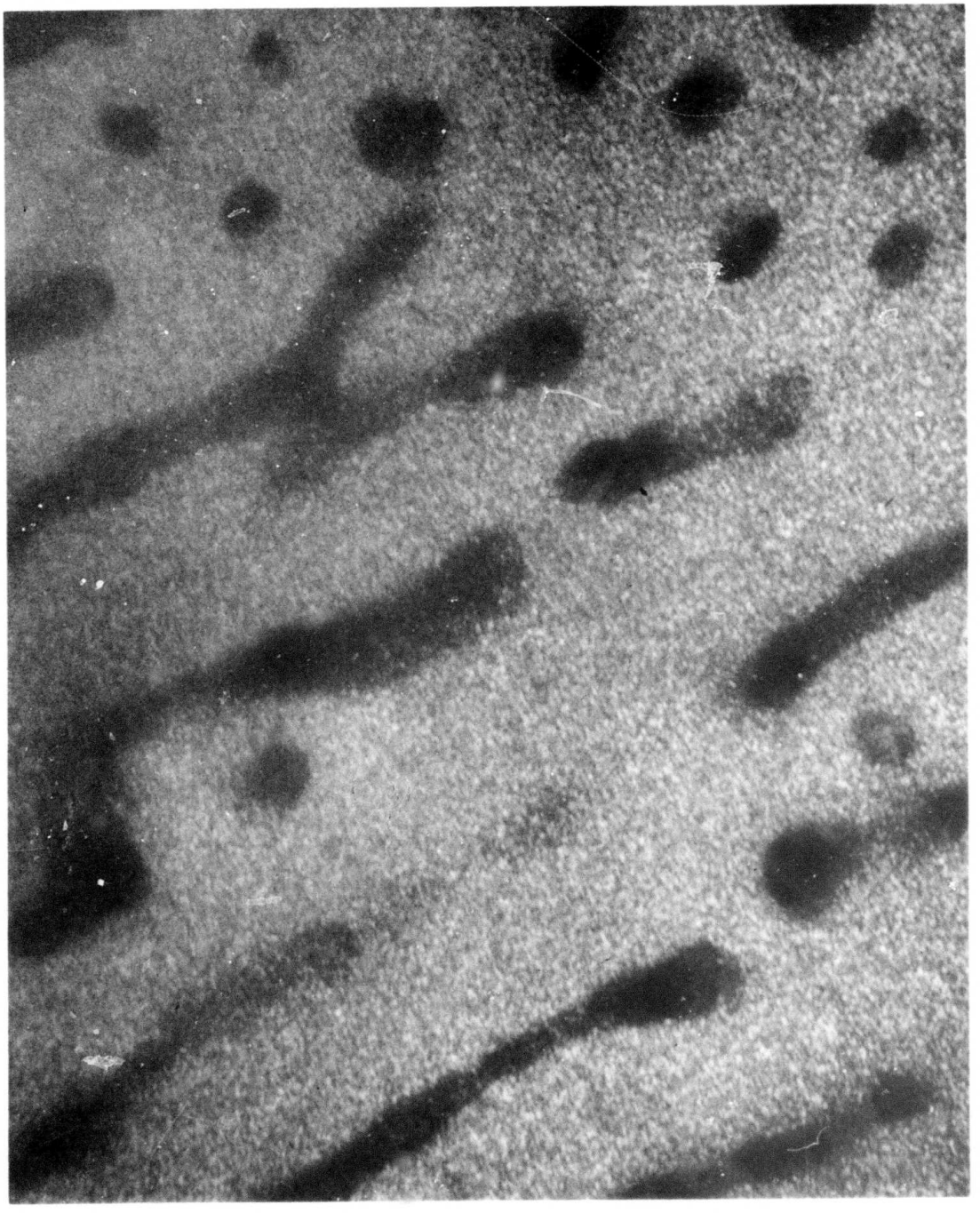

477

0.2 μm

Figure 8. Dark-field transmission electron micrograph of alloy 1.1 (Al-4Cu-3Li-0.2Zr) splat particle, +16 screen fraction

Samples were allowed to cool, and then were removed from the hot press; the density was measured and found to be close to the theoretical value.

Compacts were then extruded at 700 K (800° F) using an extrusion ratio of 8:1. Initial extrusions were performed using only a graphite-based lubricant. Subsequent extrusions were made using copper foil as an additional lubricant to improve the surface finish. The copper foil was subsequently removed by stripping and etching. The extrusions of all eight first-interation alloys are shown in Fig. 12.

Characterization of As-Extruded Alloys. The microstructure of alloy 1.1 has been characterized in both the as-hot-pressed, and as-extruded conditions. Figure 13 shows the longitudinal and transverse microstructures of a 5 cm-diameter hot-pressed compact which was vacuum degassed at 783 K (950° F) and then vacuum hot pressed at 783 K using a pressure of 55 MPa (8 ksi). Notice that there is very little porosity present, although some regions of poor interparticle bonding exist, especially around the nonsplat particles. The very much coarser microstructure of some of the nonsplat particles is also very visible. Figure 14 shows the longitudinal and transverse microstructures of the same hot-pressed compact after extrusion at 700 K (800° F). The coarser microstructure of the nonsplat particles can still be seen. Preliminary tensile data have been obtained for the alloy in the as-extruded condition. The yield strength was 241 MPa (35 ksi), the ultimate strength 324 MPa (47 ksi), and the elongation 5 percent. Characterization of the other alloys in continuing.

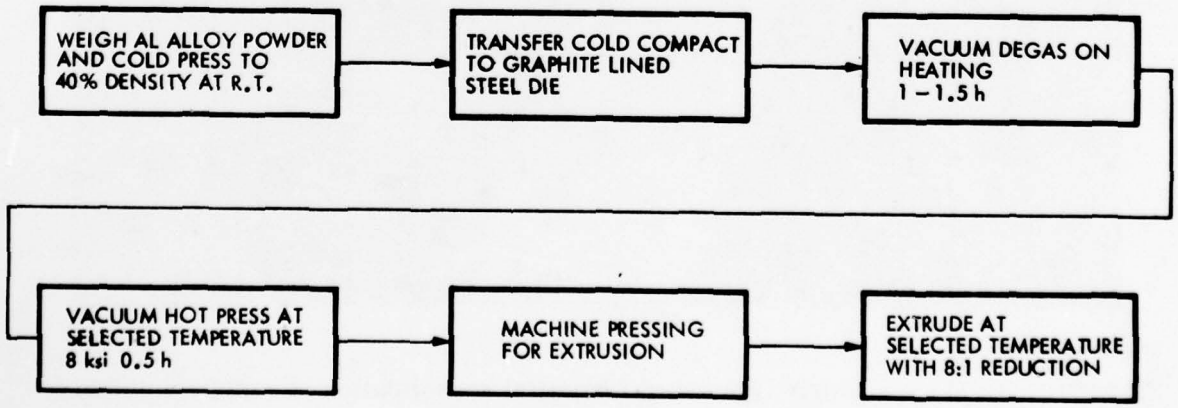

Figure 9. Flow chart for consolidation of Al-Li rapidly solidified particulate

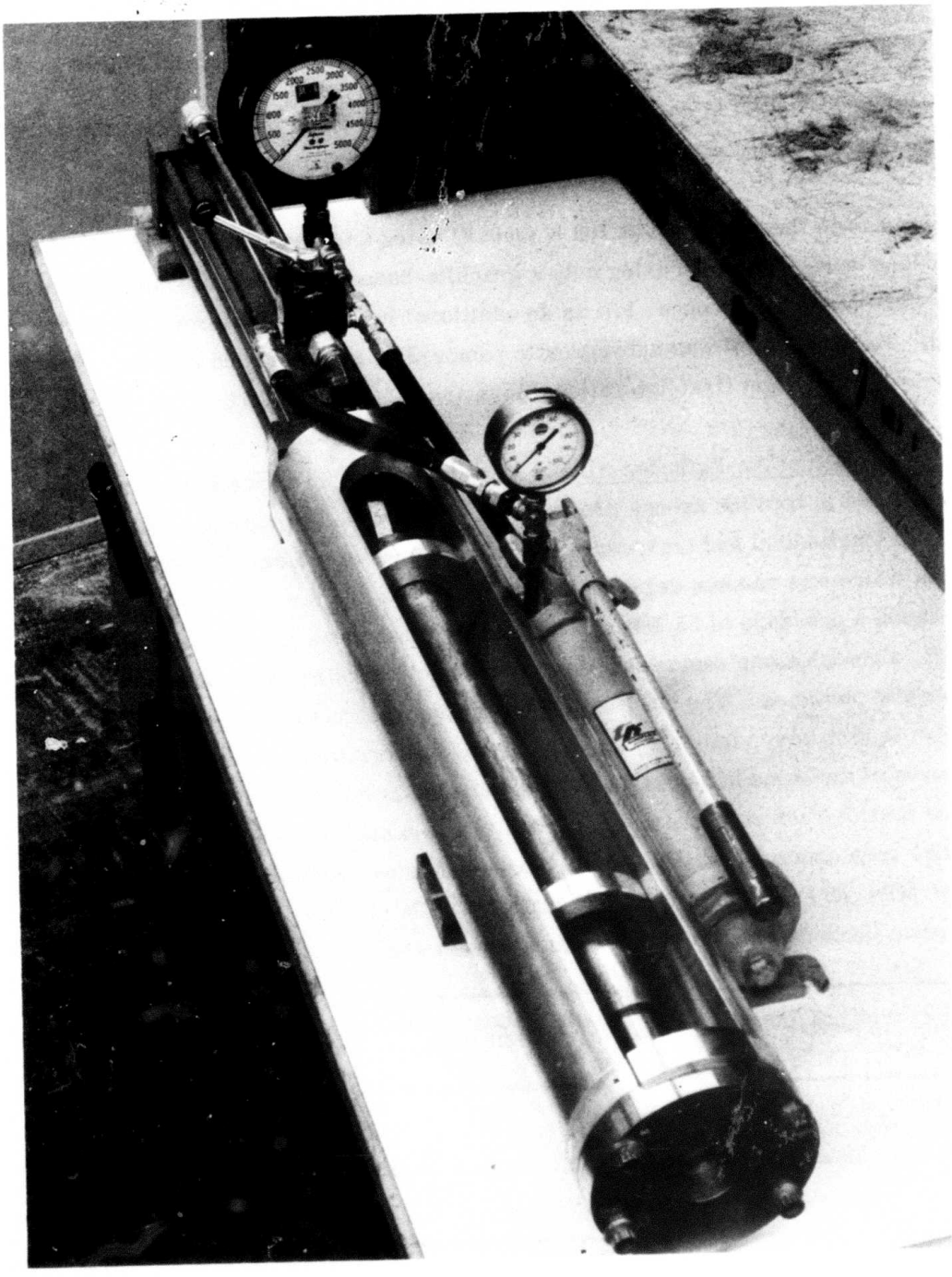

D9688.5

Figure 10. Cold compaction press used for initial consolidation of rapidly solidified Al-Li particulate

2.1.5 Aging Behavior

Extrusions of all eight first-iteration alloys were solution treated at 811 K (1000° F) for 30 min and water quenched. They were then stored at low temperature in a mixture of dry ice and methyl ethyl ketone prior to aging. Samples were aged at 464 K (375° F) for times ranging from 30 min to 40 h, and the aging response characterized by hardness measurements. The results are shown in Figs. 15 and 16. From these aging curves a peak hardness aging time of 8 h was selected for initial evaluation of mechanical properties.

Samples were also aged at room temperature for times up to 616 h. The results show no significant hardness increases.

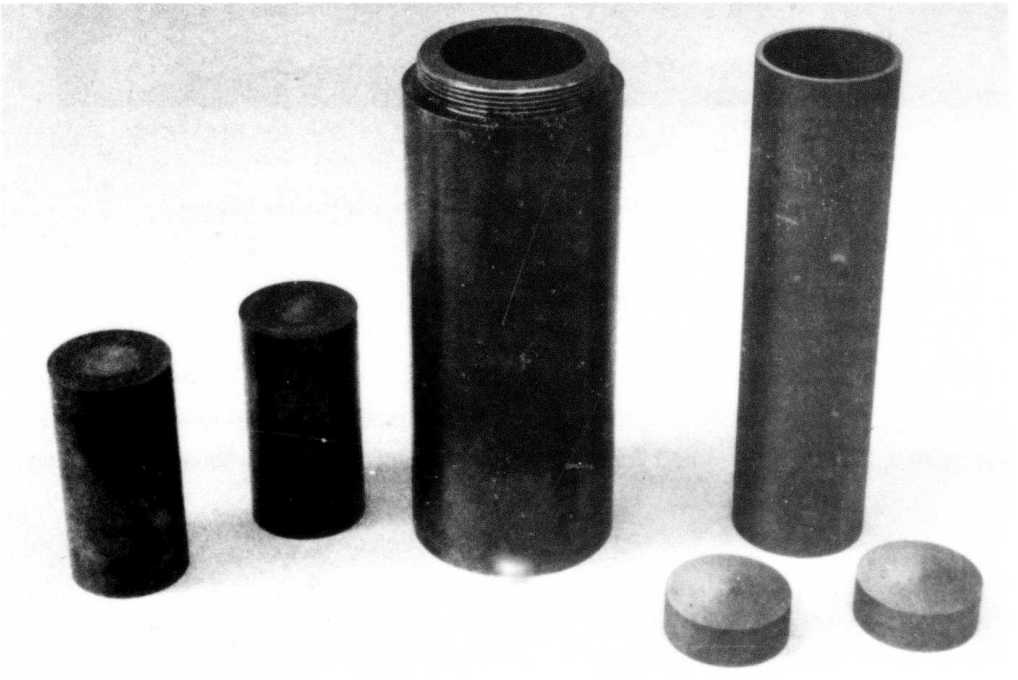

D9688.8

Figure 11. Steel die, graphite liner, and plugs used for hot pressing of rapidly solidified aluminum particulate

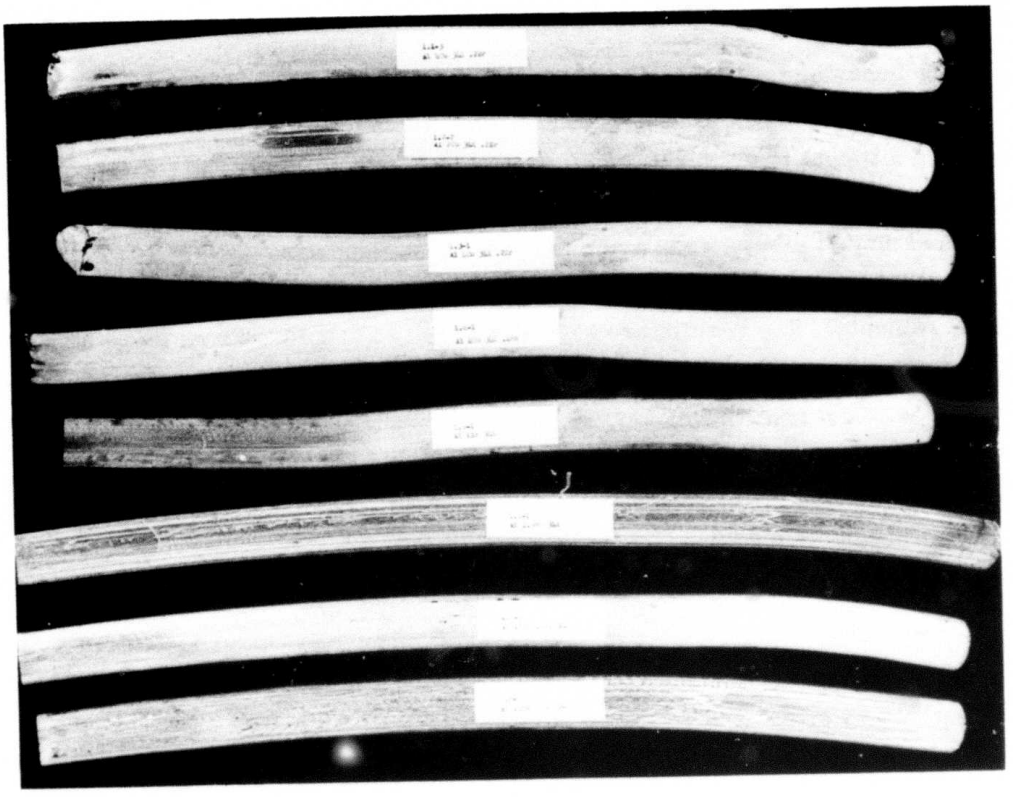

D9871

Figure 12. Extrusions of Al-Li first-interation alloys

2.1.6 Structure and Property Evaluation

Initial evaluation of structure and properties is being made by the determination of modulus, density, and tensile properties in both the peak-aged and underaged conditions, together with microstructure and fractographic characterization. Density is being

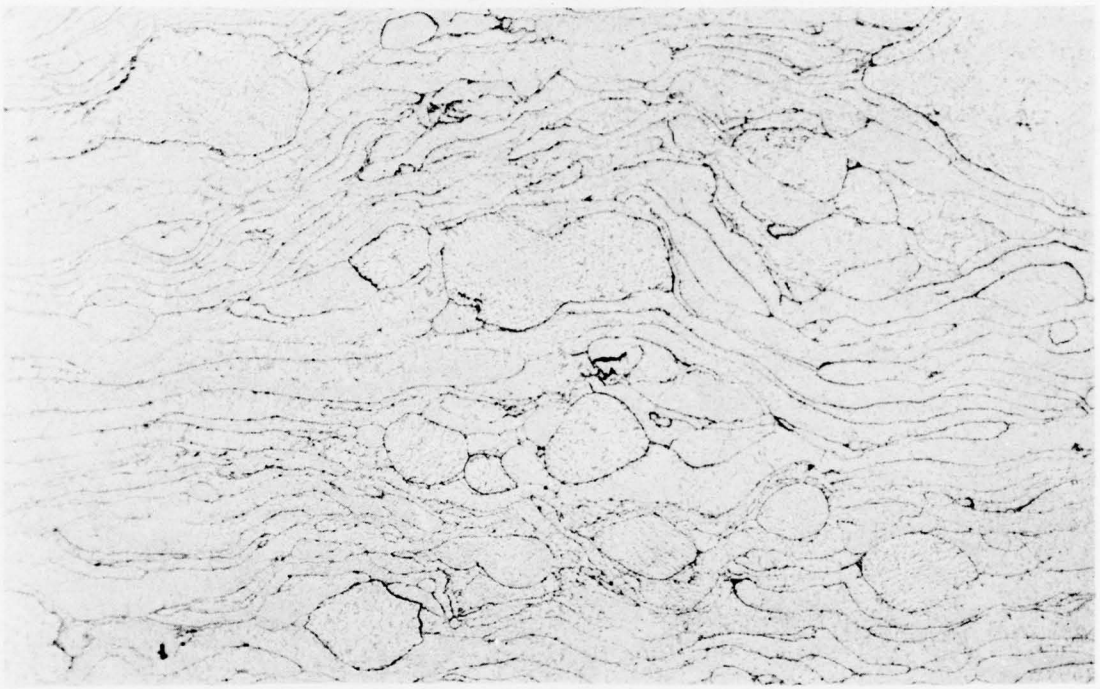

D8536 (a) 160×

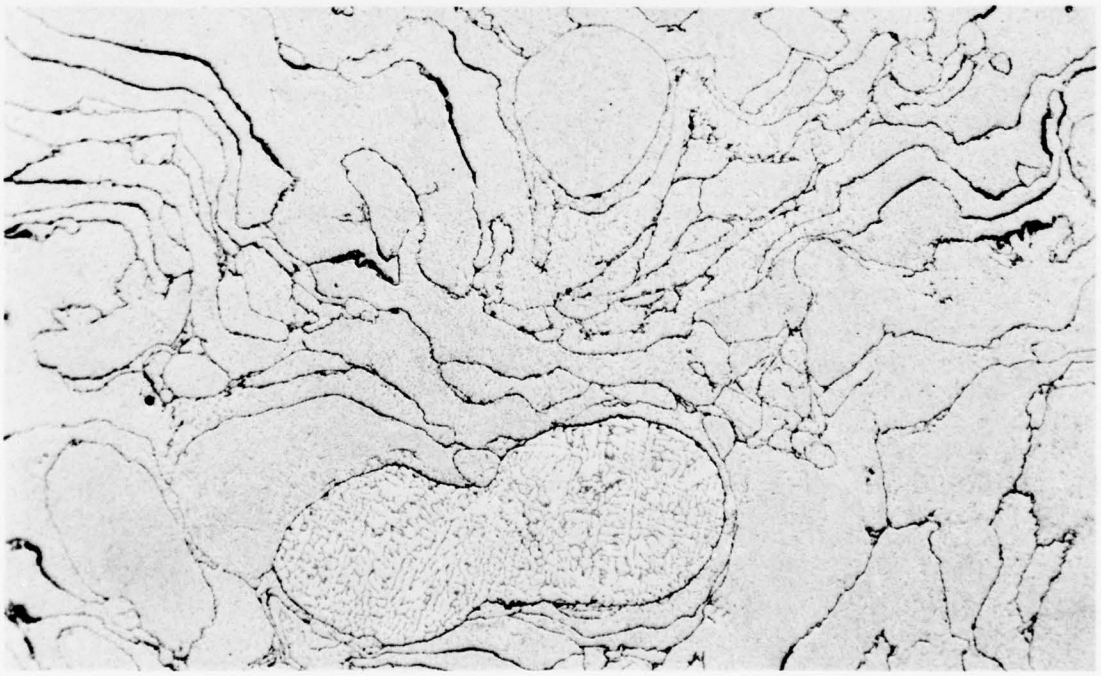

D8545 (b) 160×

Figure 13. Optical microstructure of alloy 1.1 (Al-4Cu-3Li-0.2Zr) vacuum degassed and hot pressed at 783 K and 55 MPa (a) longitudinal (b) transverse

D8610 (a) 200×

D8620 (b) 200×

Figure 14. Optical microstructure of alloy 1.1 (Al-4Cu-3Li-0.2Zr) after hot pressing, and extrusion at 700 K (a) longitudinal (b) transverse

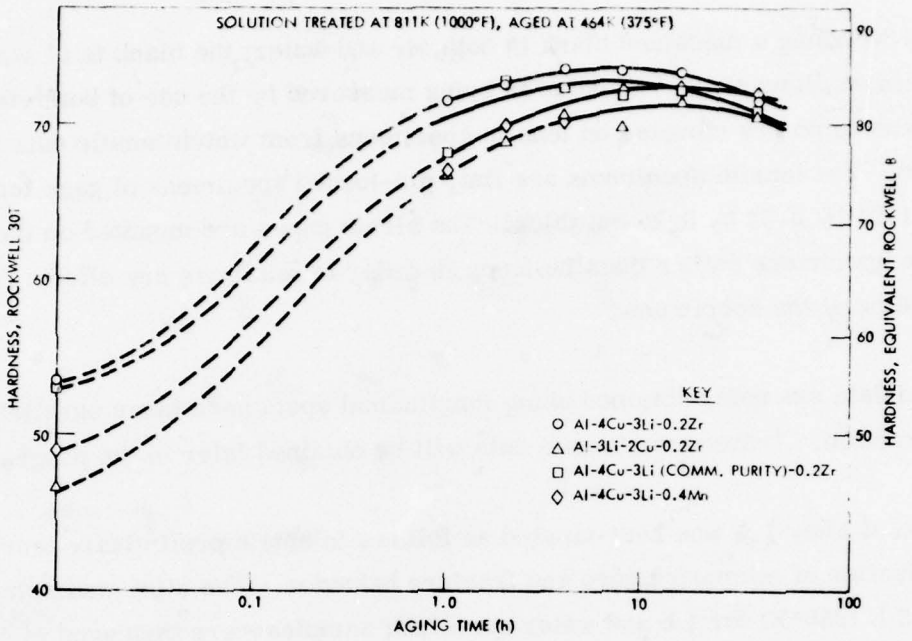

Figure 15. Aging characteristics of first four Al-Li alloys solution treated at 811 K (1,000° F), aged at 464 K (375° F)

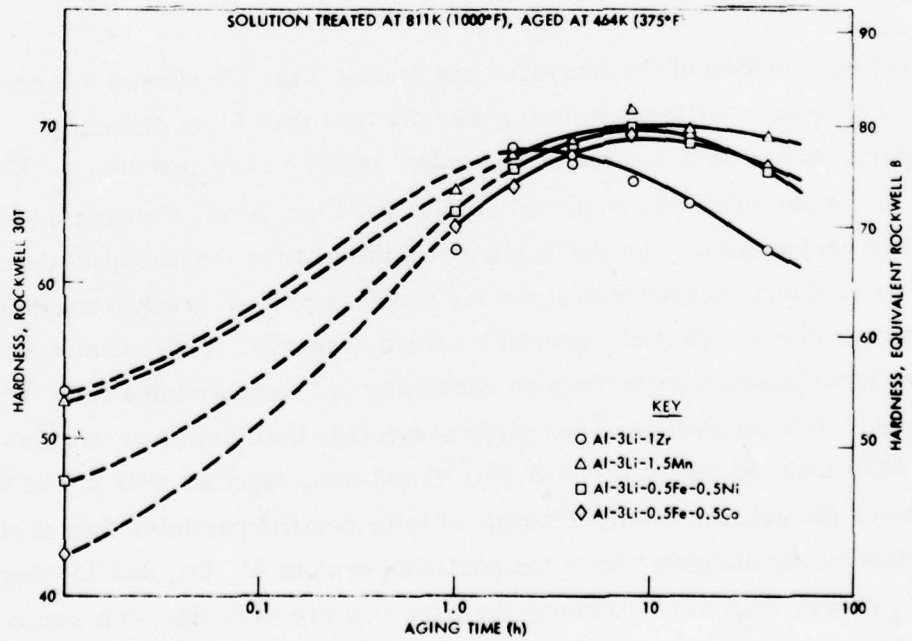

Figure 16. Aging characteristics of second four Al-Li alloys solution treated at 811 K (1,000° F), aged at 464 K (375° F)

measured by weighing a machined blank in both air and water; the blank is of standard Charpy specimen dimensions. Modulus is being measured by the use of both strain gages and extensometers mounted on tensile specimens from which tensile data are also obtained. The tensile specimens are flat, pin-loaded specimens of gage length dimensions 1.91 by 0.32 by 0.25 cm thick. The strain gages are mounted on the edge of the tensile specimens rather than the faces in order to minimize any effects from possible bending of the specimens.

Initial tensile data are being obtained using longitudinal specimens taken parallel to the extrusion direction. Transverse tensile data will be obtained later in the program.

One extrusion of alloy 1.1 was heat-treated as follows to obtain preliminary tensile data and evaluation of microstructure and fracture behavior. The alloy was solution treated at 783 K (950° F) for 1 h and water quenched; samples were then aged at 464 K (375° F) for 1 and 4 h. Both conditions showed the following preliminary tensile properties: σ_y = 414 MPa (60 ksi), E = 84.8 GPa (12.3×10^6 psi), and elongation = 3 percent.

Microstructural examination of the fractured specimens (Fig. 17) showed a large volume fraction of intermetallic particles, generally less than 1-μm diameter in "splat" regions, and up to 2 to 3 μm in "nonsplat" regions of the extrusion. Extensive cracking of the particles was observed even at the 1-μm level, showing that the particles are very brittle. The mechanism of failure of the tensile specimens appears to be by void coalescence with the voids nucleating at the cracked particles. No obvious failures of prior particle boundaries were observed. SEM examination of the fracture surfaces shows ductile dimples containing cracked particles (Fig. 18). It should be noted from the melt analyses given previously that this alloy contains more Li (3.6 wt%) than the target value (3.0 wt%) and this, together with 3.7 wt% Cu, probably produces the greater volume fraction of intermetallic particles than desirable. Energy dispersive x-ray analysis shows the particles contain Al, Cu, and Li; they are probably the T_1 phase, Al_2CuLi. Although the particles are very fine as a result of the rapid solidification approach, their high volume fraction and brittleness appear to be the cause of the low ductility (elongation = 3 percent). A higher solution treatment temperature for this alloy and the other alloys was selected to dissolve a greater

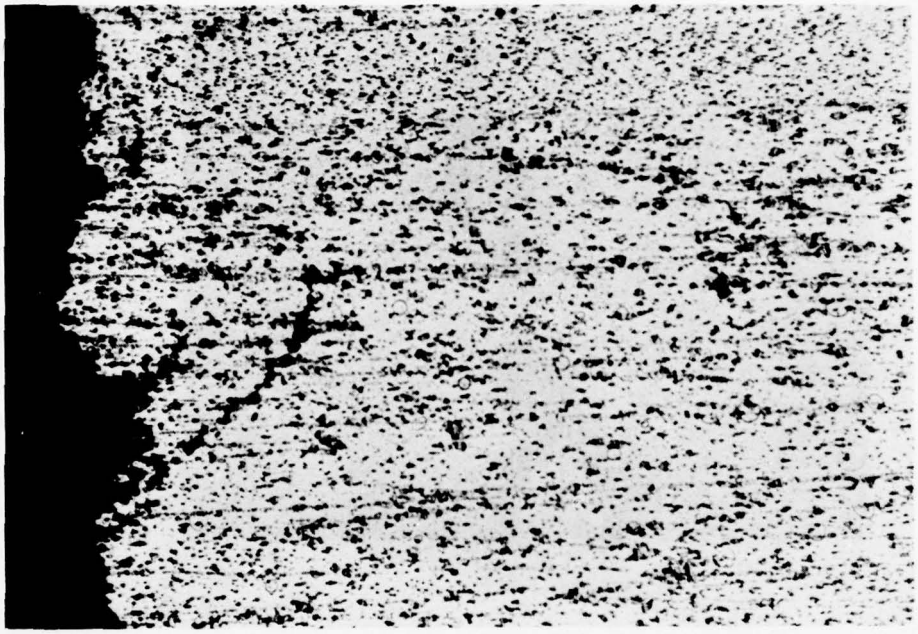

D8976 (a) 40 μm

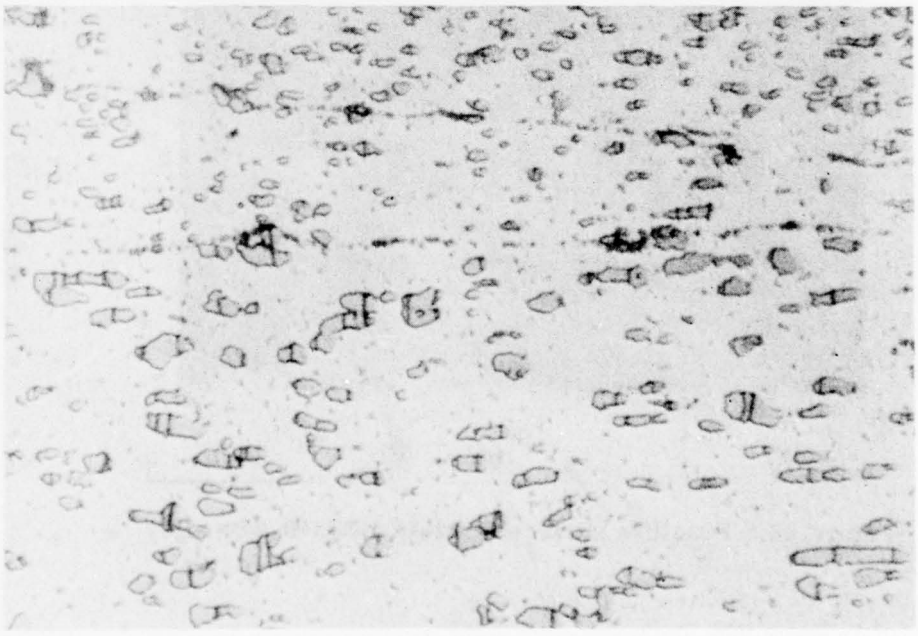

D9007 (b) 10 μm

Figure 17. Al-4Cu-3Li-0.2 Zr consolidated material solution treated 783 K (1 h), aged 464 K (4 h)

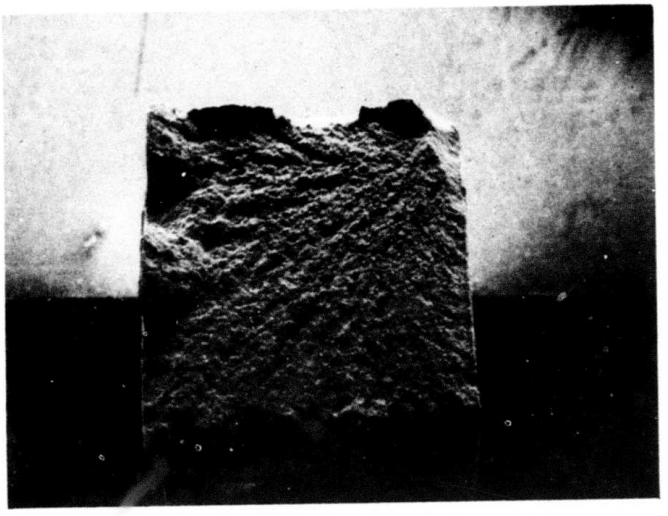

9GMX (a) 1 mm

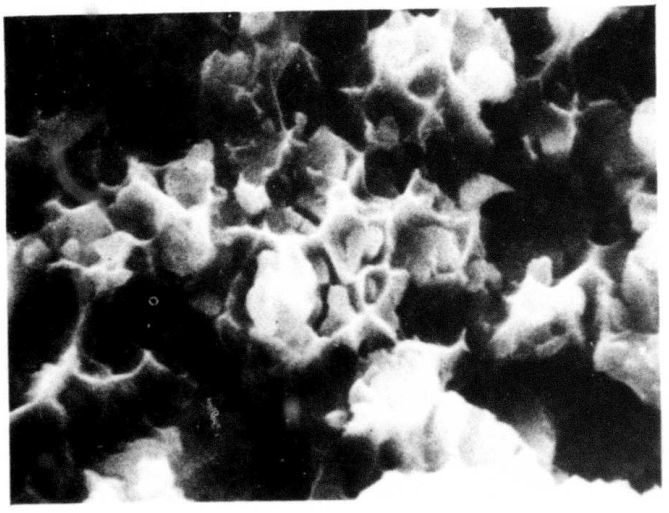

9GNG (b) 5 μm

Figure 18. Fracture surface of Al-4Cu-3Li-0.2Zr alloy

amount of any second-phase particles present. Extruded material of all eight first-iteration alloys were solution-heat-treated at 811 K (1000°F) for 30 min, water-quenched, and then aged at 464 (375°F) for 8 h. The aging time of 8 h was used, based on the aging curves of Figs. 13 and 14, to give a peak aged condition for all the alloys, with the exception of alloy 1.5 which would be in a slightly overaged condition. Modulus, density, strength, and elongation data for all eight alloys, tested at room temperature, are shown in Tables 8 and 9. These data are average values taken from the results of two tests. Also shown in Table 9 are Charpy V-notch impact energy absorbed data for a single set of specimens, also tested at room temperature.

It can be seen that the density and modulus values of all the alloys are in the range expected for alloys containing 3 wt% lithium, and that the specific modulus values meet contract property goal A. Actual values range from slightly less than to significantly greater than the goal A value of 133×10^6 in., probably as a result of the different lithium levels in the alloys. This is an encouraging result in that it shows that future work can be concentrated on improving the secondary properties of these alloys. Yield-strength values range fron 462 MPa (67 ksi) for alloy 1.1, which is equal to the property goal A value, to 303 MPa (44 ksi) for alloy 1.8. The first set of four alloys, containing copper, all show yield strengths greater than 414 MPa (60 ksi). In the second set of four alloys, the yield strengths of alloys 1.6 [407 MPa (59 ksi)] and 1.7 [400 MPa (58 ksi)] are almost as high as for the copper containing alloys. The lower yield strength of alloy 1.5 is probably the result of the alloy being in an overaged condition. The reason for the lower yield strength of alloy 1.8 is not presently known; the alloy has a hardness similar to alloy 1.7 and is expected to have a similar yield strength.

The elongation values range from 2.7 to 5.7 percent and are lower than the program goal (7 percent minimum, 10 percent typical). It is worth noting, however, that they are generally higher than the elongation values observed in some ingot cast Al-3Li based alloys also aged to the peak strength condition, which exhibit elongation values of about 2 to 3 percent (Ref. 6).

---

6. T. H Sanders, Factors Influencing Fracture Toughness and Other Properties of Aluminum-Lithium Alloys, Final Report, Naval Air Development Center, Contract N-62268-76-C-0271 for Naval Air System, Jun 1979.

TABLE 8. ELASTIC MODULUS AND DENSITY OF FIRST-ITERATION ALLOYS – PRELIMINARY DATA T6 CONDITION

	Elastic Modulus E		Density ρ		E/ρ		Increase Relative to 7075-T76 (%)		Decrease Relative to 7075-T76 (%)
Alloy	(GPa)	(x 10^6 psi)	(x 10^3 kg m^{-3})	(lb $in.^{-3}$)	(MNm kg^{-1})	(x 10^6 in.)*	E	E/ρ	ρ
1.1	82.6	11.9	2.53	0.091	33.2	131	15.9	28.2	9.6
1.2	87.3	12.7	2.54	0.092	35.0	138	22.9	35.2	9.1
1.3	80.7	11.7	2.53	0.091	32.6	128	13.7	25.8	9.6
1.4	82.5	12.0	2.56	0.092	32.8	129	16.1	26.8	8.5
1.5	84.8	12.3	2.56	0.092	33.8	133	19.4	30.5	8.5
1.6	87.2	12.7	2.48	0.090	35.9	141	22.8	38.6	11.4
1.7	83.2	12.1	2.47	0.089	34.4	135	17.2	32.7	11.7
1.8	84.1	12.2	2.47	0.089	34.7	136	18.5	33.8	11.5

*Units are actually (lbf/lbm) in.

TABLE 9. MECHANICAL PROPERTIES OF FIRST-ITERATION ALLOYS – PRELIMINARY DATA T6 CONDITION

Alloy	Nominal Composition	0.2% Yield Strength (MPa)	0.2% Yield Strength (ksi)	Tensile Strength (MPa)	Tensile Strength (ksi)	Elastic Modulus (GPa)	Elastic Modulus (x 10^6 psi)	Elongation (%)	Charpy V-Notch Energy Absorbed (J)	Charpy V-Notch Energy Absorbed (ft lb)
1.1	Al-4Cu-3Li-0.2Zr	463	67.2	510	73.9	82.6	11.9	3.0	0.94	0.69
1.2	Al-3Li-2Cu-0.2Zr	437	63.4	530	76.9	87.3	12.7	5.2	3.34	2.46
1.3	Al-4Cu-3Li-0.2Zr	461	66.9	508	73.7	80.7	11.7	3.7	1.04	0.77
1.4	Al-4Cu-3Li-0.4Mn	415	60.2	474	68.8	82.5	12.0	2.9	1.40	1.03
1.5	Al-3Li-1Zr	379	55.0	426	61.8	84.8	12.3	5.6	2.89	2.13
1.6	Al-3Li-1.5Mn	410	59.4	470	68.1	87.2	12.7	2.7	2.66	1.96
1.7	Al-3Li-0.5Fe-0.5Ni	401	58.2	461	66.8	83.2	12.1	3.6	2.41	1.78
1.8	Al-3Li-0.5Fe-0.5Co	324	47.0	411	59.6	84.1	12.2	5.7	3.17	2.34

Examination of the fracture surfaces and microstructures of the fractured tensile and Charpy specimens has been initiated. The microstructures of the Charpy specimen of alloy 1.2 is shown in Fig. 19. This shows significantly less of the brittle insoluble phase which was present in alloy 1.1 and which appeared to be the primary cause of low ductility of that alloy. It is significant that all of the alloys containing 4 percent Cu, namely alloys 1.1, 1.3, and 1.4, have low Charpy impact energy and relatively low elongation, whereas alloy 1.2, containing 2 percent Cu, has the best combination of strength and elongation together with the highest impact energy of any of the alloys in this first set of tests.

The fracture surface and microstructure of one of the alloys in the second set of four, namely alloy 1.7, has been examined. SEM pictures of the fracture surface are shown in Fig. 20. Significant areas of delamination are observed, indicating failure along prior particle boundaries [Fig. 20(a)]. Between the delaminations, the specimen appears to have failed by shear, and areas of fine dimpled rupture are seen [Fig. 20(b)]. Microstructural examination confirms the delamination and shear failures of the specimen (Fig. 21). A number of brittle particles are observed at low magnifications [Fig. 21(a)] showing multiple fractures along their length. At higher magnification [Fig. 21(b)] thin films are seen in prior particle boundaries, together with a fine dispersion of submicron particles. The nature of these various second phase particles has not yet been determined. Examination of the other alloys is continuing.

It is worth noting that these initial tests have been performed on material made from unscreened particulate, using a nonoptimized consolidation technique and a single-peak aging heat treatment. The results must therefore be considered preliminary; nevertheless reasonable mechanical properties have been obtained. The following steps will be evaluated in future work with respect to improvement of properties of the alloys:

- Removal of most of the nonsplat particles by screening
- Use of higher hot-pressing temperatures and pressures
- Use of higher extrusion ratios
- Use of underaging and overaging heat treatments

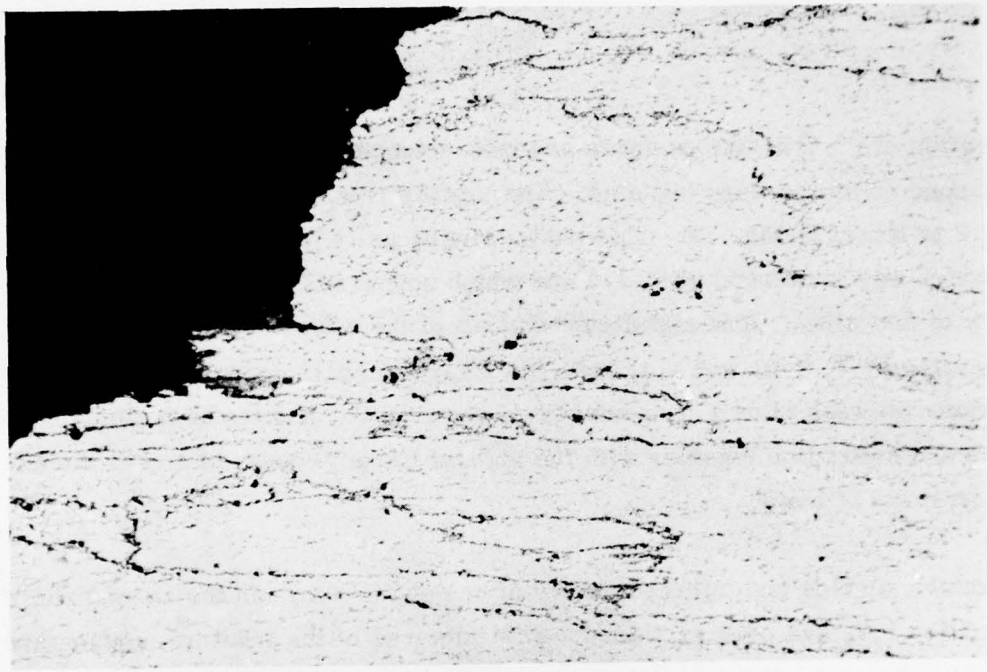

D9747 (a) 40 μm

D9751 (b) 10 μm

Figure 19. Al-3Li-2Cu-0.2Zr consolidated material solution treated 811 K (0.5 h), aged 464 K (8 h)

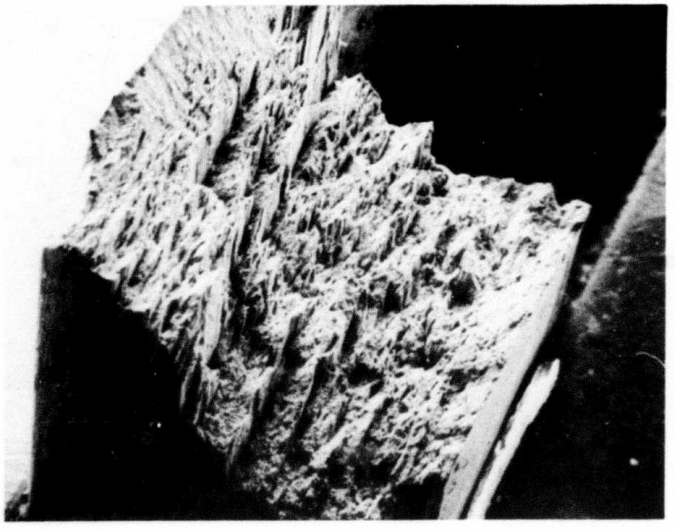

9IAQ (a) 1 mm

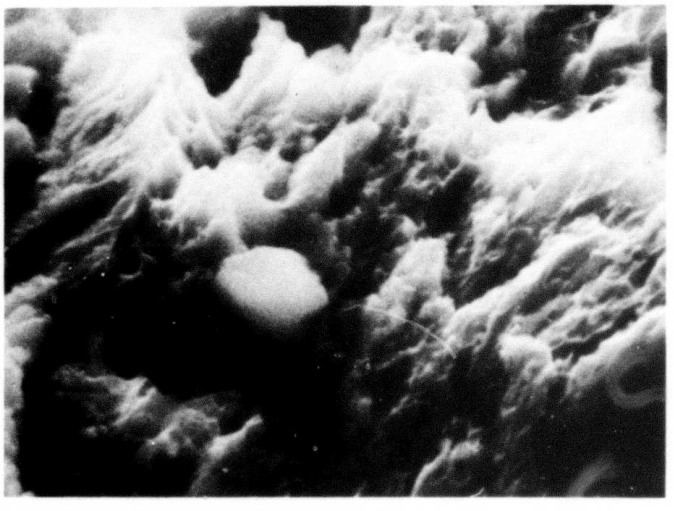

9IAX (b) 5 μm

Figure 20. Fracture surface of Al-3Li-0.5Fe-0.5Ni alloy

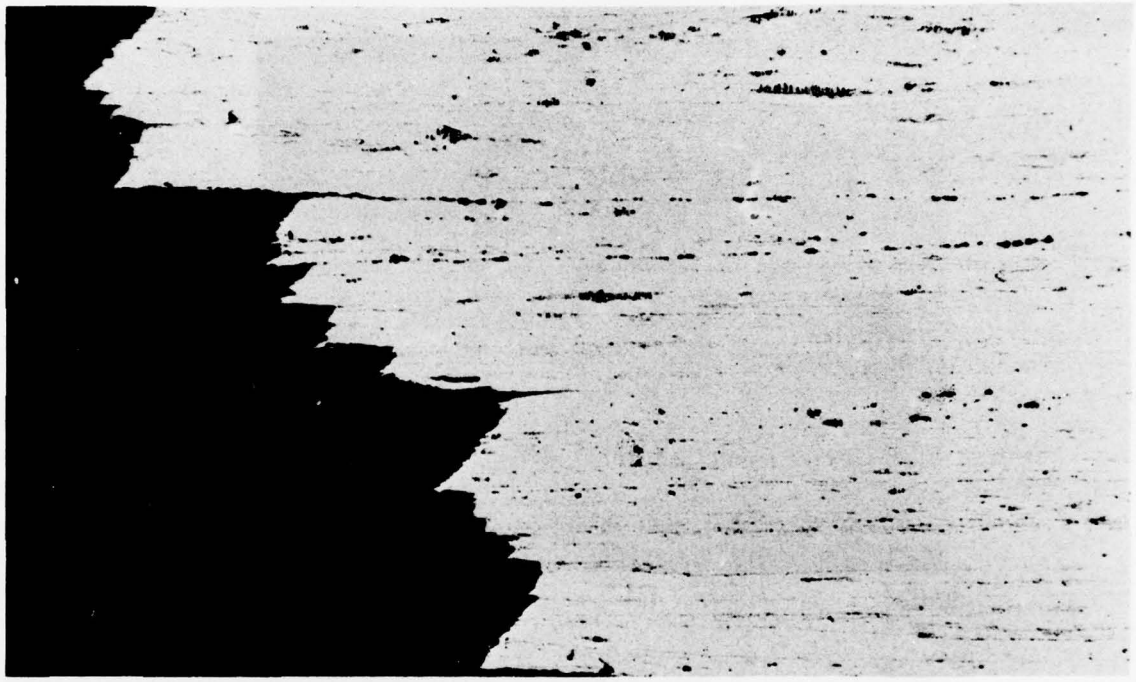

D9732 (a) 100 μm

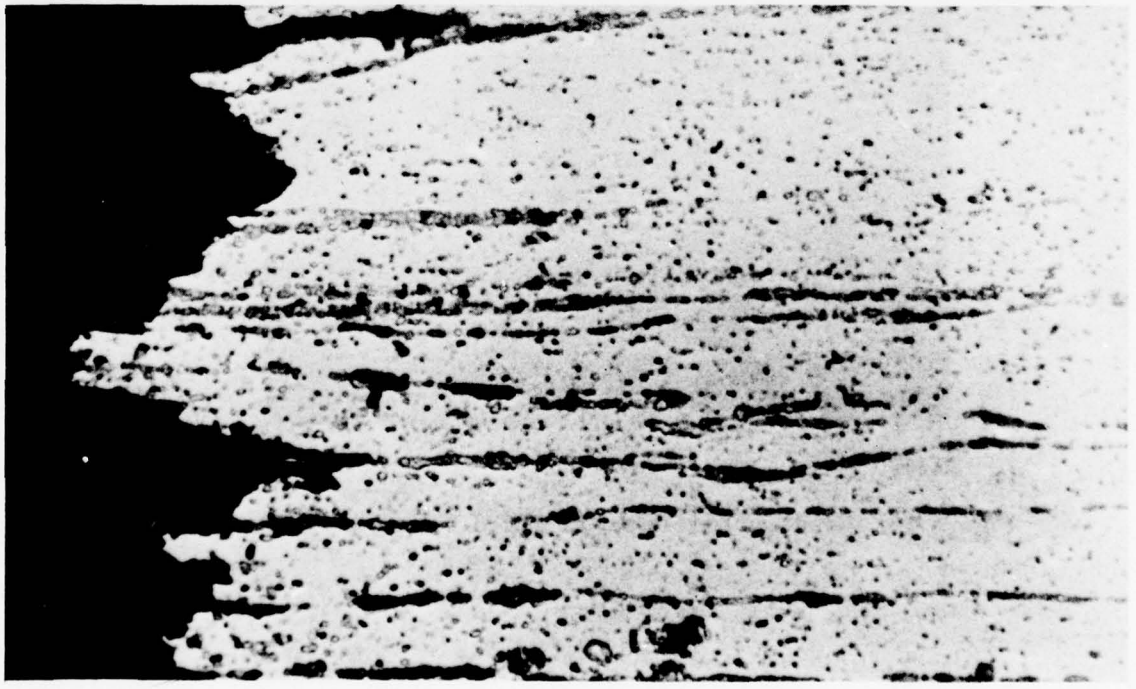

D9739 (b) 10 μm

Figure 21. Al-3Li-0.5Fe-0.5Ni consolidated material solution treated 811 K (0.5 h), aged 464 K (8 h)

2.2 TASK 2 – DEVELOPMENT OF NONLITHIUM-CONTAINING ALLOYS

Phase 1, Task 2, is being conducted by the Alcoa Laboratories as a parallel and complementary effort to the Al-Li alloy development activities (Task 1). Activities in this task are as follows:

- Subtask 1 – Alloy Selection (Two Systems, Four Compositional Variants Each)
- Subtask 2 – Manufacture of Particulates (Eight First-Iteration Alloys)
  - All eight by air atomized splat process
  - Several by argon atomized splat process
  - Several by air atomized powder process
- Subtask 3 – Powder and Splat Particulate Characterization
  - Chemical composition of melt
  - Screen fraction analysis
  - Particle morphology
  - Surface oxide content
  - Microstructure
- Subtask 4 – Deformation Processing Fundamentals (Splat and Powder)
  - Cold compaction
  - Hot compaction
- Subtask 5 – Phase Stability Studies
- Subtask 6 – Hydrogen Gas Evolution Studies
- Subtask 7 – First-Iteration Alloy Screening (Eight Splat, Four Powder Alloys)
  - Cold compaction
  - Hot compaction + extrusion (three process variations)
  - Mechanical property tests
  - Microstructural characterization
- Subtask 8 – Second-Iteration Alloy Screening (Two Systems, Two Variants Each)
  - Manufacture particulate (four splat, two powder alloys)
  - Billet consolidation
  - Direct billet rolling feasibility test
  - Extruded product fabrication
  - Property testing
  - Microstructural characterization

2.2.1 Selection of First Iteration Alloy Compositions

Alloy systems based on Al-Fe-Co, Al-Fe-Ni, and Al-Mn show high promise of producing a specific modulus of elasticity at least 30 percent greater than 7075 (Refs. 7, 8). Compositions selected for initial development are shown in Table 10. The alloy selections consist of two solute levels each in the Al-Fe-Ni-Co and Al-Mn-Si systems and each with two variations of solute ratio. This allows determination of the relative solute level required to obtain specific modulus values and to assess the relative efficacy of individual solute species in producing a high modulus second phase. These alloy systems are dispersion hardened and nonheat treatable. Because of their high solute content, casting by a rapid solidification process is dictated.

2.2.2 Generation of Powder and Splat Particulate

Both powder and splat particulates are produced using Alcoa's proprietary gas atomization technology.

TABLE 10. FIRST ITERATION OF NONLITHIUM-CONTAINING ALLOYS

Alcoa Alloy Designation	Target Melt Composition (wt %)
2.1A	Al-3.3Fe-3.4Ni-3.4Co
2.2A	Al-3.3Fe-2.3Ni-4.6Co
2.3A	Al-3.3Fe-4.6Ni-2.3Co
2.4A	Al-4.3Fe-5Ni-5Co
2.5A	Al-9.7Mn
2.6A	Al-9.7Mn-2.5Si
2.7A	Al-5Mn-5Si
2.8A	Al-14.2Mn

7. Unpublished research, Alcoa Laboratories, Alcoa Center, PA.
8. R. E. Sanders, Jr., G.J. Hildeman, and D. J. Lege, Elevated Temperature Al Alloy Development, AFML Contract F33615-77-C-5086, Technical Report for the Period Mar 29, 1978 to Mar 28, 1979.

In the fine atomized powder process, very small liquid droplets are generated by the interaction of high-pressure atomizing gas with the molten alloy. These molten metal droplets are then cooled by high-velocity room-temperature air which continuously conveys them to a cyclone collection chamber. Preheated air is used as the atomizing gas.

Alcoa's proprietary splat-making process combines gas atomization and single rotating quench-drum technologies. Atomized droplets are splat quenched against the rotating drum while they are still molten. Splat flakes rapidly solidified in this manner then spall off the drum surface. Collection of the splat flakes is accomplished by either one of two methods: (1) batch collection in a relatively static room temperature air or argon gas environment containing $\leq$6 percent oxygen or (2) continuous removal to the cyclone collection chamber by high-velocity room-temperature air. The various atomizing gas species include unheated or preheated air or unheated argon.

Table 11 lists the powder and splat materials generated to date for this task. A total of 1112 kg (2452 lb) of net product has been produced from 23 molten heats. Four atomized powder heats and three argon atomized splat heats are included for selected comparisons with the standard air atomized splat alloys. Disposition of each lot according to subtask, is included in Table 11. This material is sufficient for all first-iteration alloy evaluation tasks.

2.2.3 Powder and Splat Particulate Characterization

Actual Metal Compositions. In accord with standard powder metallurgy (PM) and aluminum industry procedures, melt chemistry is used as the best indicator of average particulate composition. Book mold samples are taken from the molten metal prior to atomization. Preliminary spectrographic analyses are performed immediately, with atomic absorption determinations performed subsequently to obtain final alloy compositions. Additional tests, particularly oxygen content by FNA analysis and Auger profile analysis of surface films, are performed for comprehensive characterization of the loose particulate. Chemical composition of the resultant wrought products is also determined. Certified

TABLE 11. NONLITHIUM-CONTAINING ALLOYS POWDER AND SPLAT PARTICULATE PRODUCTION INFORMATION

Alcoa Alloy	Type	Pot No.	S No.	Min. Melt Temp. (K)	Net Wt. (kg)	Contract Subtask Number
2.1A	Splat[a]	2145	S513656	1366	5	3
2.1A	Splat[b]	2187	S513700	1310	55.4	3, 5, 7
2.2A	Powder	2173	S513682	1065	30	3, 4, 5, 6, 7
2.2A	Splat[c]	2174	S513687	1188	13.8	3, 4, 7
2.2A	Splat[b]	2189	S513702	1310	123	3, 4, 5, 6, 7
2.3A	Splat[b]	2188	S513701	1366	48	3, 5, 7
2.4A	Splat[b]	2186	S513697	1310	41.8	3, 5, 7
2.4A	Powder	2180	S513683	1310	25	3, 7
2.5A	Splat[a]	2148	S513660	1310	30	3
2.5A	Splat[a]	2149	S513661	1310	37.7	3
2.5A	Splat[c]	2175	S513686	1199	24.1	3, 7
2.5A	Splat[b]	2191	S513704	1310	61.8	3, 5, 7
2.6A	Splat[d]	2150	S513662	1255	22.7	3, 4, 5
2.6A	Splat[d]	2151	S513663	1255	66	3, 4, 5
2.6A	Splat[d]	2152	S513664	1255	82	3, 4, 5
2.6A	Powder	2154	S513666	1144	158	3, 4, 5, 6, 7
2.6A	Splat[c]	2176	S513689	1227	27.7	3, 5, 6, 7
2.6A	Splat[b]	2192	S513705	1310	58.6	3, 5, 7
2.7A	Splat[b]	2193	S513706	1310	50	3, 5, 7
2.8A	Splat[a]	2146	S513658	1255	33	3
2.8A	Splat[a]	2147	S513659	1188	29.5	3, 4
2.8A	Powder	2168	S513678	1310	24	3, 4, 5, 7
2.8A	Splat[b]	2190	S513703	1310	64.5	3, 5, 7

Note: All powder hot-air atomized with cyclone collection.

(a) Cold-air atomized splat. Batch collection without cyclone.

(b) Hot-air atomized splat with cyclone collection.

(c) Cold-argon atomized splat. Batch collection without cyclone.

(d) Cold-air atomized splat with cyclone collection.

Alcoa alloy melt compositions are reported in Table 12 for the 23 heats from which splat and powder particulate were generated.

Screen Fraction Analysis. Random samples of each powder and splat particulate lot have been processed using conventional Tyler Ro-Tap equipment. Table 13 reports the weight percent of particulates produced within each screen fraction.

Splat flakes produced with the batch collection mode generally have significant weight fractions (>20%) in the coarsest (+8) screen size. By contrast, splat produced through the continuous cyclone collection system benefits from mechanical attrition inherent in high-velocity air conveyance. Weight of particulate in the coarsest screen fraction is reduced by a factor of 10. Adjustments in the proprietary splat atomizing practice offers some flexibility in varying molten metal droplet sizes, but the minimum permissible droplet size is limited by the need to minimize or preclude "inflight" solidification of droplets before impacting against the rotating quench drum.

Since "inflight" solidification is intended in atomized powder production, very small liquid metal droplets [10-15 μm Average Particle Diameter (APD)] are desirable. These are readily achieved, as indicated by screen fraction analyses of the powder heats (Table 13). As is typical of Alcoa's fine atomized powder, more than 90 percent of the product falls in the -325 size [44 μm (1.7×10^{-3} in.)] range. APD values of 11.5 to 13.6 μm (4.5 to 5.3×10^{-4} in.) given in Table 13 were determined with a Fisher Sub-Sieve Sizer. Note that an APD determination is not applicable to splat flakes. A more meaningful parameter for splat flake is thickness as measured metallographically.

Morphology of Splat Particulate – Optical Microscopy. The splats are roughly circular flakes, approximately 15 to 25 μm ($5.9 - 9.8 \times 10^{-4}$ in.) thick, with one side of the flake being highly specular (drum side).

The +8 screen fraction typically consists of large ($\geq$4 mm), irregularly shaped flakes with thicknesses in the range of 10 to 50 μm. Most of this fraction is splat, having

TABLE 12. CHEMICAL COMPOSITION OF NONLITHIUM-CONTAINING ALLOY MELTS (wt%)

Alcoa Alloy	Pot No.	S No.	Cu	Fe	Si	Mn	Mg	Zn	Cr	Ti	Ni	Co
2.1A	Target			3.27							3.44	3.45
	2145	513656	0.00	3.08	0.2	–	–	–	–	–	3.32	3.23
	2187	513700	0.00	3.36	0.09	0.01	0.00	0.02	0.00	0.00	3.43	3.54
2.2A	Target			3.27							2.28	4.59
	2173	513682	0.01	3.16	0.04	0.03	0.00	0.02	0.00	0.00	2.21	4.43
	2174	513687	0.01	3.09	0.04	0.03	0.00	0.01	0.01	0.00	2.20	2.94
				2.97							2.14	3.67
	2189	513702	0.01	3.23	0.07	0.00	0.00	0.02	0.00	0.00	2.32	4.02
2.3A	Target			3.27							4.57	2.29
	2188	513701	0.00	3.34	0.08	0.01	0.00	0.02	0.00	0.00	4.40	2.42
2.4A	Target			4.77							5.00	5.03
	2180	513683	0.02	4.73	0.13	0.04	0.01	0.04	0.01	0.01	4.81	4.59
	2186	513697	0.00	4.88	0.12	0.01	0.00	0.03	0.00	0.00	5.14	5.23
2.5A	Target					9.68						
	2148	513660	0.01	0.07	0.1	9.85	0.01	0.00	0.00	0.00	0.00	–
	2149	513661	0.01	0.07	0.2	10.5	0.01	0.00	0.00	0.00	0.01	–
	2175	513686	0.00	0.06	0.05	10.6	0.00	0.00	0.00	0.00	0.00	–
	2191	513704	0.00	0.09	0.06	10.2	0.00	0.00	0.00	0.00	0.00	–
2.6A	Target				2.47	9.68						
	2150	513662	0.00	0.08	2.18	10.0	0.01	0.00	0.00	0.01	0.01	–
	2151	513663	0.00	0.08	2.34	9.88	0.01	0.00	0.00	0.01	0.01	–
	2152	513664	0.00	0.07	2.39	9.40	0.01	0.00	0.00	0.01	0.01	–
	2154	513666	0.03	0.08	2.44	9.65	0.01	0.00	0.00	0.00	0.01	–
	2176	513689	0.00	0.06	2.35	10.3	0.00	0.00	0.00	0.00	0.00	–
	2192	513705	0.00	0.10	2.23	9.82	0.00	0.00	0.00	0.01	0.01	–
2.7A	Target				5.06	4.95						
	2193	513706	0.00	0.12	4.35	5.41	0.00	0.00	0.00	0.01	0.00	–
2.8A	Target					14.17						
	2146	513658	0.00	0.08	0.09	13.6	0.01	0.01	0.00	0.00	0.02	–
	2147	513659	0.01	0.08	0.09	14.2	0.00	0.00	0.00	0.01	0.01	–
	2168	513678	0.01	0.08	0.05	15.0	0.00	0.01	0.00	0.01	0.00	–
	2190	513703	0.01	0.08	0.05	14.2	0.00	0.01	0.00	0.00	0.01	–

TABLE 13. SCREEN FRACTION ANALYSES OF NONLITHIUM-CONTAINING ALLOY POWDER AND SPLAT PARTICULATE

Alcoa Alloy	Type	S No.	Screen Size – U.S. Standard (wt % in Each Size Range)								APD (μm)
			+8	- 8 +16	-16 +30	-30 +50	- 50 +100	-100 +200	-200 +325	-325	
2.1A	Splat[a]	513656	1.4	11.6	15.6	25.2	22.5	14.2	5.0	4.2	
2.1A	Splat[b]	513700	2.2	11.0	10.0	15.6	10.6	14.2	10.0	26.2	
2.2A	Powder	513682	0	0	0	trace	trace	1.6	4.4	93.8	11.5
2.2A	Splat[c]	513687	33.4	29.2	13.8	13.6	2.4	6.0	0.6	0.8	
2.2A	Splat[b]	513702	0.4	3.2	6.0	11.6	6.0	16.4	15.8	40.4	
2.3A	Splat[b]	513701	1.4	10.0	11.2	18.5	7.4	15.6	10.8	22.0	
2.4A	Splat[b]	513697	0.6	6.8	13.4	24.4	16.7	11.2	8.6	18.0	
	Powder	513683					trace	1.4	4.4	94.1	11.2
2.5A	Splat[a]	513660	21.8	26.2	14.8	19.0	11.1	5.4	0.8	0.8	
2.5A	Splat[a]	513661	36.1	32.2	14.6	10.2	4.4	1.9	0.3	0.1	
2.5A	Splat[c]	513686	24.8	43.8	18.2	9.4	2.4	0.8	0.2	0.2	
2.5A	Splat[c]	513704	2.4	12.0	13.0	18.2	9.0	16.4	8.8	21.0	
2.6A	Splat[d]	513662	3.4	38.0	28.8	20.4	12.8	4.2	1.2	1.0	
2.6A	Splat[d]	513663	3.6	37.1	24.1	20.7	9.9	3.1	0.7	0.8	
2.6A	Splat[d]	513664	2.8	26.6	25.5	25.5	12.7	4.7	1.2	0.8	
2.6A	Powder	513666	0	0	0	trace	trace	2.2	6.2	91.4	14.6
2.6A	Splat[c]	513689	28.0	40.0	18.6	9.4	0.4	2.8	0.4	0.4	
2.6A	Splat[b]	513705	1.8	10.0	12.4	19.0	15.0	12.2	8.8	20.6	
2.7A	Splat[b]	513706	2.6	12.6	13.0	18.4	6.6	21.2	9.2	17.0	
2.8A	Splat[a]	513658	23.3	23.6	16.0	17.7	9.7	4.0	2.1	3.4	
2.8A	Splat[a]	513659	27.0	35.0	18.0	14.0	4.0	1.0	0.5	0.5	
2.8A	Splat[b]	513703	1.6	10.8	10.8	15.6	14.3	13.4	11.0	22.6	
2.8A	Powder	513678	0	0	0	0	trace	1.4	5.2	93.3	13.0

(a) Cold-air atomized splat. Batch collection without cyclone.

(b) Hot-air atomized splat with cyclone collection.

(c) Cold-argon atomized splat. Batch collection without cyclone.

(d) Cold-air atomized splat with cyclone collection.

solidified quite rapidly, and is typified by fine dendritic and nondendritic morphology. It does contain thicker flakes having entrapped gas voids and some large nonsplat particles. Some of the thicker flakes consist of several overlapping thinner flakes. Typical cross sections of these various types are shown in Fig. 22. Due to the large planar size which may cause problems in consolidation and the presence of both nonsplat particles and particles with voids, this screen fraction is excluded from the particulate used in subsequent consolidation.

The +16 screen fraction consists of individual flake particulate on the order of 10 to 20 μm (0.4 to 0.8 x 10^{-4} in.) thick. The flakes are again irregularly shaped, either circular or ellipical, and approximately 2 to 3 mm (0.125 in.) in diameter. Some multiple layered splats containing entrapped gas voids are present in all the alloys, particularly 2.1A and 2.4A, but fewer than in the +8 screen fraction. Typical examples of morphology of the +16 screen fraction are shown in Fig. 23. The microstructure of the Al-Fe-Ni-Co alloys is featureless, even after prolonged chemical etching, while the Al-Mn (Si) alloys, which are featureless in the as-polished condition, are dendritic as revealed by etching. The lack of microstructural features shown in optical microscopy of the Al-Fe-Ni-Co alloys does not mean there is an absence of precipitation, as both Guinier x-ray analysis and transmission electron microscopy (TEM) show the presence of a variety of precipitates.

In the +30 to +100 screen fractions, the flake thickness is 10 μm (0.4 x 10^{-4} in.) or less and planar dimensions are about 1 to 2 mm (~0.06 in.) in the +30 mesh and about 0.1 mm (4 x 10^{-3} in.) in the +100 mesh fraction. As shown in Fig. 24, some in-flight solidified (nonsplat) particulate is present in these screen fractions.

In the +200 screen fraction, the flake thickness is about 5 to 10 μm (1.95 to 3.9 x 10^{-4} in.) and most flakes are nondendritic; however, there is a larger amount of inflight solidified particulate than in the coarser screen fractions (Fig. 25). The Al-Mn-Si compositions and hot air atomized lots of various compositions have more inflight solidified particulate than the other lots.

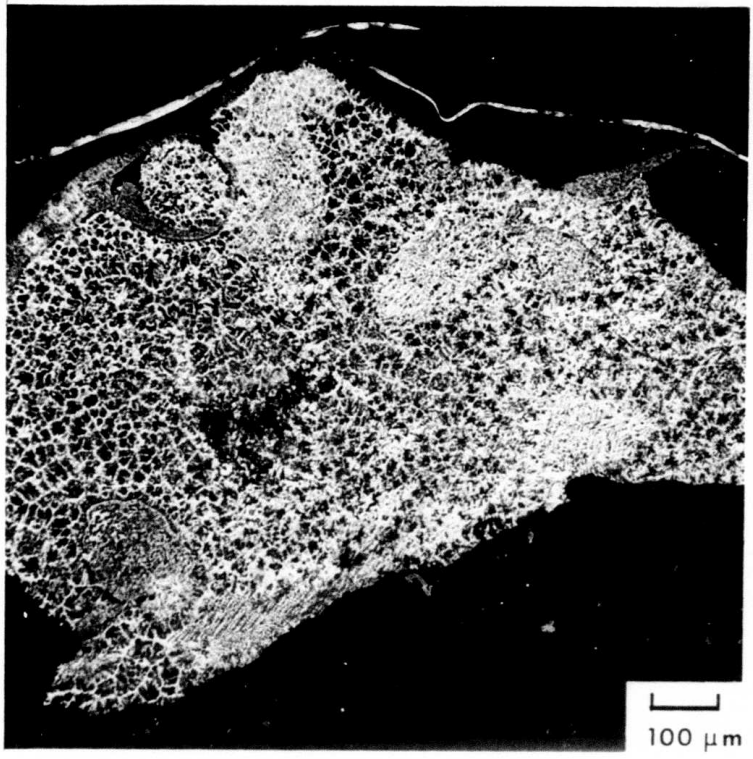

(a)

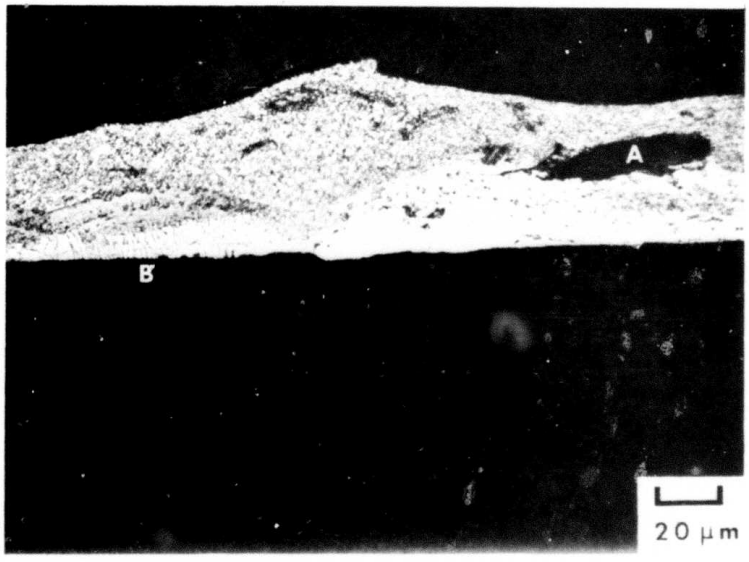

(b)

Figure 22. Optical microstructure of +8 screen fraction particulate: (a) splat and nonsplat in alloy 2.5A (Al-10Mn) and (b) gas void at "A", columnar structure at "B" in splat of alloy 2.8A (Al-14.2Mn)

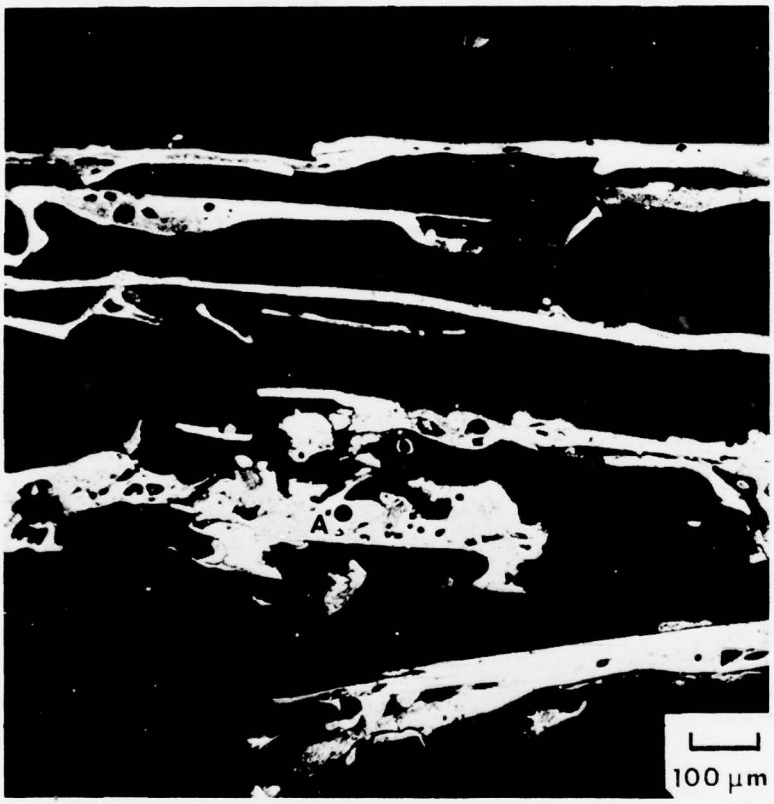

Figure 23. Optical microstructure of alloy 2.4A (Al-4Fe-5Ni-5Co) typical splat particulate in +16 screen fraction. Note example of gas voids at "A"

In the +325 and -325 screen fractions, a high proportion of the particulate is inflight solidified (nonsplat) particulate, and is highest in the -325 fraction. Typical examples from a splat lot are shown in Fig. 26(a). This particulate is not typical of Alcoa fine atomized powder, see Fig. 26(b). It has a larger size (Alcoa fine atomized powder typically has an APD of 9 to 15 μm) and lower solidification rate. The inflight solidified particulate produced in the splat process often consists of multiple droplets welded together.

Table 14 compares weight distribution in alloy 2.6A for both hot and cold atomizing air splat generation. Heating the atomizing air clearly reduces the weight fraction in screen sizes of +50 and larger and significantly increases the weight fraction of splat

TABLE 14. EFFECT OF ATOMIZING AIR TEMPERATURE ON WEIGHT DISTRIBUTION OF SPLAT ALLOY 2.6A, Al-10Mn-2.5Si

Mesh	Cold Air With Cyclone Wt Fraction (%)	σ_{n-1} (%)	Hot Air With Cyclone Wt Fraction (%)
+8	3.3	0.4	1.8
+16	33.9	6.3	10.0
+30	26.1	2.4	12.4
+50	22.2	2.9	19.0
+100	11.8	1.6	15.0
+200	4.0	0.8	12.2
+325	1.0	0.3	8.8
-325	0.9	0.1	20.6

TABLE 15. EFFECT OF CYCLONING ON WEIGHT FRACTION OF SPLAT

Mesh	Alloy 2.5[(a)] Without Cyclone Wt Fraction (%)	σ_{n-1} (%)	Alloy 2.6[(b)] With Cyclone Wt Fraction (%)	σ_{n-1} (%)
+8	29.0	10.1	3.30	0.40
+16	29.2	14.2	33.90	6.30
+30	14.7	0.1	26.10	2.40
+50	14.6	6.2	22.20	2.90
+100	7.8	4.7	11.8	1.6
+200	3.7	2.5	4.0	0.8
+325	0.6	0.4	1.0	0.3
-325	0.5	0.5	0.9	0.1

(a) Al-10 Mn
(b) Al-10 Mn-2.5 Si

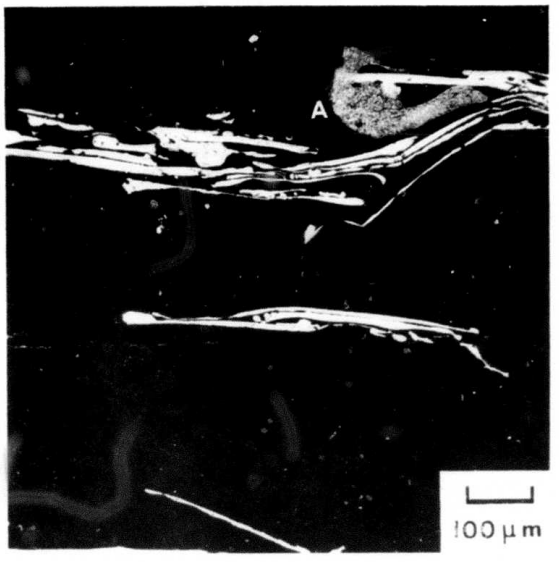

(a)

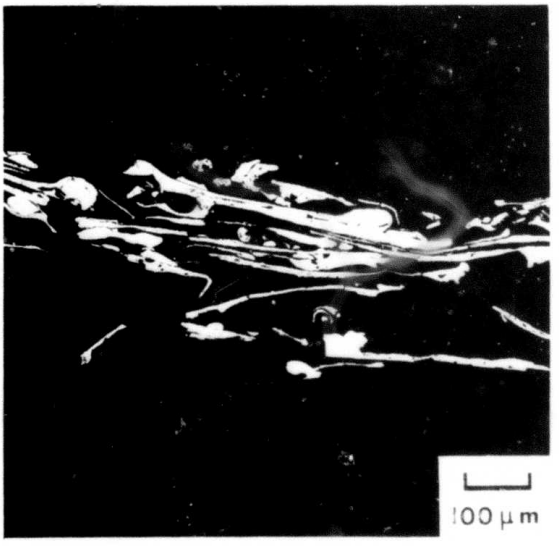

(b)

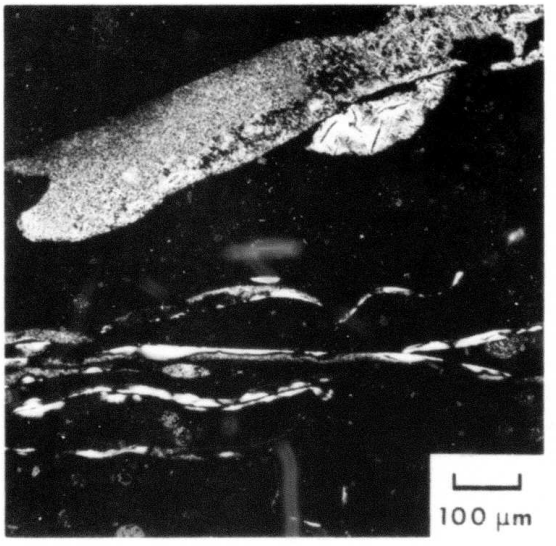

(c)

Figure 24. Optical microstructure of typical splat particulate in +50 screen fraction: (a) alloy 2.1A (Al-3Fe-3Ni-3Co), showing predominantly featureless structure; inflight solidified particulate at "A", (b) alloy 2.4A (Al-4Fe-5Ni-5Co), and (c) alloy 2.6A (Al-10Mn-2.5Si)

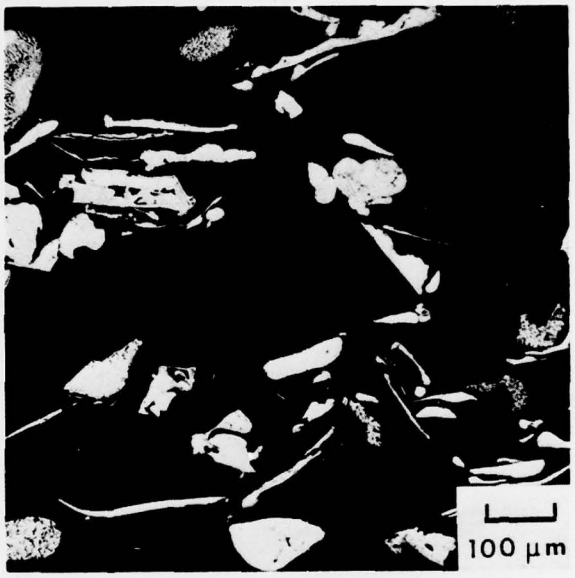

Figure 25. Optical microstructure of particulate in +200 screen fraction of alloy 2.1A (Al-3Fe-3Ni-3Co). Note predominance of inflight solidified particulate

and inflight solidified (nonsplat) particulate in screen sizes of +200 and smaller. smaller. Table 15 shows the distribution of particulate in two runs without cyclone collection for alloy 2.5A and three runs with cyclone collection for alloy 2.6A. Cyclone collection apparently breaks down multiple layered splats in the +8 fraction and re-distributes them into the +16 to +50 screen fractions, with only a small weight change occurring in the smaller screen fractions.

Based on these observations and subsequent Guinier analyses, only -8/+200 size particulate is included in the first iteration alloy screening studies (Subtask 7). Selective processing of the entire range of splat flake sizes produced will be investigated in Subtask 4.

Oxygen Content. Representative samples of powder and splat particulate lots were analyzed to determine oxygen content. Results are shown in Table 16. Although oxygen determination by the FNA technique is usually accurate and reproducible, these

TABLE 16. FAST-NEUTRON ACTIVATION OXYGEN ANALYSES OF NONLITHIUM-CONTAINING ALLOY POWDER AND SPLAT PARTICULATE

Alcoa Alloy	Pot No.	S No.	Type	Oxygen (wt %)
2.1A	2187	513700	Splat-Hot Air	0.495
2.2A	2173	513682	Powder-Hot Air	0.548
	2174	513687	Splat-Cold Argon	0.276
	2189	513702	Splat-Hot Air	4.035 – 0.167*
2.3A	2188	503701	Splat-Hot Air	0.543
2.4A	2186	513697	Splat-Hot Air	0.445
	2180	513693	Powder-Hot Air	0.549
2.5A	2148	513660	Splat-Cold Air	0.702
	2149	513661	Splat-Cold Air/Cyclone	0.393
	2175	513686	Splat-Cold Argon	0.389
	2191	513704	Splat-Hot Air	0.461
2.6A	2150	513662	Splat-Cold Air/Cyclone	0.441
	2151	513663	Splat-Cold Air/Cyclone	0.491
	2152	513664	Splat-Cold Air/Cyclone	0.621
	2154	513666	Powder-Hot Air	0.466
	2176	513689	Splat-Cold Argon	0.415
	2192	513705	Splat-Hot Air	0.519
2.7A	2193	513706	Splat-Hot Air	0.595
2.8A	2146	513658	Splat-Cold Air	0.487
	2147	513659	Splat-Cold Air	0.359
	2168	513678	Powder-Hot Air	0.479
	2190	513703	Splat-Hot Air	3.495 – 0.177*

*Original results were suspect; analysis of duplicate samples appears to be low.

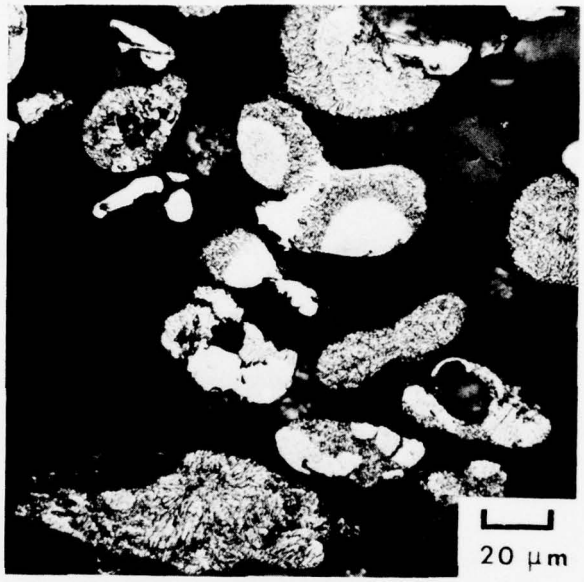

(a)

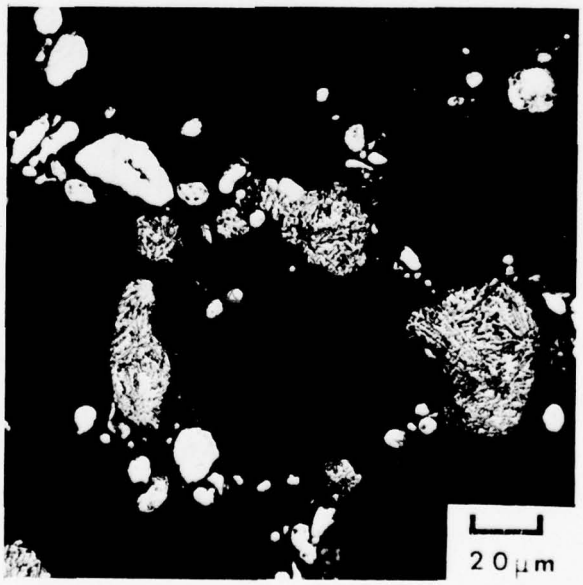

(b)

Figure 26. Optical microstructure of alloy 2.4A (Al-4Fe-5Ni-5Co) in -325 screen fractions: (a) predominance of inflight solidified particulate in a splat lot and (b) typical fine atomized powder

data contain unexplained irregularities. Oxygen contents of the powder materials fall within an anticipated 0.4 to 0.5 wt% range. Alcoa's prior work found splat flakes usually have only half the oxygen content of comparable alloy composition fine atomized powder. In the present data, oxygen content of most splat lots equals or exceeds those of the conventionally produced fine atomized powder. Even more puzzling are the discrepancies between FNA determinations of duplicate lot samples, specifically Pot numbers 2189 and 2190. Additional FNA tests are now being planned in conjunction with surface area evaluation of selected flake screen fractions. Auger and SIMS/ISS studies of the oxide layer on particle surfaces have not been completed.

Guinier-deWolff X-Ray Analysis of Loose Particulate. Mixtures of +100 and +200 screen fractions of splat particulate, and the -325 screen fraction of atomized powder were examined separately with a Guinier-deWolff camera using Cu Kα x-radiation. The results are presented in Table 17. Little variation exists in the amount of $(FeNiCo)_2Al_9$ in the splat alloys 2.1A to 2.4A, and in the atomized powder sample of alloy 2.2A. In atomized powder of the Al-Mn alloys 2.6A and 2.8A, there are both different phases and greater amounts of the same phases found in splat of the same compositions. The predominant phases in the as-cast Al-Mn(Si) alloys are Mn_3SiAl_{12} and $MnAl_6$. Although not expected initially, it is now known that as low as 0.03 wt% Si can stabilize Mn_3SiAl_{12}. This phase was not identified previously because of displaced line positions; however, reexamination suggests the observed line shifts are probably due to small diffracting domain size and different solute content due to rapid solidification.

The trial alloy, Al-6Mn, and alloy 2.8A, Al-14Mn, were examined to determine the relative amount of precipitated phases in different screen fractions. These results are summarized in Table 18. Solid solution in the +8 to +100 screen fractions appears to be consistently retained and is probably also retained in the +200 screen fraction splat particulate but not in the inflight solidified particulate found in the +325 screen fraction.

TABLE 17. GUINIER ANALYSES OF AS-PRODUCED NONLITHIUM-CONTAINING ALLOY PARTICULATE

Alloy	Pot No.	S No.	Material[a]	Alloy Content (wt %)			Phases Detected by Guinier Analysis			
				Fe	Ni	Co	M_2Al_9[b]	Mn_3SiAl_{12}	$MnAl_6$	Si
2.1A	2187	513700	S	3.36	3.43	3.54	med+			
2.2A	2189	513702	S	3.23	2.32	4.02	med			
2.2A	2173	513682	P	3.16	2.21	4.43	med			
2.3A	2188	513701	S	3.34	4.40	2.42	med-			
2.4A	2186	513697	S	4.88	5.14	5.23	med			
				Mn	Si					
2.5A	2191	513704	S	10.2				v.small+	v.small-	
2.6A	2192	513705	S	9.82	2.23			med	v.small+	
2.6A	2154	513666	P	9.65	2.44			med+[c]		poss.trace
2.7A	2193	513706	S	4.95	5.06			med	trace	v.small+
2.8A	2146	513658	S	13.6				small+[c]		
2.8A	2168	513678	P	15.0				large[c]	poss.trace	

(a) S - splat, mixture of +200 and +100 particulate; p - powder, -325 particulate.
(b) M denotes (Fe, Ni, Co).
(c) Identification is tentative.

TABLE 18. GUINIER ANALYSES OF SELECTED SCREEN FRACTIONS OF Al-Mn ALLOY SPLAT PARTICULATE

Alloy*	Screen Fraction	Phases Detected by Guinier Analysis	
		$MnAl_6$	Mn_3SiAl_{12}
2.8A	+8		Medium
2.8A	+30		Small+
Al-6 Mn	+30		V. Small+
2.8A	+100		Small+
Al-6 Mn	+100	poss. trace	Small-
Al-6 Mn	+325	poss. v. small	Small

*2.8A is Al-14 Mn; Al-6 Mn is a "trial" alloy

Previous Guinier analyses of Alcoa fine-atomized powder indicate fine-atomized powder has less retained solid solution than splat particulate of the same composition. Because the fine inflight solidified particulate found in the splat lots is even coarser in size than the conventionally produced fine-atomized powder, the solidification of the inflight solidified powder will be slower, and less solid solution will be retained. Optical metallography supports this expectation. Since the amount of inflight solidified particulate is considered excessive in screen fractions smaller than +200, only +200 and coarser fractions will be used for further processing when retention of solid solution is an important consideration. If changes in particulate manufacture can be made to reduce the amount of product in the +200 and smaller fractions, the +200 fraction should also be excluded from further processing.

Transmission Electron Microscopy (TEM) of Splat Particulate. TEM examination was conducted on loose flakes in the +8 screen fraction, thinned by conventional twin-jet electropolishing foil-preparation techniques. Guinier analysis shows the phase distribution in these flakes to be reasonably representative of flakes in the -8/+100 screen fractions. TEM examination of flakes in the +8 size fraction involves some complications in interpretation. As some flakes are multiple layered, the position of foils prepared from such flakes cannot be located confidently with respect to individual flake thickness. In addition, some flakes exhibit a transition from non-dendritic to dendritic part way through the thickness. The nondendritic structure initiates at the surface contacting the quench drum, and proceeds outward by planar or cellular solidification. The cellular structure has also been described as a columnar structure (Ref. 4). As solidification proceeds, liquid undercooling decreases to where the solidification mode changes to dendritic. Transition to dendritic solidification may also be initiated heterogeneously by impurities or primary crystals of a second phase. Of course, dendritic solidification may also be initiated at the drum surface. In comparing dendritic structures, changes in center to center spacing of dendrite arm spacing is used to infer differences in solidification rate. Note that alloy content also affects this spacing.

Alloys 2.1A, 2.2A, 2.3A, and 2.4A have similar microstructures, even though the Ni:Co ratio and total solute content vary significantly. As shown in Fig. 27, the solidification structure is "cellular" with complex inner features. As Guinier analyses indicate, only $(FeNiCo)_2Al_9$ precipitation is present in this alloy, the two structures observed must both consist of this precipitate. The "cellular" structure comprises fine lamellae with a spacing of about 0.1 μm ($4x10^{-6}$ in.) [Fig. 27(b)]. At the core of the "cell" is a poorly resolved structure, partly lost by electropolishing in Fig. 27(a). In some cells it appears as a rosette (Fig. 28), and in other cells, no such structure exists. This feature is probably a single crystal of $(FeNiCo)_2Al_9$, which may provide sites for heterogeneous nucleation of dendrites (Ref. 9). A possible spatial relation of the various structures found by TEM examination is shown schematically in Fig. 29. In such a microstructure, the smallest precipitate spacing achievable is the lamellar spacing, assuming subsequent heat treatment can spheroidize the structure without coarsening it.

TEM examination of alloy 2.5A, Al-10Mn, splat flakes reveals a rather uniform dendritic structure, illustrated in Fig. 30. Cellular features found by optical microscopy were not found by TEM, probably because an insufficient volume of material is sampled by TEM. Both Mn_3SiAl_{12} and $MnAl_6$ phases are probably present in the dendrite interstices, as both phases were detected by Guinier analysis. The average dendrite arm spacing is 0.64 μm, indicating a solidification rate of approximately 10^6 K/s.

Alloy 2.6A has the same nominal composition as 2.5A, with an addition of 2.5Si. Optical microscopy of 2.6A reveals the presence of a small amount of cellular structure, less than in 2.5A. TEM examination of 2.6A found only dendritic structure, illustrated in Fig. 31 The dendrite arm spacing in this alloy is 0.1 to 0.25 μm, significantly finer than in alloy 2.5A. Guinier analyses have shown that the addition of Si to Al-Mn alloys reduces the ability to maintain supersaturated solid solution in the rapidly solidified flakes. From conventional casting experience, the addition of Si increases fluidity of the melt. As the same splat-making procedures were used for alloys 2.5A

---

9. J. P. Hirth, "Nucleation, Undercooling and Homogeneous Structures in Rapidly Solidified Powders," Met. Trans. Vol. 9A, 1978, p 401-404.

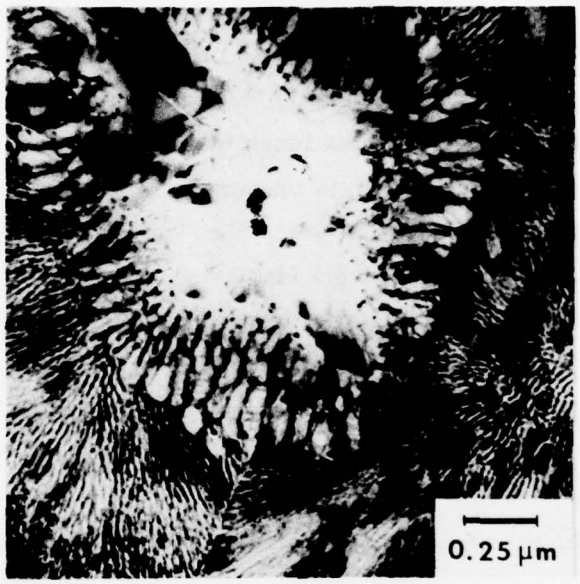

(a)

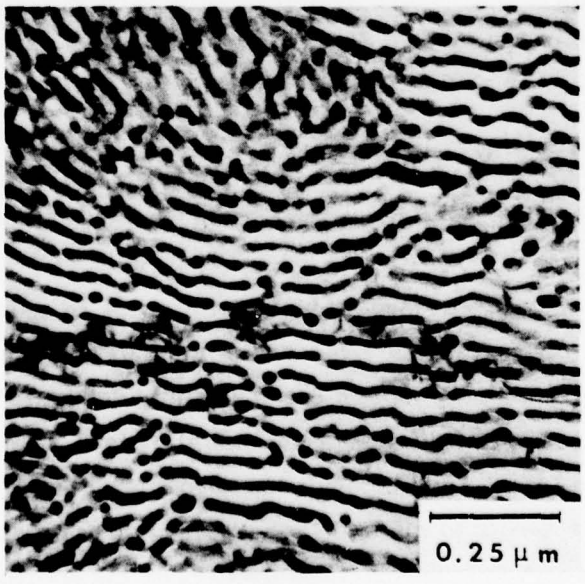

(b)

Figure 27. TEM of splat alloy 2.1A (Al-3Fe-3Ni-3Co): (a) primary Co_2Al_9 particle surrounded by fine cellular structure (b) higher magnification shows lamellar nature of cellular structure

Figure 28. TEM of splat alloy 2.1A (Al-3Fe-3Ni-3Co) showing rosette-shaped primary crystal of $(FeNiCo)_2 Al_9$

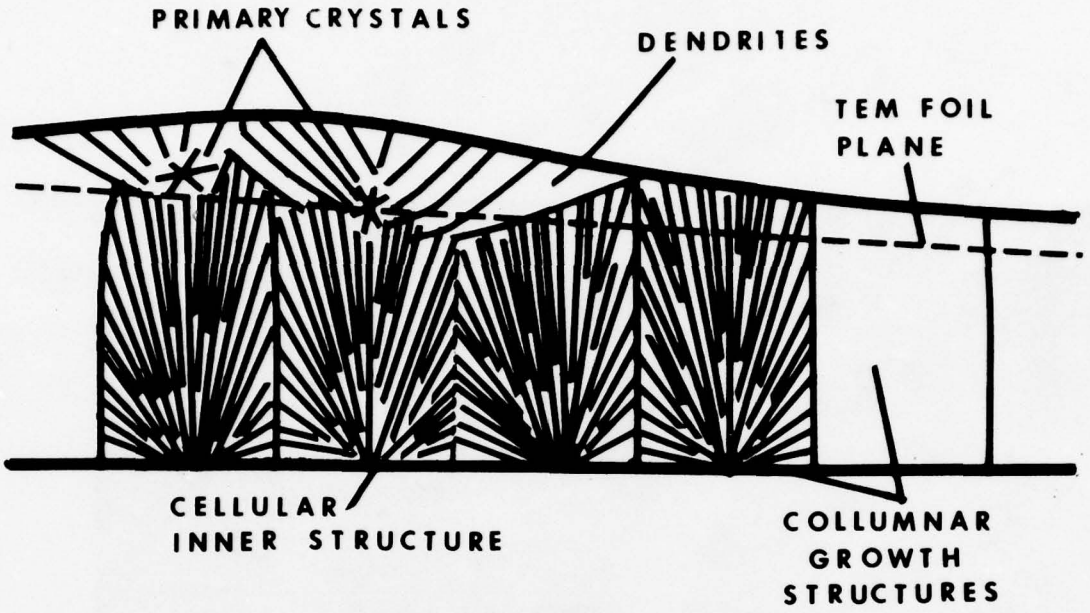

Figure 29. Schematic of splat structures shown in Figs. 27 and 28; probable position of TEM foil plane is indicated

and 2.6A, the finer dendritic spacing in the latter may be due to the Si addition promoting either formation of thinner flakes due to increased droplet fluidity and which would solidify more rapidly, or nucleation and growth of dendrites due to the decreased solubility, or both of these.

TEM examination of alloy 2.7A, Al-5Mn-5Si, reveals a dendritic structure similar in spacing to alloy 2.5A, but with a large amount of Mn_3SiAl_{12} and some free Si precipitated in the dendrite interstices. A typical microstructure is shown in Fig. 32.

TEM examination of alloy 2.8A, Al-14Mn, reveals both dendritic and cellular structures, typical examples of which are shown in Fig. 33. The cellular structure is similar to that found in alloys 2.1A-2.4A. Guinier analysis has found the presence of only one second phase in this alloy identified tentatively as Mn_3SiAl_{12}. The various forms in which this compound exists in alloy 2.8 apparently include (1) interdendritic precipitate, (2) lamellar eutectic structure in the cellular regions, and (3) rosettes at dendrite core

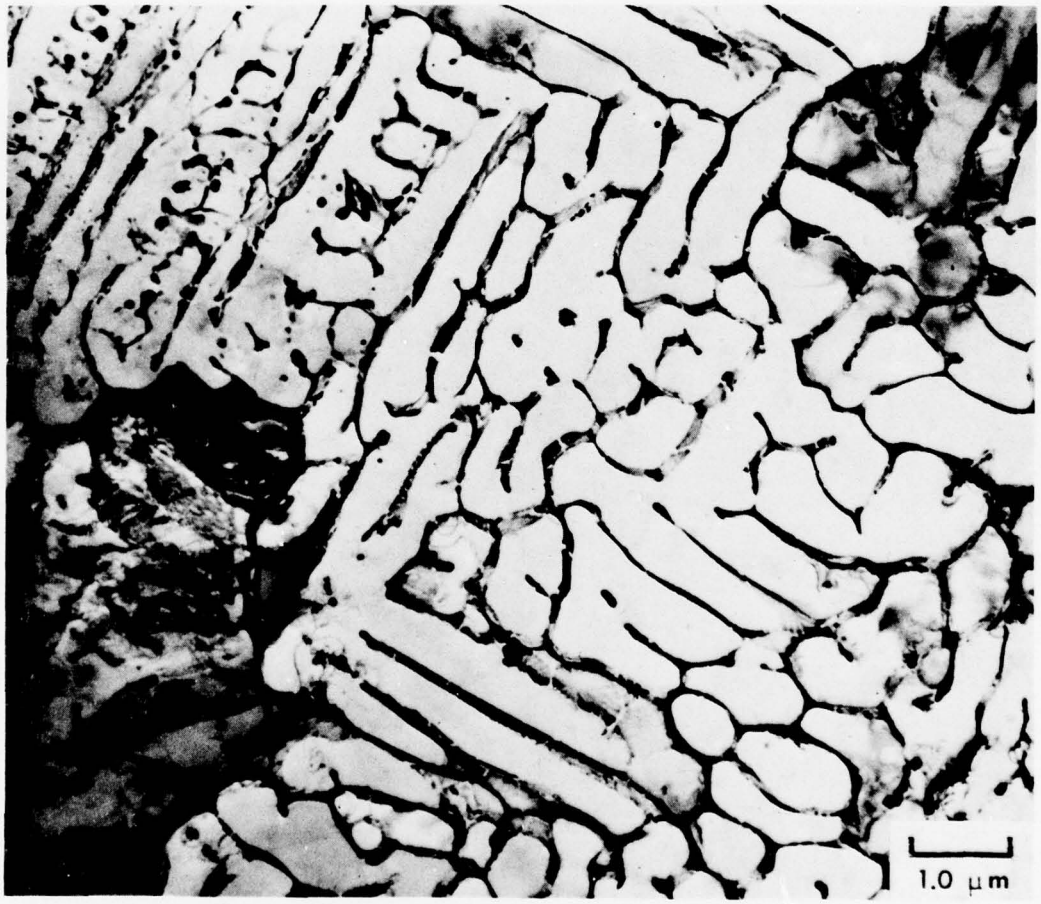

Figure 30. TEM of splat alloy 2.5A (Al-10Mn) showing typical dendritic structure

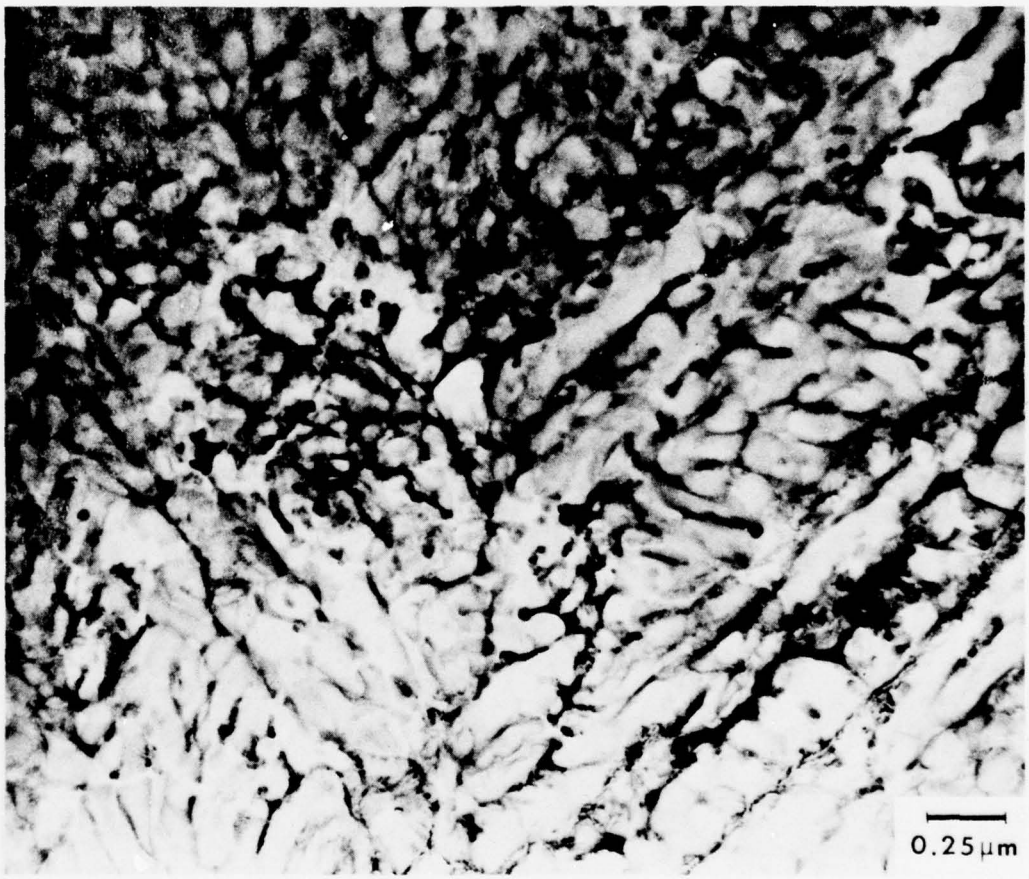

Figure 31. TEM of splat alloy 2.6A (Al-10Mn-2.5Si) showing typical dendritic structure

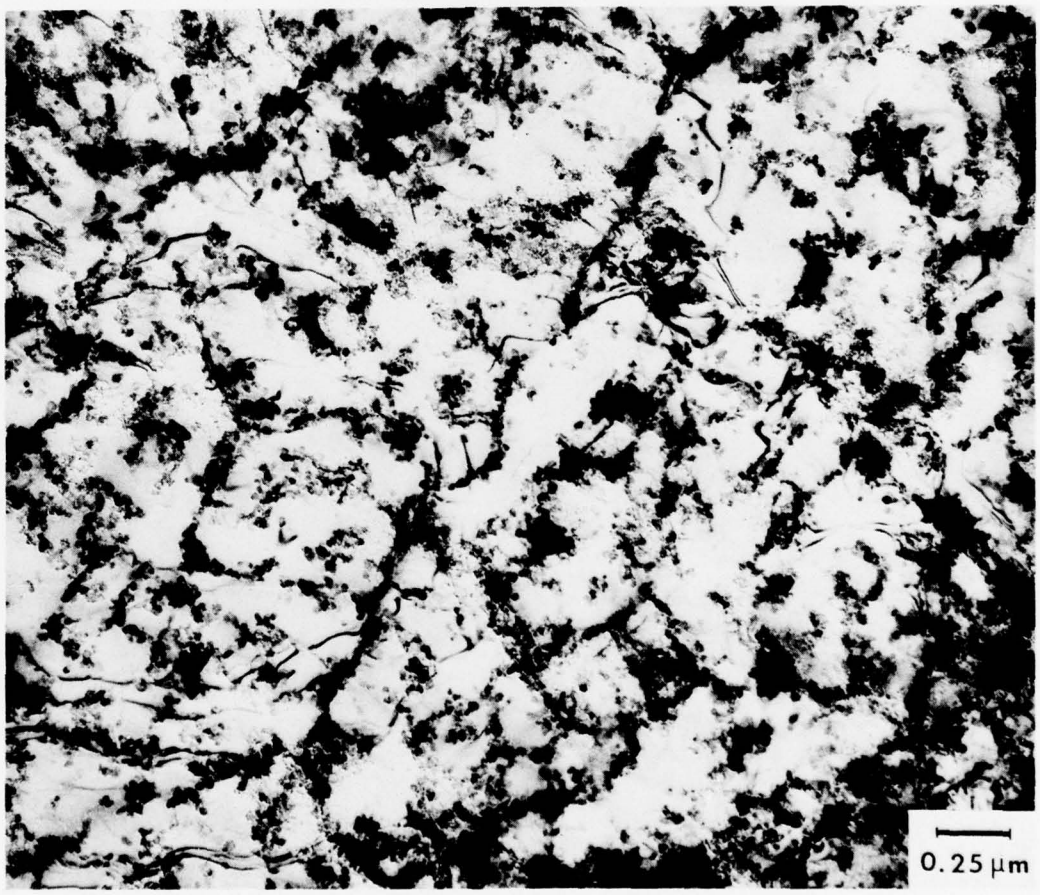

Figure 32. TEM of splat alloy 2.7A (Al-5Mn-5Si) showing typical dendritic structure

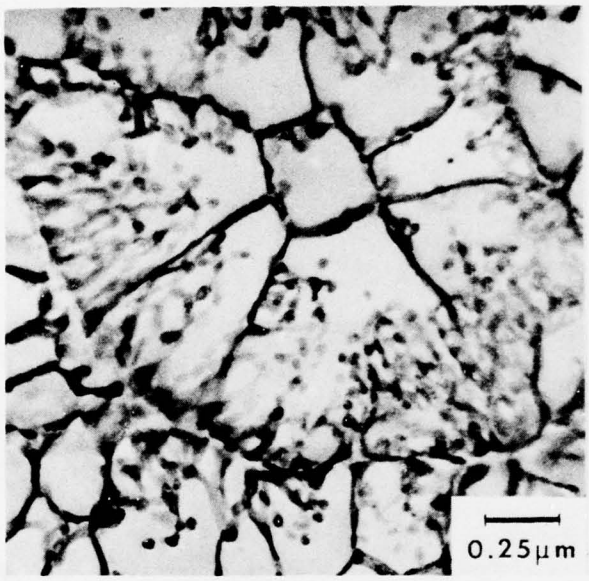

(a)

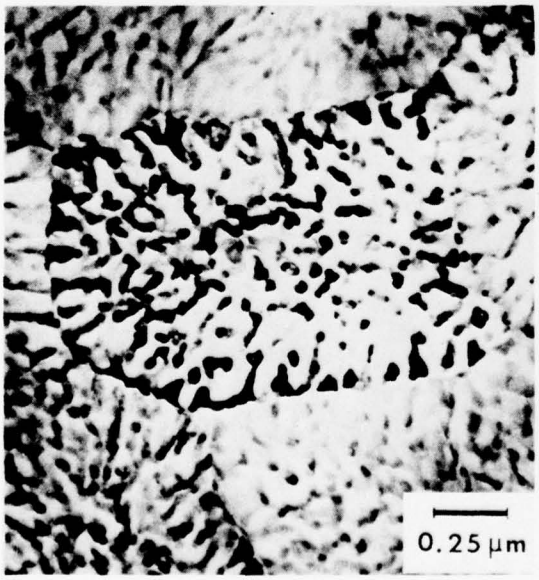

(b)

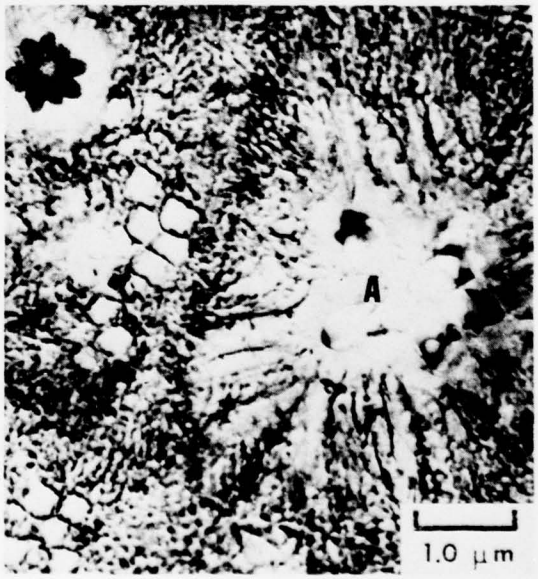

(c)

Figure 33. TEM of splat alloy 2.8A (Al-14Mn):
(a) typical dendritic structure
(b) typical cellular structure
(c) nucleation of dendrites at primary crystals ("A")

regions. The rosette feature is not uncommon in rapidly solidified aluminum alloys, having been observed in other alloys in this study (Fig. 28, for example), and in Al-Pt alloys (Ref. 10). The rosettes are most likely a primary crystal of a high-temperature phase. Al_4Mn would be the logical equilibrium composition for this alloy, but was not detected by Guinier analysis. The phase $Al_{12}Mn_3Si$ may be a variant of the $Al_4(Mn,X)$ type, other examples being $Al_{20}Cu_2Mn_3$ and $Al_{60}Mn_{11}Ni_4$. The stoichiometry of $Al_{12}Mn_3Si$ is in question, as both $Al_{10}Mn_2Si$ and $Al_{21}Mn_3Si_5$ have also been cited (Refs. 11, 12). In any case, the phase could occur as primary crystals and which optical and electron microscopy suggests probably serve as dendrite nuclei.

In summary, the electron microscopy indicates the Al-Fe-Ni-Co splat particulate has solidified predominantly by a cellular rather than a dendritic mode. Within these cells, a fine lamellar structure exists, having a spacing of about 0.1 μm. For either solidification structure, a larger amount of second phase has precipitated in the Al-Fe-Ni-Co alloys, and the distribution is finer compared to the binary Al-Mn alloys. The Al-Mn binary alloys exhibit cellular and dendritic morphologies with dendritic spacings 0.5 to 0.75 μm. Second phase occurs as interdendritic precipitates, primary crystals, and fine lamellar structure. The addition of Si appears to promote precipitation, including free Si, and reduces the propensity for cellular solidification. The dendrite spacing is similar in both the Al-Mn and Al-Mn-Si alloys.

2.2.4 Deformation Processing Fundamentals

The effects of particle morphology, selected screen fractions, alloy composition, and surface oxide characteristics on cold compaction pressure and density variations will be evaluated for both powder and splat materials. How these factors affect vacuum hot compaction and particle bonding will then be evaluated.

---

10. K. Chattopadhyay and P. Ramachandrarao, "Metastable Phase Formation and Decomposition in a Rapidly Solidified Aluminum-Platinum Alloy," Mater. Sci. and Eng., Vol. 38, 1979, p 7-17.
11. W. B. Pearson, Handbook of Lattice Spacings and Structures of Metals, Pergamon Press, New York, 1958, p 375.
12. L. F. Mondolfo, Aluminum Alloys, Structure and Properties, Butterworths, Inc., Boston, 1976, p 594.

2.2.5 Phase Stability Studies

Since the nonlithium-containing alloys are dispersion hardened, it is important to anticipate any microstructural decomposition of the as-cast particulate during subsequent hot pressing and extrusion. Hot pressing and extrusion temperatures will probably be between 550 K (530°F) and 800 K (980°F), with the lower temperatures promoting efficient outgassing of the particulate. A matrix of temperature and time was selected to evaluate decomposition over this range. +8 splat and a mixture of +50 to +200 splats were wrapped separately in Al foil and exposed to temperatures of 575 K (575°F), 675 K (755°F), and 775 K (935°F) for 0.5, 5, and 50 h in an air furnace. Negligible oxidation occurred, except at 775 K, where some mild oxidation was observed. Guinier analysis was performed on the +50 to +200 screen fractions; TEM of the +8 splat was conducted selectively to investigate possible coarsening of precipitates.

The amount of $(FeNiCo)_2Al_9$ in alloys 2.1A, 2.2A, 2.3A, and 2.4A is not significantly affected by aging, as shown by the Guinier analysis results in Table 19.

TABLE 19. GUINIER ANALYSIS OF AGED LOOSE PARTICULATE: Al-Fe-Ni-Co ALLOYS

Exposure Condition	Amount of $(FeNiCo)_2Al_9$ Present*			
	2.1A	2.2A	2.3A	2.4A
0.5 h at 575 K (575°F)	med-	small+	small+	med-
5.0 h at 575 K	med	med-	med-	med+
50.0 h at 575 K	med+	med	med	med+
0.5 h at 675 K (755°F)	med	med-	med-	med-
5.0 h at 675 K	med+	med+	med	med+
50.0 h at 675 K	med+	med+	med+	med+
0.5 h at 775 K (935°F)	med	med+	med	med+
5.0 h at 775 K	med+	med+	med+	med+
50.0 h at 775 K	med+	med+	med+	med+
Unaged (reference)	med+	med	med-	med

*2.1A is Al-3Fe-3Ni-3Co; 2.2A is Al-3Fe-2Ni-4Co; 2.3A is Al-3Fe-4Ni-2Co; 2.4A is Al-5Fe-5Ni-5Co.

Consequently, the changes that might occur would be structure coarsening rather than precipitation, and will be revealed in on-going TEM examination.

Aging of the Al-Mn alloys 2.5A and 2.8A at 575 K for up to 50 h produces only a small amount of precipitation (Tables 20 and 21). At 675 K, however, a large amount of $MnAl_6$ is precipitated, and at 50 h $MnAl_{12}$ is precipitated, apparently at the expense of $MnAl_6$. At 775 K, a large amount of $MnAl_6$ is precipitated within 5 h in alloy 2.5A and 0.5 h in alloy 2.8A, and longer times apparently cause only coarsening of the already-formed precipitate. Microstructural appearance of the precipitation and coarsening produced by aging of these alloys is illustrated in Fig. 34. Aging at any of the three temperatures produces precipitation both within and between dendrites and cells.

The effects of aging of Al-Mn-Si alloys 2.6A and 2.7A on precipitation are shown in Tables 22 and 23. In alloy 2.6A, negligible precipitation is effected, except some increase in amount of Mn_3SiAl_{12}, at 675 and 775 K at the longer times. In alloy 2.7A, aging does not increase the amount of Mn_3SiAl_{12} but does increase the amount of Si precipitating.

Although examination of the aged structures is not complete, three sets of temperatures for vacuum hot degassing, hot compaction, and extrusion have been selected. These appear in Table 24. The lowest temperature is selected to minimize coarsening of precipitates and substructure, while the two higher temperatures, 675 K (756°F) and 775 K (936°F) (and with short aging times), are selected for increased degassing and precipitation.

2.2.6 Hydrogen Gas Evolution Studies

Activity has not been started on this subtask.

2.2.7 First-Iteration Alloy Screening

A materials and processing summary for this subtask is shown in Table 25.

TABLE 20. GUINIER ANALYSIS OF AGED LOOSE PARTICULATE: Alloy 2.5A, Al-10Mn

Exposure Condition	Amount of Phase		
	$MnAl_6$	$MnAl_{12}$	Mn_3SiAl_{12}
0.5 h @ 575 K (575°F)	–	–	small–
5.0 h @ 575 K	trace	–	small
50.0 h @ 575 K	small+	trace	small
0.5 h @ 675 K (755°F)	med	trace	pos.v.small–
5.0 h @ 675 K	large–	v.small+	pos.trace
50.0 h @ 675 K	large–	med+	pos.trace
0.5 h @ 775 K (935°F)	med+	pos.trace	pos.trace
5.0 h @ 775 K	large–	v.small–	pos.trace
50.0 h @ 775 K	large–	v.small–	pos.v.small–
Unaged (reference)	v.small–	–	v.small+

TABLE 21. GUINIER ANALYSIS OF AGED LOOSE PARTICULATE: Alloy 2.8A, Al-14Mn

Exposure Condition	Amount of Phases			
	$MnAl_6$	$MnAl_{12}$	Mn_2SiAl_{12} [a]	Mn_2SiAl_{12} [b]
0.5 h @ 575 K (575°F)	–	–	–	small
5.0 h @ 575 K	–	–	–	small+
50.0 h @ 575 K	large–	pos.trace	v.small	–
0.5 h @ 675 K (755°F)	large–	trace	–	–
5.0 h @ 675 K	large–	small–	–	–
50.0 h @ 675 K	med+	large–	–	–
0.5 h @ 775 K (935°F)	large–	–	–	–
5.0 h @ 775 K	large–	–	–	–
50.0 h @ 775 K	large–	–	–	–
Unaged (reference)	–	–	–	small+

(a) Typically observed lines.
(b) Second type observed with distorted line positions but tentatively identified as Mn_3SiAl_{12}.

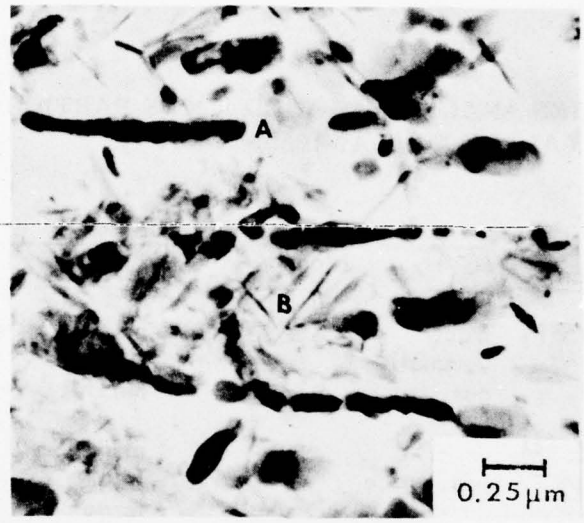

(a)

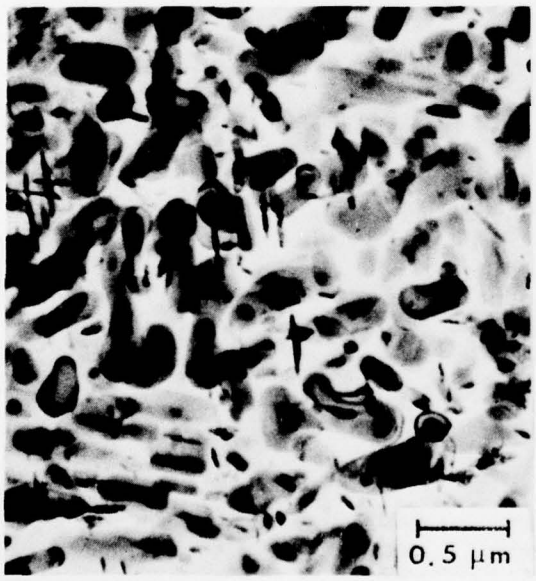

(b)

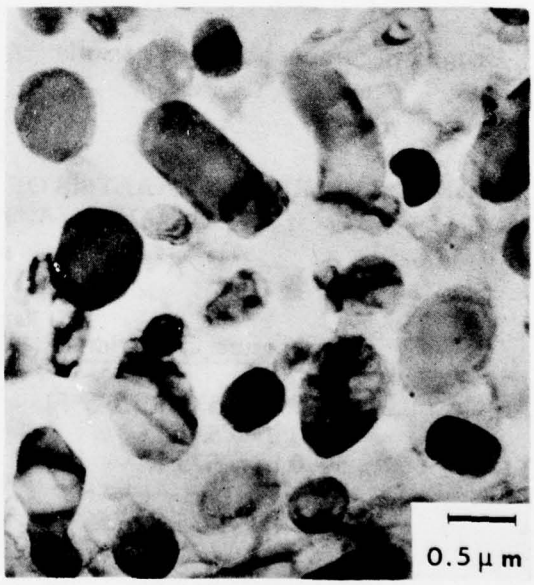

(c)

Figure 34. TEM of splats after aging:
(a) Alloy 2.5A (Al-10Mn), aged 675 K (5 h) showing inter- and intradendritic precipitation
(b) Alloy 2.8A (Al-14Mn), aged 675 K (5 h) showing increased precipitation of $MnAl_6$ and $MnAl_{12}$
(c) Alloy 2.5A, aged 775 K (50 h) showing coarsened precipitates of $MnAl_6$

TABLE 22. GUINIER ANALYSIS OF AGED LOOSE PARTICULATE: ALLOY 2.6A, Al-10Mn-2.5Si

Exposure Condition	Amount of Phase			
	$MnAl_6$	$MnAl_{12}$	Mn_3SiAl_{12}	Si
0.5 h @ 575 K (575°F)	trace	–	med-	trace
5.0 h @ 575 K	v. small+	–	med	–
50.0 h @ 575 K	pos. trace	–	med+	–
0.5 h @ 675 K (755°F)	–	–	med+	–
5.0 h @ 675 K	pos. trace	–	large-	–
50.0 h @ 675 K	–	v. small+	large-	–
0.5 h @ 775 K (935°F)	pos. trace	–	med+	–
5.0 h @ 775 K	trace	–	med+	–
50.0 h @ 775 K	v. small	–	large-	–
Unaged (reference)	v. small+	–	med	–

TABLE 23. GUINIER ANALYSIS OF AGED LOOSE PARTICULATE: ALLOY 2.7A, Al-5Mn-5Si

Exposure Condition	Amount of Phase	
	Mn_3SiAl_{12}	Si
0.5 h @ 575 K (575°F)	small+	small+
5.0 h @ 575 K	med-	med-
50.0 h @ 575 K	med	med-
0.5 h @ 675 K (755°F)	med-	med-
5.0 h @ 675 K	med-	med
50.0 h @ 675 K	med	med+
0.5 h @ 775 K (935°F)	med-	med
5.0 h @ 775 K	med	med+
50.0 h @ 775 K	med	med+
Unaged (reference)	med	v.small+

TABLE 24. THE TEMPERATURE SEQUENCES FOR HOT PRESSING AND EXTRUSION OF FIRST-ITERATION NONLITHIUM-CONTAINING ALLOYS

Sequence	Vacuum Outgassing and Hot Pressing Temperature	Extrusion Temperature
1	775 K (935°F)	575 K (575°F)
2	675 K (755°F)	675 K
3	675 K	575 K

Cold Compaction. Seven wet-bag isostatic compacts approximately 9 kg each were successfully made from atomized-powder variations of alloys 2.2A, 2.4A, 2.6A, and 2.8A. Isostatic compaction of splat was not successful. Prior experience at Alcoa indicated that soft rubber bags are pinched and punctured by the sharp-edged flakes and that thicker urethane molds also fail by localized sidewall strain during compaction of the low packing density flakes. A trial performance at Alcoa expense to evaluate a proprietary top closure of the urethane mold was also unsuccessful because of multiple sidewall tears.

Mechanical compaction of the cold splat flakes was then attempted, using as a container an extruded aluminum alloy canister positioned on a hard plate. At 27 MPa (4 ksi) the flakes compacted to about 38 percent density and the can sidewall buckled. At 69 Mpa (10 ksi) the compact density reached 45 percent, and a larger portion of the sidewall buckled. After three such compactions, this technique was discontinued as being impractical. Evaluation of these compacts indicated air was apparently trapped in some layers between the flakes. A different mechanical compaction procedure was then tried and was successful in producing all the required compacts. This method involved using a steel die equipped with a bottom knock-out. Compacts 2 to 6 cm thick and 50 to 70 percent density were made at a pressure of 172 MPa (25 ksi), then stacked inside extruded aluminum canisters with sufficient inside clearance for efficient hot degassing. The cold compacts obtained and their densities are listed in Table 26.

Hot Compaction. Generation of fully dense, hot-pressed splat and powder billets of the first-iteration alloys will be accomplished in the next reporting period followed by hot extrusion and evaluation of the extruded products.

TABLE 25. MATERIALS AND PROCESSING SUMMARY FOR FIRST-ITERATION NONLITHIUM-CONTAINING ALLOY SCREENING

Alcoa Alloy	Type Material	Alcoa Pot No.	No. of Compacts[a]	Hot Deformation Process Variations[b]
2.1A	Splat	2187	3	3
2.2A	Powder	2173	2	2
	Splat	2189	3	Same 3 as above
	Splat[c]	2174	1	One of the 3 above
2.3A	Splat	2188	3	3
2.4A	Splat	2186	3	3
	Powder	2180	1	One of the 3 above
2.5A	Splat	2191	3	3
	Splat[c]	2175	1	One of the 3 above
2.6A	Powder	2154	3	3
	Splat	2192	3	Same 3 as above
	Splat[c]	2176	2	Two of the 3 above
2.7A	Splat	2193	3	3
2.8A	Splat	2190	3	3
	Powder	2168	1	One of the 3 above
			35 Total	

(a) Nominally 9 kg, 149 mm diameter, cold compacts encapsulated in evacuation canisters for dynamic vacuum preheating to selected hot compaction temperatures.

(b) Each compact vacuum preheated and hot pressed at one of two selected temperatures in the 561 to 797K range. Hot-pressed billets machined to remove outer can material then extruded at one of two selected temperatures in the 561 to 797K range.

(c) Argon-atomized splat as contrasted with standard air-atomized powder and splat materials.

TABLE 26. COLD DIE COMPACTION OF NONLITHIUM-CONTAINING ALLOY SPLAT FLAKES

Alcoa Alloy	S No.	Density of Compact (g/cm^3)	Theoretical Density (g/cm^3)	Amount of Theoretical Density (%)
2.1A	513700	1.6	2.9	55
2.2A	513702	1.6	2.9	55
	513687	1.8	2.9	62
2.3A	513701	1.7	2.9	59
2.4A	513697	1.5	3.0	50
2.5A	513704	2.0	2.88	69
	513686	1.8	2.88	62
2.6A	513705	1.8	2.86	63
	513689	1.8	2.86	63
2.7A	513706	1.7	2.76	61
2.8A	513703	1.9	2.97	64

Note: compact pressure = 172 MPa (25 ksi); compact diameter = 11.4 cm (4.5 in.)

2.3 TASK 3 – QUANTITATIVE MICROSTRUCTURAL ANALYSIS AND MECHANICAL PROPERTY CALCULATIONS

This task is being conducted by the Georgia Institute of Technology.

A limited amount of two alloys produced from splat particulate was available in extruded bars for investigation of microstructures, mechanical behavior, and other properties. The two alloys are alloy 1.1 (Al-4Cu-3Li) and alloy 1.6 (Al-3Li-1.5Mn). Whenever possible, comparisons are made between these powder metallurgy (PM) and corresponding ingot metallurgy (IM) alloys. These results are preliminary and exploratory in nature, as insufficient material was available for extensive testing and analysis. However, the procedures developed now will be useful for later analyses.

2.3.1 Characterization of Microstructure

The microstructural studies include light-optical photomicrographs, and transmission electron microscopy (TEM) photographs of as-extruded or solution-heat-treated (SHT) foils from PM materials. Figure 35 presents orthogonal views of PM alloy 1.6 and an IM alloy Al-Li-Mn having the same nominal composition (Ref. 13). The pronounced differences in grain size and shape make property comparisons difficult; however, the basic microstructural quantities should serve to clarify observed differences in properties. Table 27 summarizes metallographic measurements made on LT-planes, similar to those shown in Fig. 35 (vertical planes on the right).

TABLE 27. SUMMARY OF QUANTITATIVE MICROSTRUCTURAL MEASUREMENTS ON SHT PM AND IM Al-Li ALLOYS (LT-PLANES)

	S_v (cm^2/cm^3)	Degree of Orientation Ω_{12} (%)	Mean Intercept Length $\bar{L}$ (μm)
PM Alloy 1.1	364	59	11
PM Alloy 1.6*	340	68	12
IM Alloy Al-Li-Mn*	22	13	182

*Same nominal composition.

Thin foils for TEM examination were prepared from PM alloy 1.6 in the as-extruded and SHT conditions. A general view of the microstructure in the as-extruded condition is shown in Fig. 36. This is representative of an unrecrystallized recovered microstructure. The four or five adjoining crystals in the center of Fig. 36 were shown by electron diffraction to have quite similar spatial orientations. Thus, we may assume that crystals of this size (about 1.5 μm) are subgrains rather than grains.

The particles in alloy 1.6 for the as-extruded and SHT conditions were compared. Figure 37 is a representative sampling of the two conditions at a high magnification. In general, the particles appear more angular, or polygonal, in the as-extruded condition than in the SHT condition, where the particles are more rounded. The

13. E. J. Coyne, Jr. and E. A. Starke, Jr. (unpublished research).

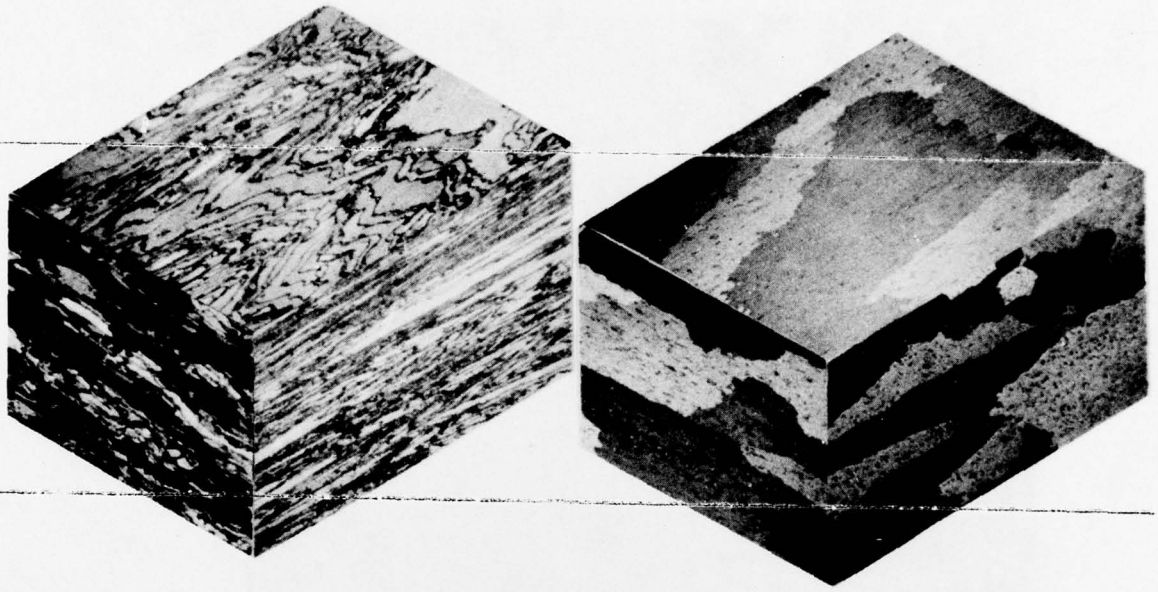

(a) (b)

Figure 35. Orthogonal views of PM alloy 1.6 and comparable composition IM Al-Li-Mn alloy

Figure 36. Transmission electron micrograph of PM alloy 1.6 in the as-extruded condition

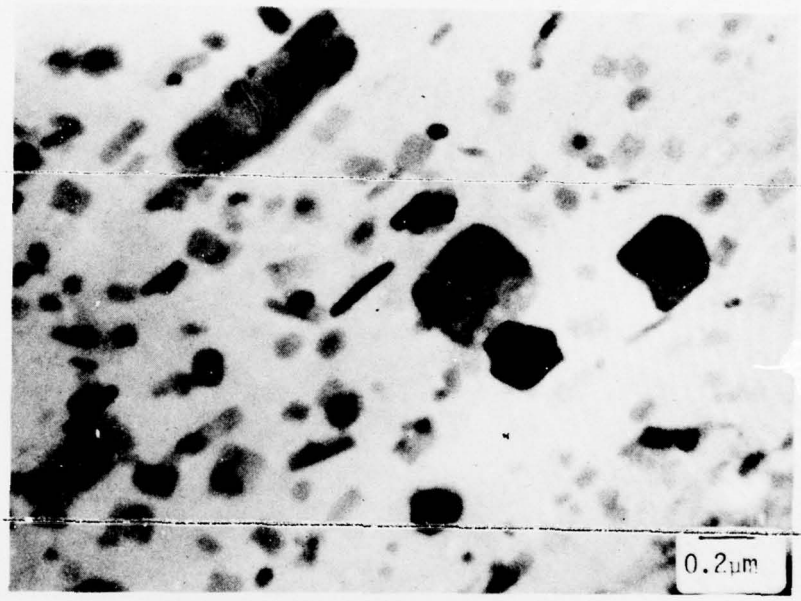

(a)

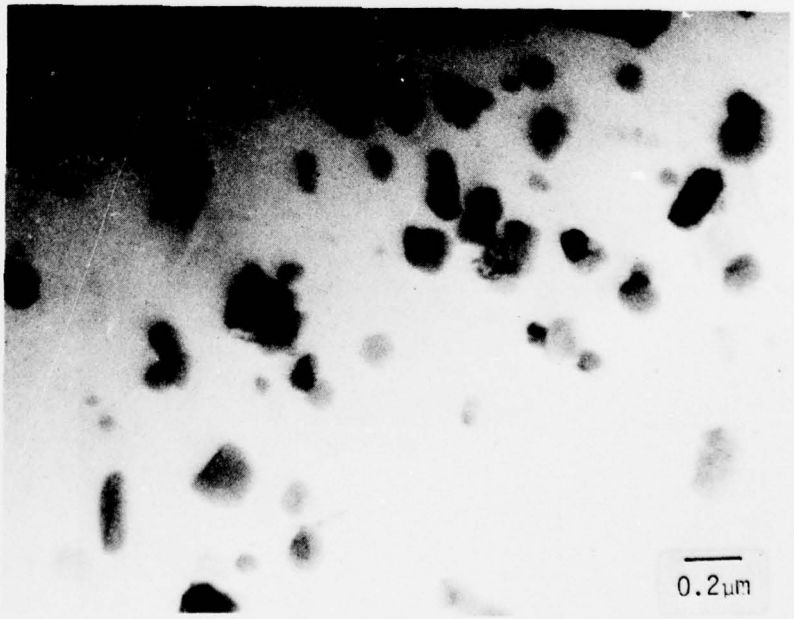

(b)

Figure 37. Transmission electron micrographs of PM alloy 1.6: (a) as-extruded and (b) solution-heat-treated

difference in size between large and small particles is greater in the as-extruded condition than in the SHT condition. The numerical ratio of "small" to "big" particles is about 15 in the as-extruded condition, while this ratio is about 10 in the SHT condition.

Crystallographic texture in the form of pole figures was obtained for PM alloy 1.1 in the as-extruded condition, and for PM alloy 1.6 in the as-extruded SHT conditions. A Siemens automated goniometer was used on 2.54 cm^2 coupons, with 1,200 readings taken per run. Analysis and plots of the data were made using a computer program developed at Georgia Institute of Technology.

Pole figures for the (111), (200), and (220) planes in PM alloy 1.1 are shown in Fig. 38. In Fig. 39, textures in PM alloy 1.6 are compared with those obtained from an IM Al-Li-Mn alloy of similar composition, in both the as-extruded and SHT conditions. Note the well-defined and sharp texture in both the PM and IM alloys. The textures are almost the same for the PM and IM extruded alloys even though the extrusion ratios were quite different – 8:1 for the PM and 35:1 for the IM materials. A saturation in crystallographic texture apparently occurs at a low extrusion ratio, and the possibility of obtaining random texture in extrusions of the PM material is minute.

The high elastic modulus and low density of the Al-Li alloys is due to a large volume fraction of coherent, shearable, and ordered Al_3Li precipitates. The shearable nature of the precipitates results in strain localization and large stress concentrations at grain boundaries in IM products, which may cause the low ductility and intergranular failure commonly observed in these products (Ref. 6). One approach for minimizing strain localization and homogenizing slip is to reduce the grain size (Ref. 14), and the PM product has an extremely fine grain size. However, the PM alloy has a very sharp texture, and the low mismatch in orientation between adjacent grains and subgrains suggests their boundaries will not provide strong barriers for slip (Ref. 15).

---

14. E. A. Starke, Jr., and G. Lütjering, Fatigue and Microstructure, M. Meshii, ed., American Society for Metals, Metals Park, Ohio, 1979, p. 205.

15. R. E. Sanders, Jr., and E. A. Starke, Jr., "The Effect of Intermediate Thermomechanical Treatments on the Fatigue Properties of a 7050 Aluminum Alloy," Met. Trans., Vol. 9A, 1978, p. 1087.

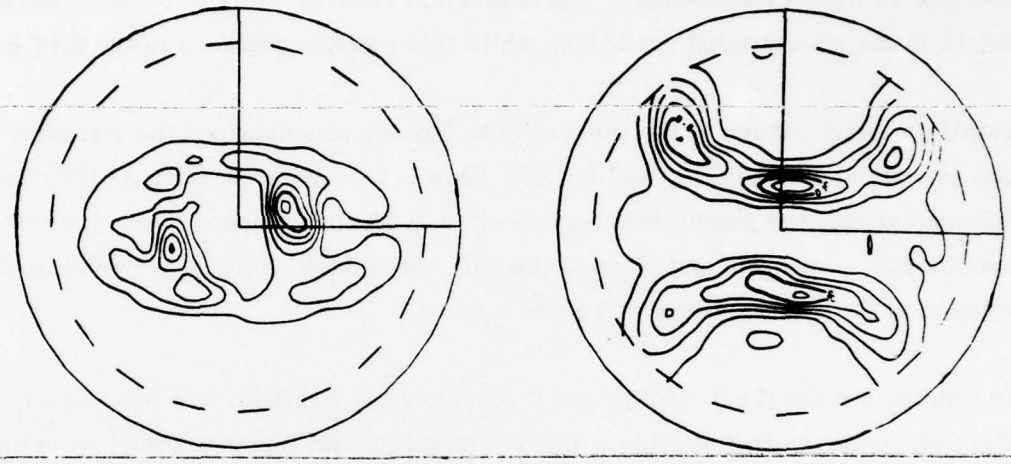

1.1 As Extruded (111)

1.1 As Extruded (200)

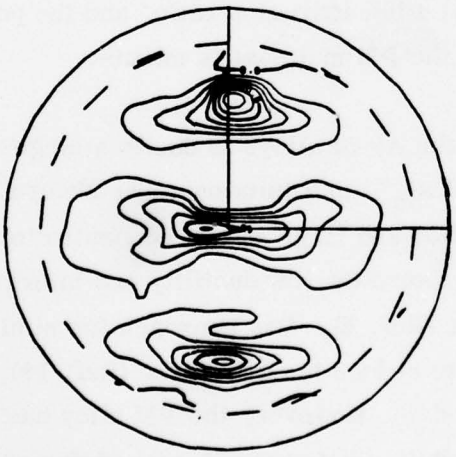

1.1 As Extruded (220)

Figure 38. Pole figures of as-extruded PM alloy 1.1 on (111), (200), and (220) planes

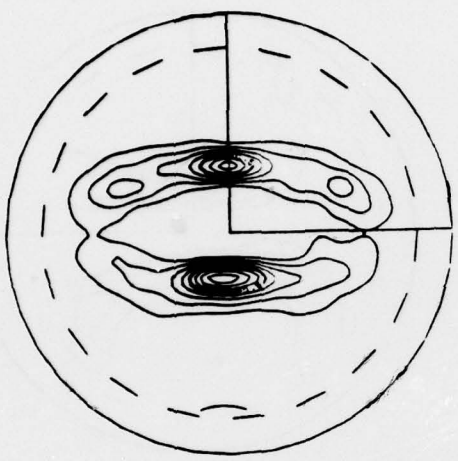

1.6 As Extruded (111)

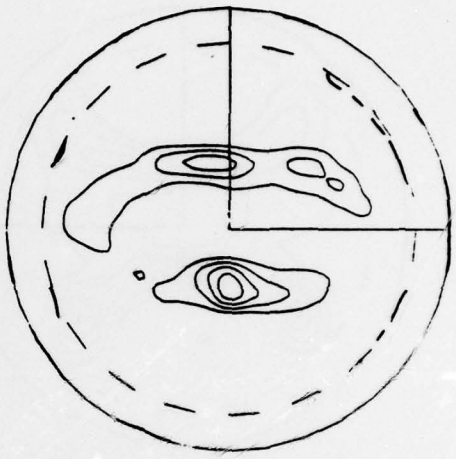

I/M Al-Li-Mn As Extruded
(111)

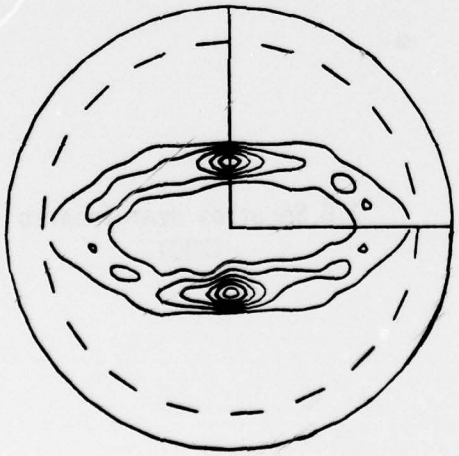

1.6 Solution Heat Treated
(111)

(a)

Figure 39. Pole figures of PM alloy 1.6 and IM Al-Li-Mn alloy in the as-extruded and solution-heat-treated conditions: (a) (111) planes, (b) (200) planes, and (c) (200) planes

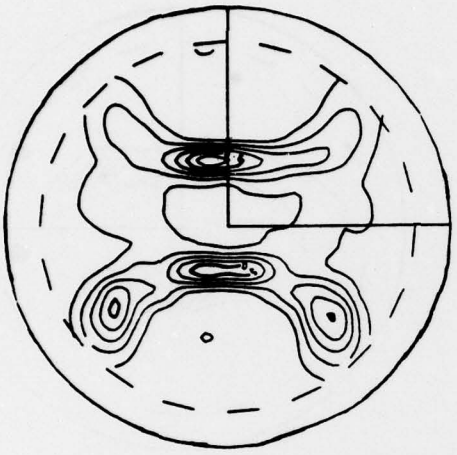

1.6 As Extruded (200)

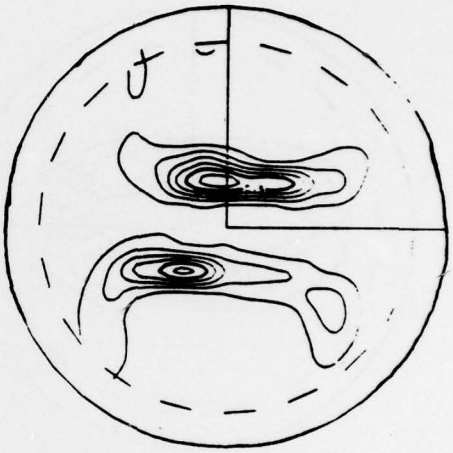

I/M Al-Li-Mn As Extruded (200)

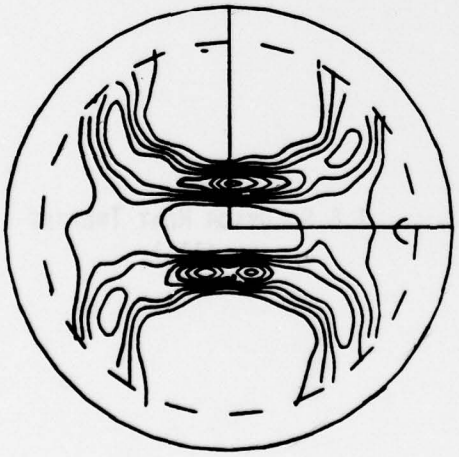

1.6 Solution Heat Treated (200)

(b)

Figure 39. (Cont.)

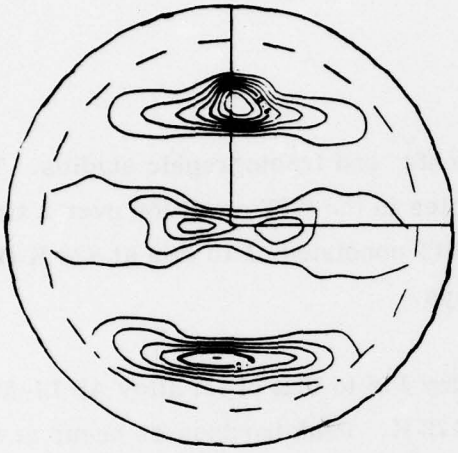

1.6 As Extruded (220)

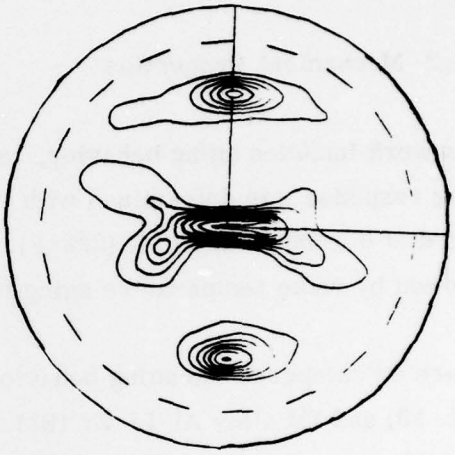

1/M Al-Li-Mn As Extruded
(220)

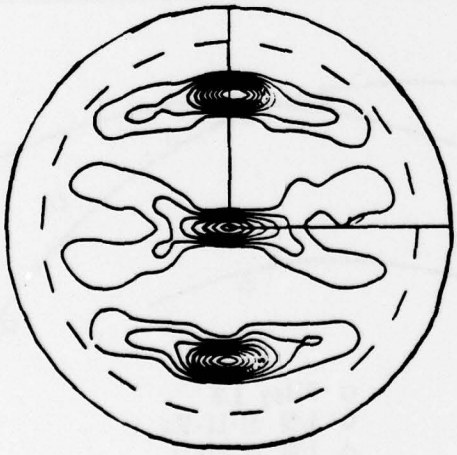

1.6 Solution Heat Treated
(220)

(c)

Figure 39. (Cont.)

Strain localization in such microstructure will not be inhibited by the small grain size and some other method for homogenizing slip – e.g., adding a large volume fraction of small dispersoids – must be used.

2.3.2 Mechanical Properties

This work includes aging behavior, tensile tests, and fractographic studies. The aging response was determined with 12 samples in the SHT condition over a time period of 0 to 350 h at 473 K (392° F). The SHT consisted of 15 min at 828 K (1031° F) followed by room temperature aging for 3 days.

Figure 40 compares the aging behavior of alloy 1.6 to that of IM alloy Al-Li-Mn (Ref. 13) and IM alloy Al-Li-Zr (Ref. 6) at 473 K. Peak hardnesses occur at 8, 24, and 15 h, respectively. The pronounced differences in time to reach peak hardness must be attributed to grain-size differences, as well as the disparity in grain boundary areas, residual cold work (because of different extrusion ratios), and enhanced diffusional mobility.

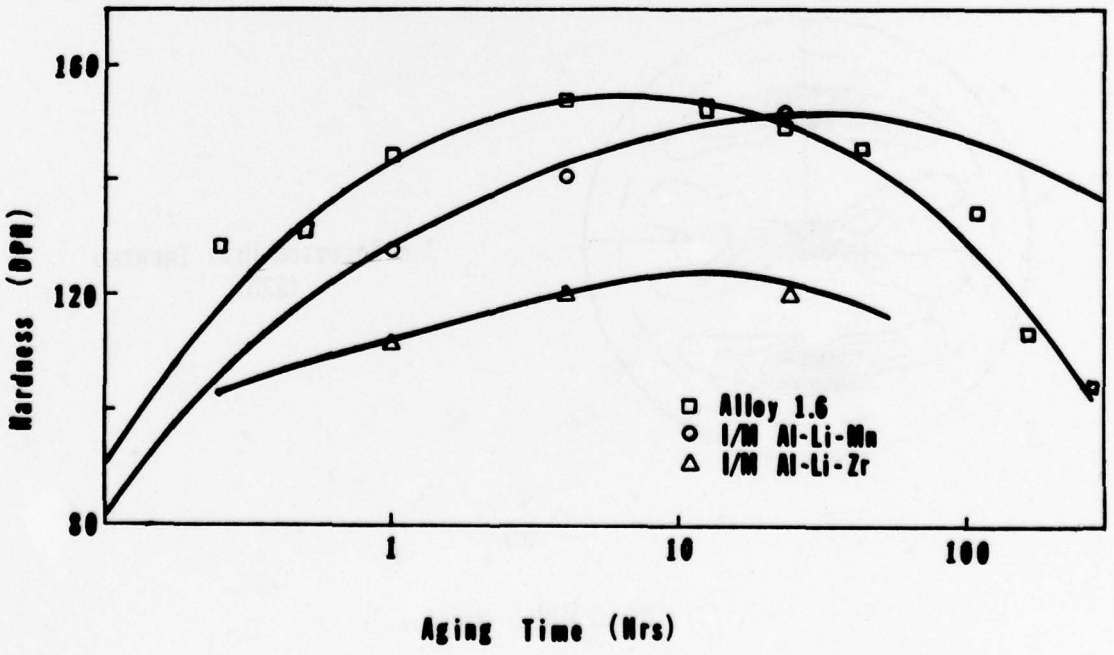

Figure 40. Hardness versus aging time at 473 K (392° F) for PM alloy 1.6 and IM Al-Li-Zr, both unrecrystallized and IM Al-Li-Mn recrystallized

Because of the limited amount of available material, tensile tests were attempted only on alloy 1.6. Two miniature tensile specimens were prepared in the underage (1 h at 473 K) and peak hardness (8 h at 473 K) conditions. The gage length was 10 mm long, and the gage diameter was 4.5 mm. The tests were run at room temperature at a strain rate of $0.1\ s^{-1}$.

Results for the peak-aged specimen are as follows:

$$\sigma_{ys} = 400\ \text{MPa (58 ksi)}$$
$$E = 83.4\ \text{GPa}\ (12.1 \times 10^3\ \text{ksi})$$
$$\text{Elongation} = 3.8\ \text{percent}$$

The underage specimen appeared to have a higher yield strength and lower elongation, but the validity of the test procedure for this specimen is in question. However, some useful information may be obtained from an examination of the fracture surface. These tensile tests will be repeated using larger specimens when more material is available.

Fracture surfaces of the two tensile specimens were examined by SEM. Typical fracture appearance is shown in Figs. 41, 42, and 43. Vertical facets were common in both aging conditions (Fig. 41). The height of these facets is somewhat smaller in the underage (1 h) condition than in the peak-age (8 h) condition. Secondary cracking, dimples, and particles on the fracture surface are also seen (Fig. 42). The jagged surface topography shown in Fig. 42 is typical of both aging conditions and may be due to separation occurring along original powder particle interfaces.

At higher magnification, the fracture surfaces appear quite faceted (Fig. 43). The somewhat continuous network of small polygonal-shaped areas may be attributed to contiguous dimple regions. Such dimple regions are about twice as large in the underage specimen as in the peak-age specimen. This difference in facet areas may be due to a difference in the density of particles large enough to provide void nucleation sites for the ductile, dimpled, fracture mode.

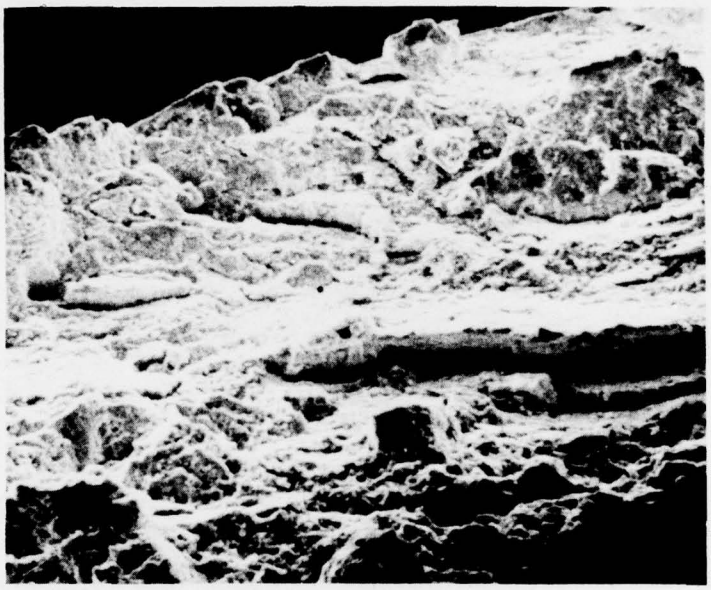

(a)

(b)

Figure 41. Secondary electron images of PM alloy 1.6 fracture surface: (a) under-age, 170× and (b) peak-age, 150×

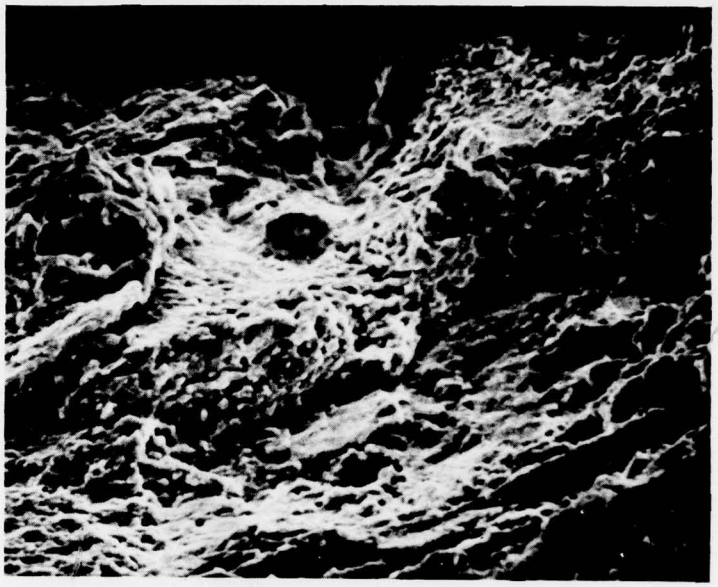

(a)

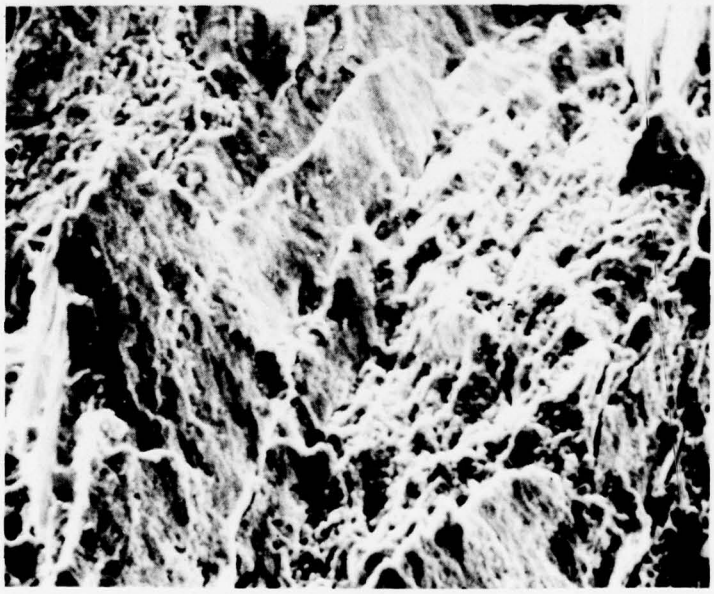

(b)

Figure 42. Secondary electron images of PM alloy 1.6 fracture surface: (a) under-age, 460× and (b) peak-age, 400×

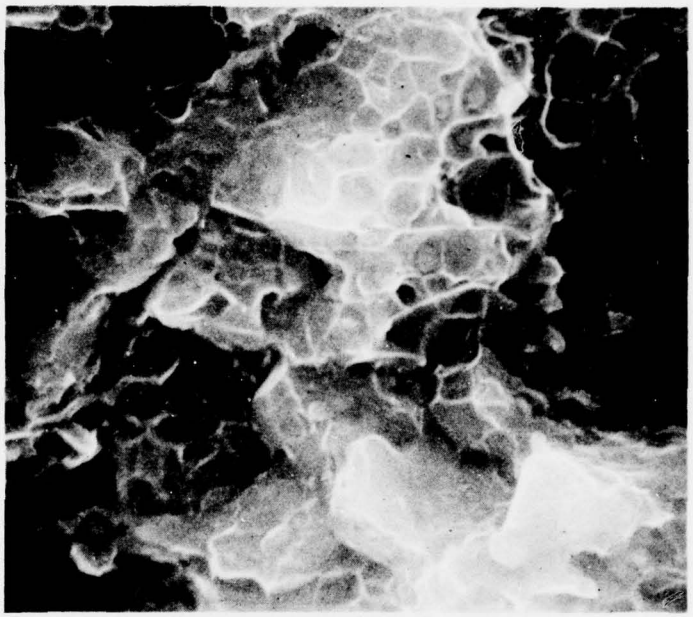

(a)

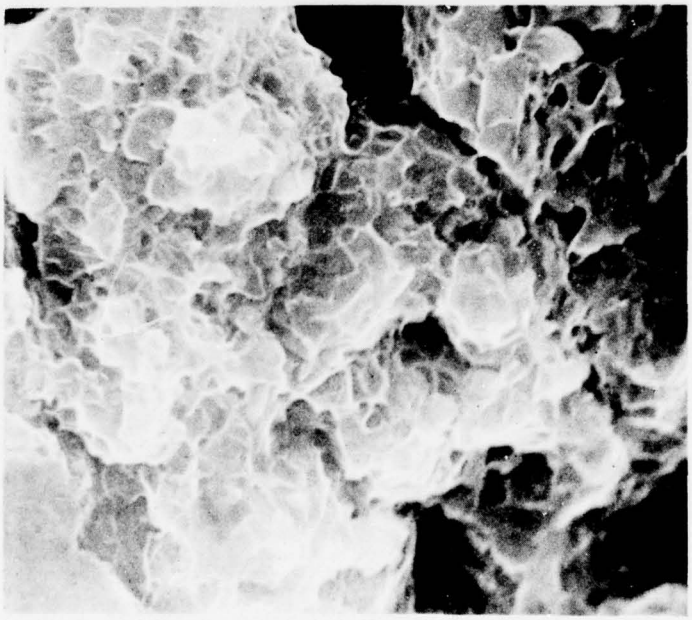

(b)

Figure 43. Secondary electron images of PM alloy 1.6 fracture surface: (a) under-age, 5000× and (b) peak-age, 5000×

2.3.3 AES and SEM Analysis of PM and IM Al-3Li-1.5Mn Fractures

To better understand the fracture characteristics of the IM and PM Al-Li-Mn alloys, an in situ Auger electron spectroscopy (AES) analysis of fracture surfaces was performed on the two alloys in peak-strength condition. This study was performed with a Model 590 scanning Auger electron microscope (SAM), at the Surface Sciences Division of Perkin Elmer Corporation. A fracture stage in the microscope permits in situ fracture and analysis within the microscope. The specimen is under constant ultra-low pressure of 17.3 nPa (1.3×10^{-10} torr). Auger spectra, scanning secondary electron images, and scanning Auger electron images were recorded at selected locations on the fracture surfaces. The Auger spectra were generated with a 5.0-kV beam incident on the fracture surface. A scanning electron microscope (SEM) examination was also conducted on the two alloys where a longitudinal surface was polished mechanically and etched for 1 min in a boiling 10%-bromine/90%-methanol solution.

Secondary electron images of the fracture surfaces of the IM and PM alloys obtained with the SAM are shown in Figs. 44 and 45. The macroscopic plane of the fracture of the IM alloy was normal to the extrusion direction. Microscopically, the fracture was intergranular with fine dimples on the grain boundary facets (regions 1 and 3, Fig. 44) and numerous flat featureless areas (region 2, Fig. 44). The macroscopic plane of fracture on the PM alloy was not perpendicular to the tensile axis, but deviated significantly (Fig. 45). The PM alloy fractured in a fibrous mode.

Auger electron spectra (AES) for the IM and PM alloys are given in Figs. 46 and 47 for locations indicated in Figs. 44 and 45, respectively. In the IM alloy, aluminum and oxygen were present on the fracture surface at each location; manganese was detected at only the featureless areas (Fig. 46). In the PM alloy, chlorine and potassium were both detected. The concentration of oxygen on the PM specimen fracture surface is significantly greater than on the IM alloy. This is exemplified by the high ratio of aluminum to oxygen AES peak heights in the PM alloy compared to the IM alloy.

An Auger electron microscope scan for manganese with the corresponding secondary electron image for the IM alloy is shown in Fig. 48. The featureless area examined

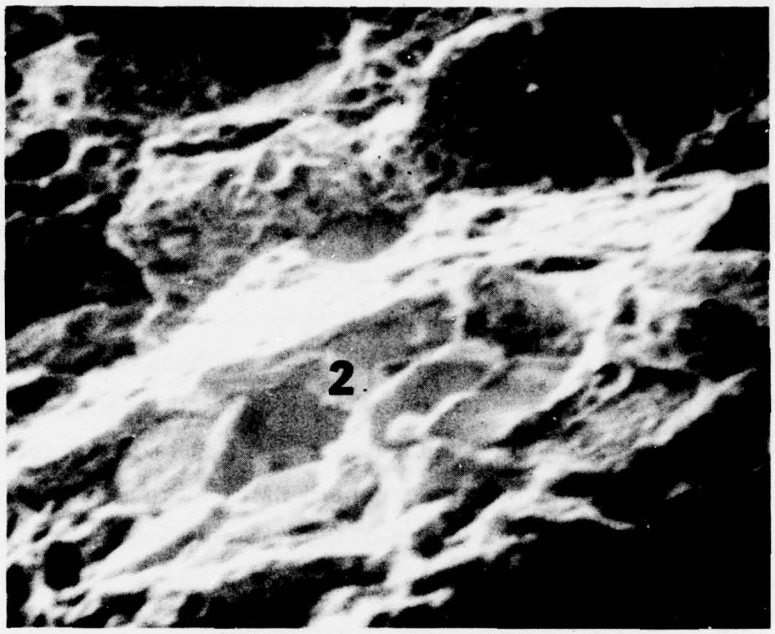

Figure 44. Secondary electron image of IM Al-Li-Mn alloy, showing selected areas for Auger analysis, 3200×

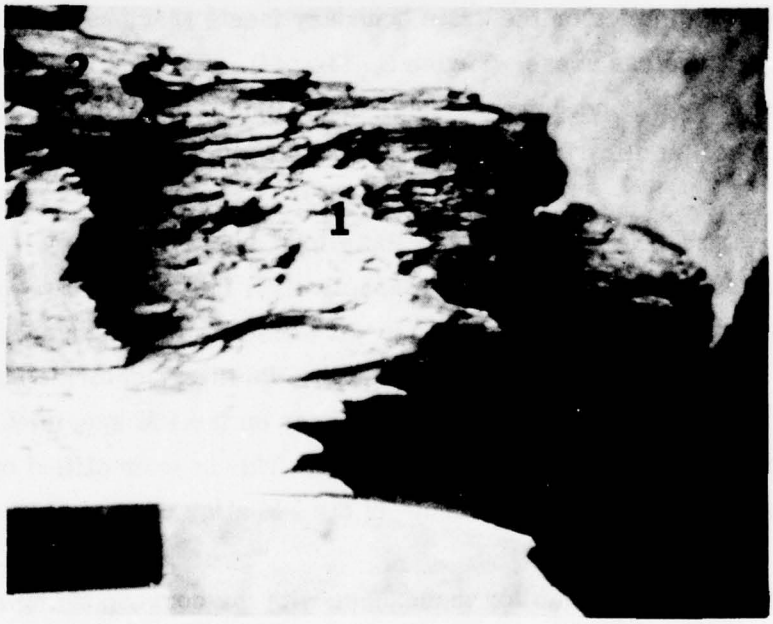

Figure 45. Secondary electron image of PM alloy 1.6, showing the area selected for Auger analysis, 20×

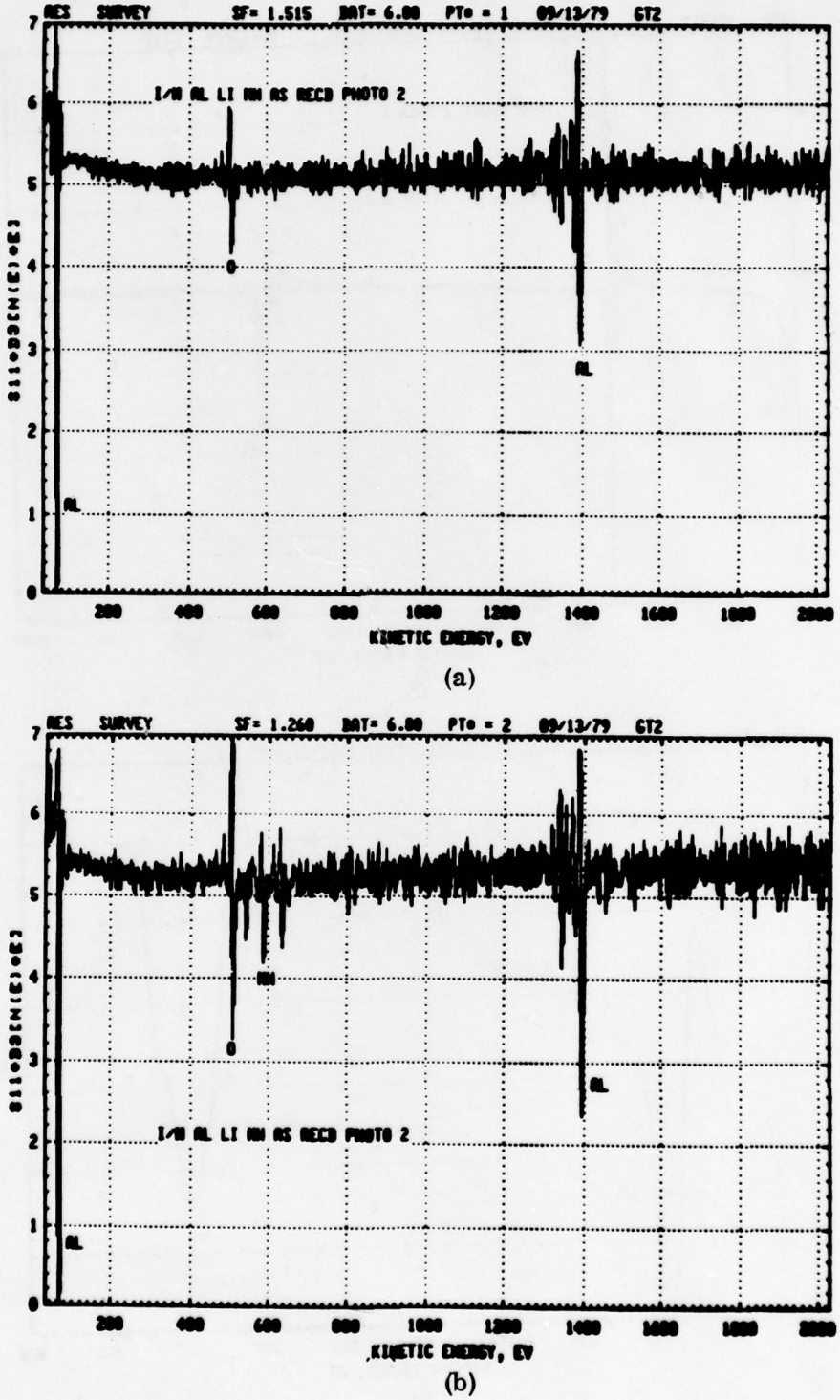

Figure 46. Representative Auger electron spectra for the IM Al-Li-Mn alloy: (a) general surface (region 1, Fig. 44) and (b) featureless area (region 2, Fig. 44)

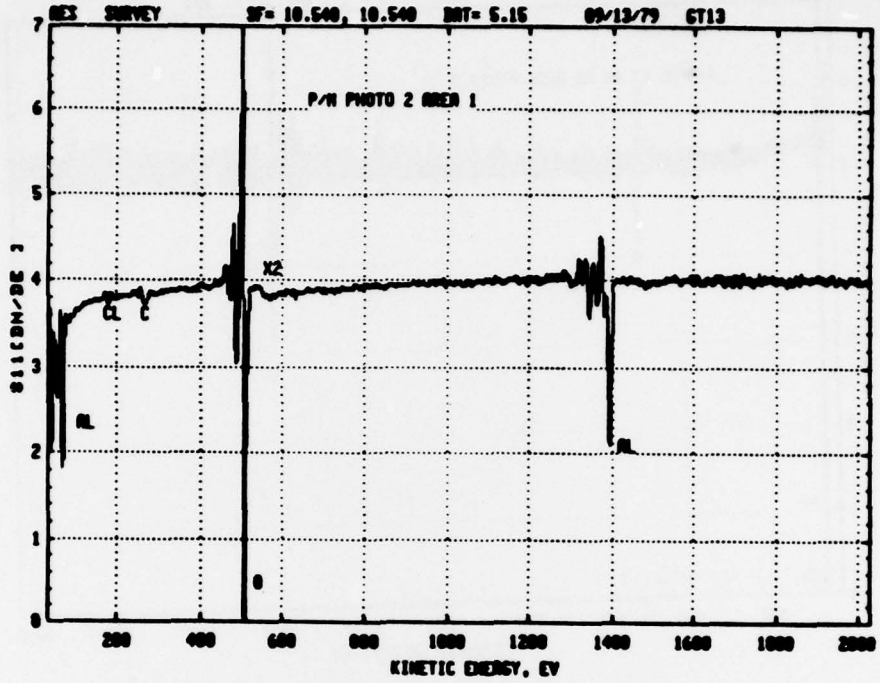

(a)

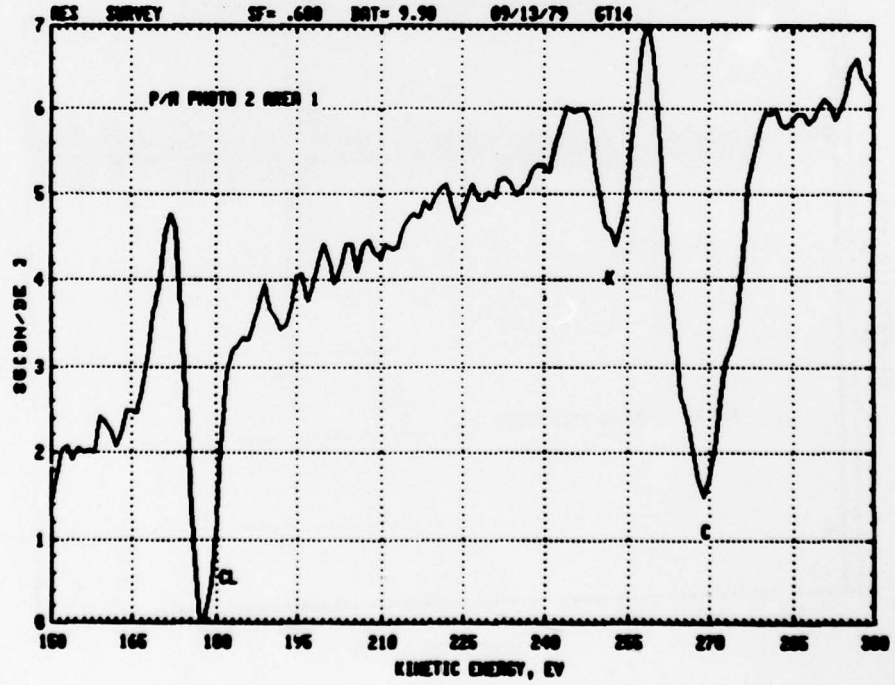

(b)

Figure 47. Representative Auger electron spectra for the PM alloy 1.6: (a) general surface and (b) expanded energy scale in the region of Cl, K, and C peaks

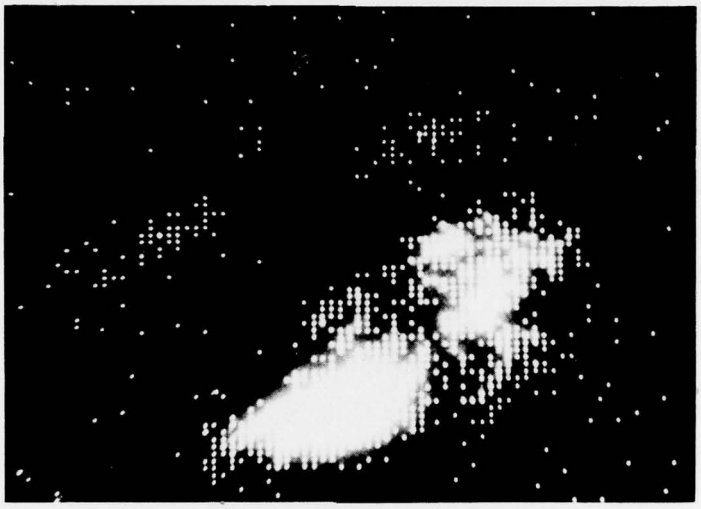

(a)

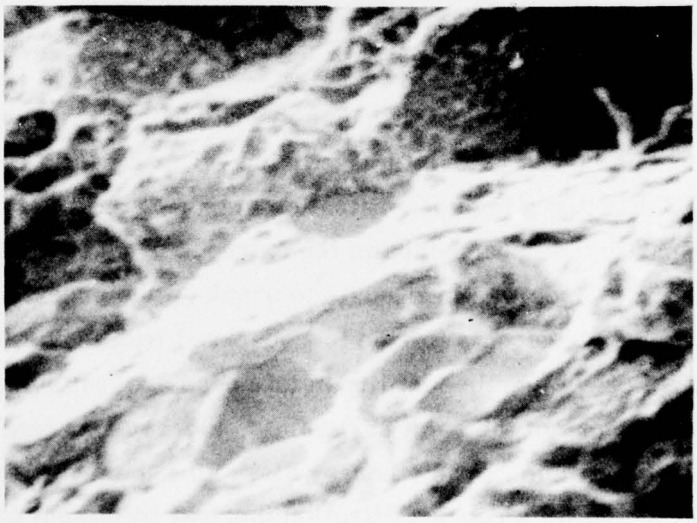

(b)

Figure 48. Auger analysis of the IM Al-Li-Mn alloy: (a) scanning Auger electron image for Mn and (b) corresponding secondary electron image, 3200×

is high in manganese and is probably a manganese-aluminum precipitate. Auger electron microscope scans of an area containing Cl and K in the PM alloy are shown in Fig. 49. The concentration of these elements on the fracture surface does not appear to be coincident.

Bromine-methanol etched surfaces of the IM and PM alloys have different distribution and morphology of second-phase particles. In the IM alloy (Fig. 50), there is a bimodal size distribution of precipitates. Chemical analysis by an energy dispersive analyzer on the SEM shows both the small and large particles contain manganese. In the PM alloy, in addition to the fine precipitates that contain manganese, there is a semicontinuous network of coarse particles (Fig. 51). Analysis of these particles indicates they are not manganese.

The AES and SEM result in some interesting observations. In the IM alloy, there is a bimodal size distribution of manganese precipitates. The coarse precipitates, which are approximately 10 μm in diameter, probably formed during solidification. The high volume fraction of these coarse precipitates is believed to contribute to the observed low fracture toughness of the IM alloy. The small precipitates apparently formed during the preheat cycle and are probably Al_6Mn.

The PM alloy appears to have a semicontinuous network of fine particles, corresponding to the splat particulate boundaries in the extrusion. These particles are probably a metal oxide, as AES detected a high concentration of oxygen on the fracture surface. Fracture along splat particulate boundaries in the extruded product probably occurred because the extrusion ratio used was inadequate to break up the preexisting oxide films. This fracture mode probably accounts for the low observed tensile ductility. Factors which would probably improve tensile ductility in this case are (a) improved oxidation protection during manufacture of the splat particulate, thereby reducing the oxide film thickness, (b) increased extrusion ratio, thereby disrupting the preexisting oxide films on particulate surfaces, and (c) a recrystallization thermal treatment to dissociate the oxide particle networks with the grain and subgrain boundaries.

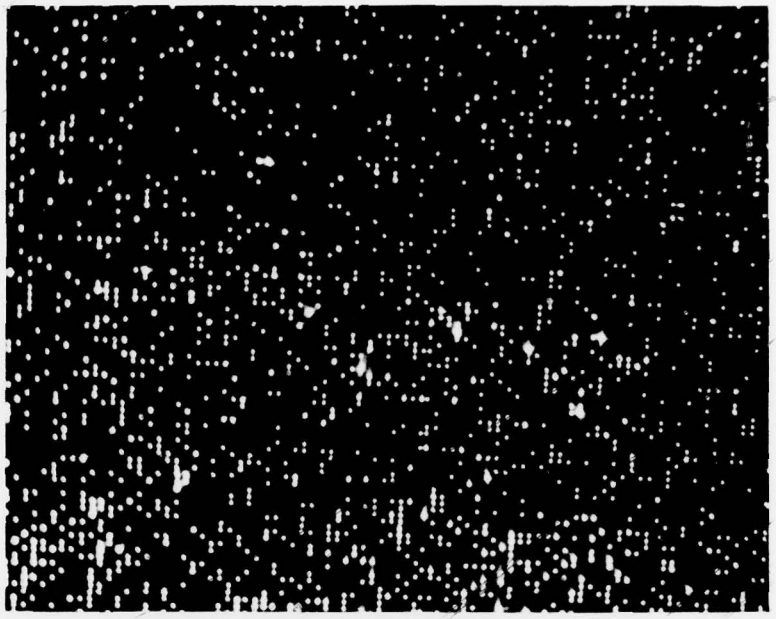

(a)

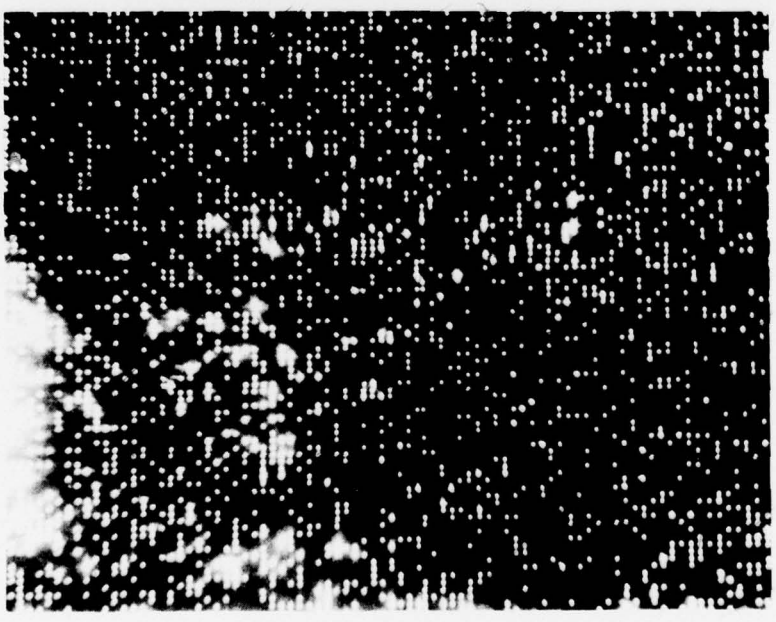

(b)

Figure 49. Auger analysis of PM alloy 1.6: (a) scanning Auger electron image for K, (b) scanning Auger electron image for Cl, and (c) corresponding secondary electron image, 500×

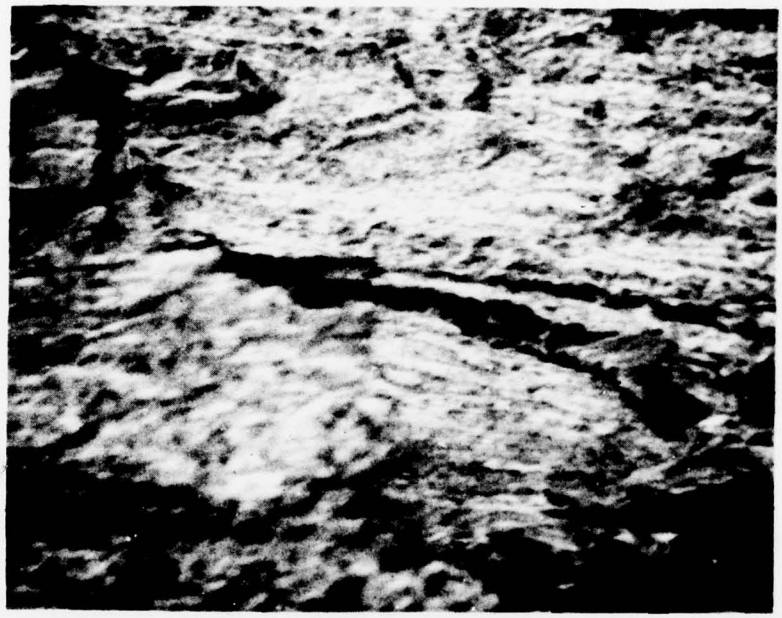

(c)

Figure 49. (Cont.)

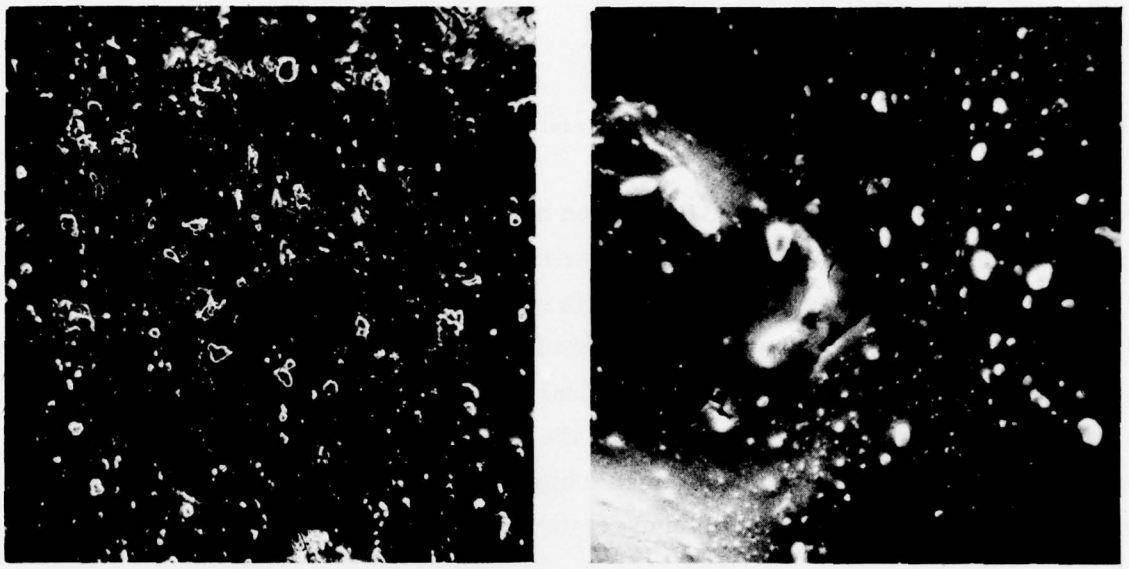

(a) (b)

Figure 50. Scanning electron micrographs showing the distribution of manganese precipitates in the IM Al-Li-Mn alloy: (a) 125× and (b) 610×. Etch: hot 10% bromine + 90% methanol

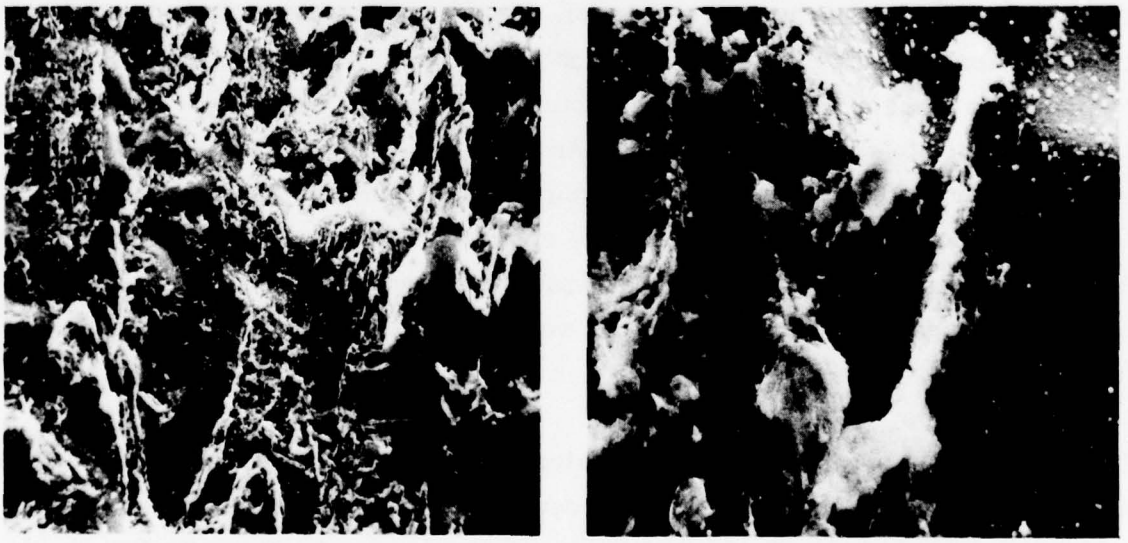

(a) (b)

Figure 51. Scanning electron micrographs showing the distribution of coarse particles and fine manganese precipitates in the PM alloy 1.6: (a) 115× and (b) 610×. Etch: hot 10% bromine + 90% methanol

2.4 TASK 4 – APPLICATION STUDIES

This task is being performed by the Lockheed-California Company.

During this period, the model for prediction of weight saving was adapted to an advanced tactical fighter (ATF) aircraft to permit assessment of effect on payoff and distribution of critical material properties. In addition, the effect of secondary structural criteria on payoff was evaluated. This is important since all structure is designed to resist a variety of alternate critical modes. Although one set of (primary) criteria will generally size the structure, the next most critical set described here as secondary criteria may limit the maximum payoff obtained from improvement of those properties that affect the primary criteria.

2.4.1 Adaption of Weight Savings Prediction Model to Fighter Aircraft

The model was extended to include an ATF by determining the distribution of structural weight by critical design criteria. The aircraft selected for analysis is from the Air Force "Wing/Fuselage Critical Component Development." An aluminum version of one of the ATF designs was selected (Ref. 16). Only the wing, tail, body, and strake are considered here since the landing gear, nacelle, and air-induction system are primarily steel or titanium. The structural components considered weigh 6273 kg, 81 percent of the total structural weight. An allocation of weight of individual components into the seven structural categories (Appendix C of Ref. 2) was then made by reviewing the loads and drawings available, combined with prior applicable experience. This weight breakdown is considered reasonably representative of a variety of ATF types, independent of configuration, gross weight, etc., for purposes of the present study.

The overall weight breakdown of the ATF aircraft selected is shown in Table 28. The weight breakdown of the structure into the seven categories for materials sensitivity analysis is shown in Table 29 along with comparative figures for the S-3A Patrol aircraft.

---

16. R. W. Walter, J. E. Mooney, R. A. Hamm, and R. R. June, "Wing/Fuselage Critical Component Development," Boeing Co. Technical Report AFFDL-TR-78-146, Contract AFFDL F38815-77-C-5228, Nov 1978

TABLE 28. ADVANCED TACTICAL FIGHTER WEIGHT ALLOCATION

Aircraft Components	Weight (kg)	Amount of Gross Weight (%)
Wing*	2,938	13.4
Horizontal Tail	0	–
Vertical Tail*	427	1.9
Body and Strake*	2,805	12.8
Landing Gear	935	4.3
Nacelle	170	0.8
Air Induction	475	2.2
Total Structure	7,750	35.4
Total Propulsion	3,671	16.8
Total Fixed Equipment	2,265	10.3
Weight Empty	13,681	62.5
Non-Exp. Useful Load	574	2.5
Operating Weight	14,234	65.0
Payload	2,345	10.7
Fuel	5,330	24.3
Gross Weight	21,909	100.0

*Aluminum components considered for weight savings analysis regarding advanced aluminum alloys.

TABLE 29. ALLOCATION OF WEIGHT BY FAILURE CRITERIA FOR ATF AND S-3A AIRCRAFT

Criteria Category	Criteria Description	Advanced Tactical Fighter						S-3A Patrol Plane (Wt %)
		Wing (kg)	Fuselage (kg)	Empennage (kg)	Control Surfaces (kg)	Total (kg)	Total (Wt %)	
1	Tensile Strength	499	544	54	68	1165	18.6	30.1
2	Compressive Strength	91	113	18	–	222	3.5	–
3	Crippling	499	544	45	136	1225	19.5	14.3
4	Compressive Surface	249	222	91	45	608	9.7	8.1
5	Buckling	408	567	45	113	1134	18.1	19.7
6	Aeroelastic Stiffness	249	272	68	136	726	11.6	14.1
7	Damage Tolerance or Fatigue Cutoff	499	544	104	45	1193	19.0	13.7
Total		2495	2808	426	544	6273		

*Weights are based on aluminum structure in wing, tail, body, and strake.

As shown in Table 30, the weight breakdown of both aircraft is similar in terms of percent weight affected by a strength or modulus change. The weight savings in the ATF is more dependent on DADTA (Category 7).

TABLE 30. PERCENT OF STRUCTURE AFFECTED BY SELECTED MATERIAL PROPERTIES

Property	Aluminum Structure Affected	
	S-3A	ATF
Strength	52.5	51.3
Modulus	56.2	58.9
DADTA	13.7	19.0

The effects of modulus and density on weight savings of aluminum structure in the S-3A patrol and ATF aircraft are shown in Figs. 52 and 53. The combinations of modulus and density satisfying contract goal A (30 percent increase in modulus-to-density ratio) are included in these figures. In Figs. 54 and 55 similar data are presented for strength, modulus, and density effects on weight savings for the same aircraft. Property combinations satisfying contract goal B (20 percent increase in both modulus-to-density and strength-to-density ratios) are included.

Some useful conclusions may be drawn from these data. Alloys meeting either contract goals A or B will result in weight savings varying from 3 to 14 percent, with the lowest density alloys giving the highest weight savings. The effect of density on weight savings is most pronounced for alloys that do not differ in strength from the baseline strength. The best combination of properties meeting either goal A or B results in about the same weight savings – 13 to 14 percent – for both types of aircraft. It is also clear that the highest payoff will be achieved for new alloys have a lower density than present commercial alloys. For alloys with higher density than present commercial alloys, weight savings will be less than 10 percent, with the highest savings achieved by a combination of strength and modulus improvement.

2.4.2 Minimum Required Properties

The minimum DADTA (fatigue life, fatigue crack growth resistance, and fracture toughness) properties required for compression critical structures, such as wing upper surfaces, were evaluated for various aircraft. The analysis indicates that tension and compression stresses in the wing upper surface can be increased by 22 percent for patrol aircraft, 29 percent for transport aircraft, and up to 23 percent for fighter aircraft with wing stores before fatigue life and fatigue crack growth properties become critical. The detailed analysis is presented in Appendix A.

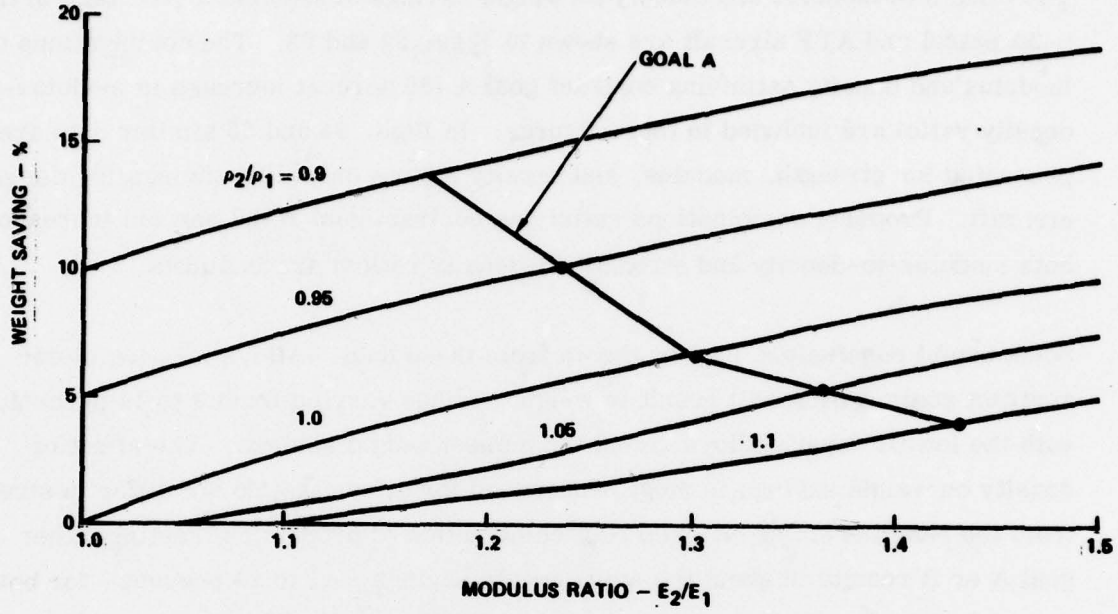

Figure 52. Effect of modulus and density on weight savings in the S-3A patrol aircraft

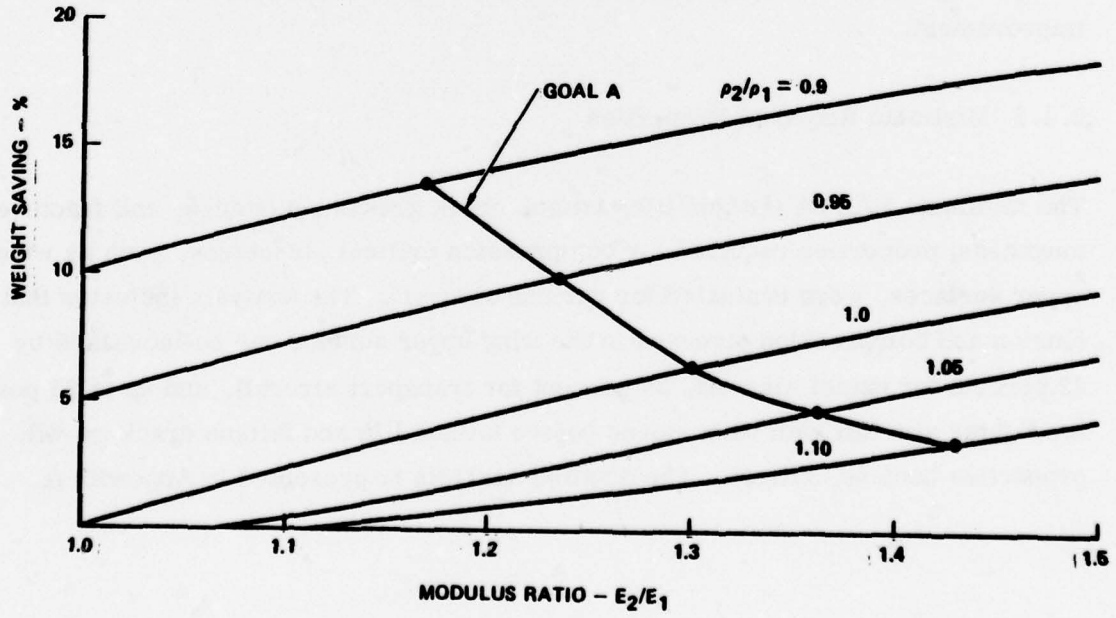

Figure 53. Effect of modulus and density on weight savings in an advanced tactical fighter

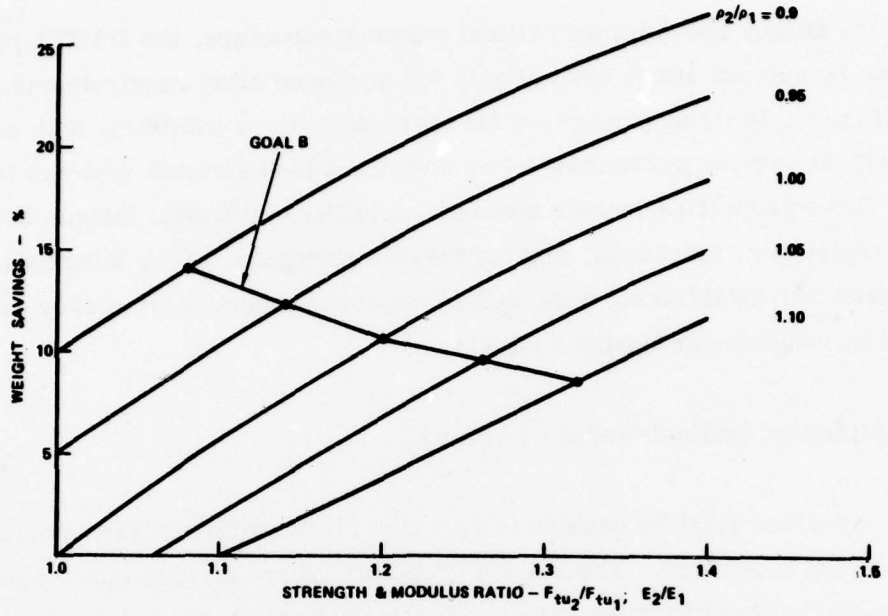

Figure 54. Effect of equal modulus and strength improvements at various densities on weight savings in the S-3A patrol aircraft

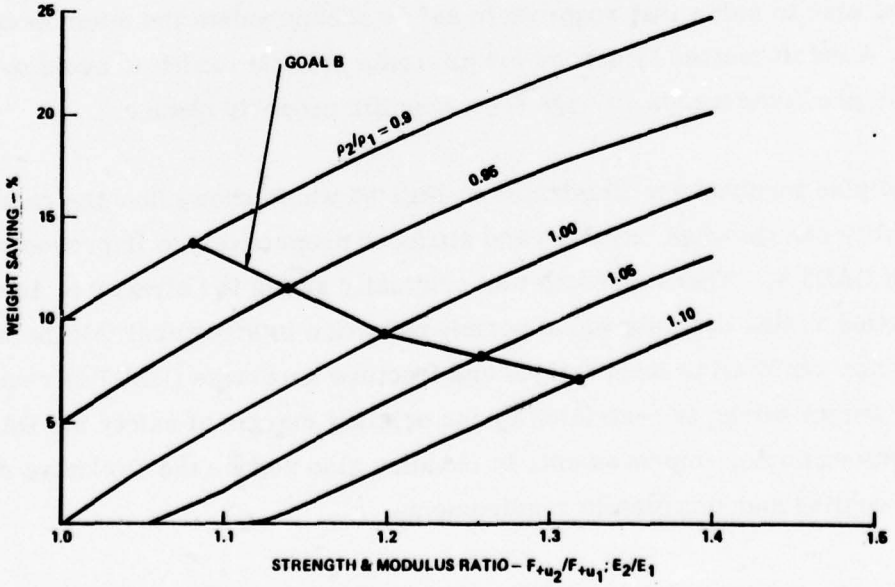

Figure 55. Effect of equal modulus and strength improvements on weight savings at various densities in an advanced tactical fighter

Except for fatigue and fracture critical primary structure, the DADTA properties exhibited by current alloys are suitable for advanced alloy requirements. A summary of the engineering properties for aluminum alloys exhibiting both satisfactory and marginal service performance in current and past aircraft systems is being compiled. These properties include strength, ductility, stiffness, fatigue life and crack growth resistance, toughness, and corrosion resistance. This information will provide a basis for establishing minimum acceptable properties when they are not dictated by conventional design analysis.

2.4.3 Alternate Critical Modes of Failure

A given structure must be capable of carrying all the different loading conditions imposed on it in service. These loading conditions are divided into the seven criteria categories used in the previously described "Weight Saving Prediction Model" (Ref. 2). Although only one of these categories usually establishes the structural cross section area for a given material, the relative importance of each category must be considered in the application of a new material. A large improvement in properties affecting the specific critical category, if fully used, could reduce the structural size to below that required to safely accommodate the other modes of loading. A cutoff method is needed for alternate critical modes to avoid overly optimistic predicted weight savings for a specific property change.

The principles involved are illustrated in Fig. 56 which shows how the relative levels of criticality change when strength and stiffness properties are improved without change in DADTA. Where strength was originally sizing the structure, improvement in properties in this example would permit reduction in structural thickness to below the minimum required to meet fatigue and fracture toughness (DADTA) requirements. Thus the weight saving is restricted by the original margin of safety for DADTA. In the same example, improvements in modulus also reduce the thickness required to meet buckling and aeroelastic requirements.

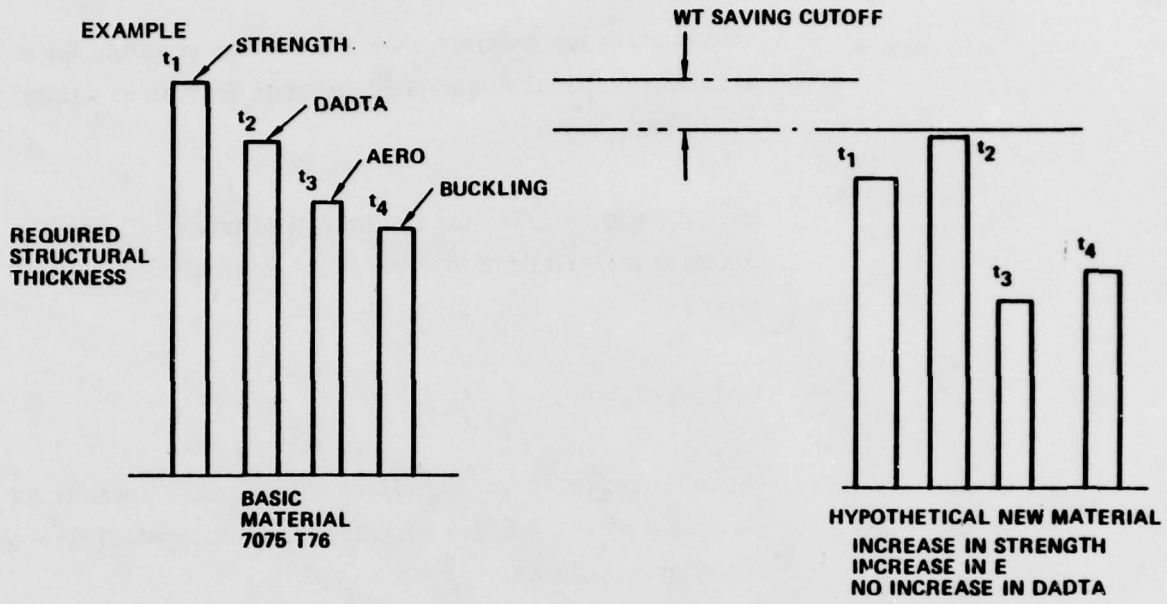

Figure 56. Example of weight savings cutoff when a new alloy having increased strength and modulus replaces the basic alloy. Allowable stress for the DADTA failure criterion is assumed to be unchanged

The maximum possible weight saving from improvement in material properties for structure that is critical in one category is established by two factors: (1) the change in margin of safety of any of the other critical categories and (2) the increase in allowable stress of any of the other second critical categories resulting from the material improvement.

This cutoff on weight saving may be calculated using the following equation.

$$R_{a/b\,max} = R_b \left(\frac{I}{I + MS}\right)^n$$

where

$R_{a/b\ max}$ = weight ratio for maximum weight savings possible for a structure critical in category "a" with margin of safety MS in category b

R_b = weight ratio W_2/W_1 for the improved material over the baseline material for the next most critical category (see Table C-1, Ref. 2)

MS = margin of safety

n = exponent dependent on the effect of material thickness on allowable stress (values vary according to critical failure category as follows)

n = 1 for categories 1, 2, 4, 6, 7
n = 1/2 for category 3 (crippling)
n = 1/3 for category 5 (buckling)

For example, the maximum weight savings possible from use of a new alloy with higher modulus where the structure is sized by aeroelastic requirements, category 6, and has a 20 percent margin of safety (MS) in buckling, category 5, would be determined as follows:

For category 5, (buckling):

MS = 0.20
n = 1/3

And from the cutoff equation,

$$R_{6/5}\Big|_{max} = R_5 \left(\frac{1}{1 + MS}\right)^{1/3}$$

From Table C-1, Ref. 2,

$$R_5 = \frac{\delta_2}{\delta_1}\left(\frac{E_1}{E_2}\right)^{1/3}$$

Then,

$$R_{6/5}\Big|_{max} = \frac{\delta_2}{\delta_1}\left(\frac{E_1}{E_2}\right)^{1/3} \frac{1}{1.2}^{1/3}$$

The maximum weight savings fraction is:

$$\frac{\Delta W}{W_1}\Big|_{max} = 1 - R_{6/5\ max} = 1 - \frac{\delta_2}{\delta_1}\left(\frac{E_1}{1.2E_2}\right)^{1/3}$$

$$\frac{\Delta W}{W_1}\Big|_{max} = 1 - \left(\frac{E_1}{1.2E_2}\right)^{1/3}$$

Using this equation, the limitations imposed by a 20 percent margin of safety in buckling on potential weight savings from improvement in modulus were calculated and compared to weight savings possible for a structure sized by aeroelastic requirements (Fig. 57). The weight savings resulting from modulus improvement only are first plotted for each affected category as a percent of the structural weight involved. The maximum payoff from modulus improvement is in aeroelastic critical structures, category 6. When the limitation of buckling margin of safety is imposed, the weight saved is reduced to a minimum indicated in Fig. 57 as the lower bound of the shaded region. Because of varying degrees of structural criticality it is anticipated that the actual weight saving would be somewhere between maximum and minimum payoff.

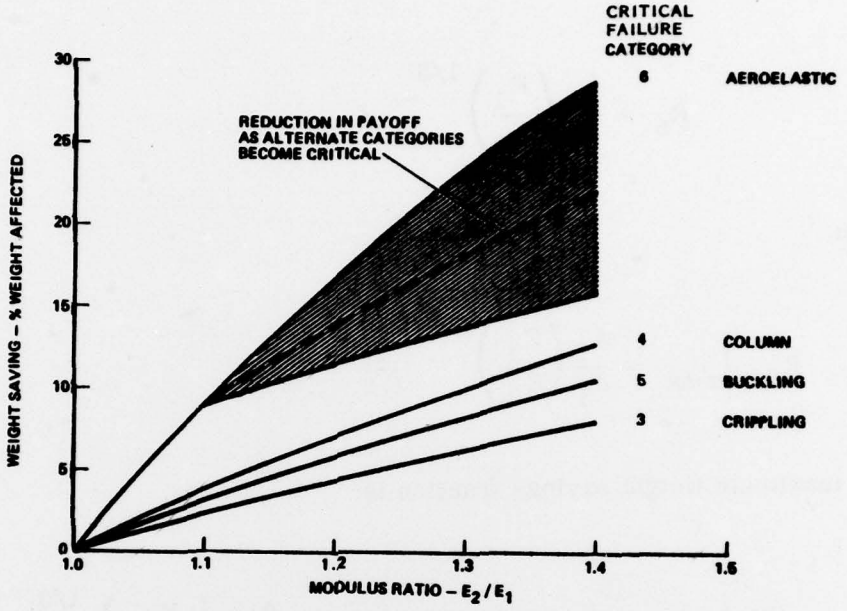

Figure 57. Effect of modulus improvement on weight saving achieved in structures sized by various critical failure categories

2.4.4 Baseline Properties

The baseline properties for 7075-T76 to be used for comparison purposes are presented in Table 31.

TABLE 31. 7075-T76 EXTRUSION BASELINE PROPERTIES

Property	Test Dir.	Minimum[a]	Typical
Tensile Ultimate, F_{tu}, MPa (ksi)	L	517 (76)	522 (80)
Tensile Yield, F_{ty}, MPa (ksi)	L	448 (65)	483 (70
Compression Yield, F_{cy}, MPa (ksi)	L	448 (65)	483 (70)
Shear Ultimate, F_{su}, MPa (ksi)	L	283 (41)	303 (44)
Elongation, % in 4D	L	7	10
Tensile Modulus, GPa (10^3 ksi)	L	72 (10.4)	–
Compression Modulus, GPa (10^3 ksi)	L	74 (10.7)	–
Shear Modulus, GPa (10^3 ksi)	L	28 (4.0)	–
Poissons Ratio, μ	–	0.33	–
Density, kgm^{-3} (lb in.$^{-3}$)		2796 (0.101)	–
Fatigue, F_{max}, MPa (ksi) (Net)			
For $K_t = 2.7$, $R = 0.1$, $n = 10^5$	L	–	152 (22)
Plain Strain Fracture Toughness,	LT	–	33 (30)
K_{1c}, MPam$^{1/2}$ (ksi $\sqrt{in.}$)	TL	–	27 (25)
Fatigue Crack Growth, ΔK, MPam$^{1/2}$ (ksi $\sqrt{in.}$)			
For $R = 0.1$, $da/dn = 10^{-5}$ in/cycle, Lab Air	LT	–	11 (10)
Stress Corrosion Threshold, MPam$^{1/2}$ (ksi $\sqrt{in.}$)	ST	27 (25)[b]	–
Exfoliation Corrosion Resistance		>B[b]	–

(a) "A" values from MIL-Handbook-5 unless otherwise specified.
(b) Specification values, exfoliation corrosion per EXCO.

Section 3
CONCLUSIONS

1. Melting and atomization to produce splat or fine atomized powder was readily achieved for 15 of the first 16 alloys, both with and without lithium. One alloy, Al-3Li-1Zr, posed significant difficulties because of the high chemical activity in the liquid state and incomplete solubility of Zr at practical melt temperatures.

2. From metallographic examination of the alloy splats, rapid cooling rates from 10^6 to over 10^7 Ks^{-1} appear to have been achieved. In the Al-Fe-Ni-Co, Al-Mn, and Al-Mn-Si alloys, a number of unique solidification features and phases have been produced by the nonequilibrium solidification conditions.

3. Examination of particulate in the splat lots reveals the presence of two types of nonsplat particles that have not solidified as rapidly as the splat and probably should be removed before subsequent consolidation is performed. The first type is found primarily in the coarsest screen fractions and has a very thick oxide surface layer and relatively coarse microstructure. The second type is found primarily in the fine screen fractions and has a thicker oxide film and coarser microstructure than the splat. Most of these particles can be removed by rejecting +8 and -100 or -200 size screen fractions.

4. The first eight Al-Li alloys prepared from unscreened splat and in the extruded and peak-aged condition exhibit a tensile modulus-to-density ratio 26 to 39 percent higher than 7075-T6, as was expected. The longitudinal tensile yield and ultimate strengths are between 82 and 103 percent of 7075-T6 typical values, except the Al-3Li-0.5 Fe-0.5 Co alloy which on the same basis exhibited 68 percent yield and 77 percent ultimate strength.

Tensile elongation was 2.7 to 5.7 percent, where the minimum goal is 7 percent. For these alloys, four steps have been identified for evaluation to improve the properties, especially tensile ductility.

- Removal of majority of nonsplat particles by screening
- Higher hot pressing temperatures and pressures
- Higher extrusion ratios
- Underaging and overaging heat treatments

5. Cold compaction of the lithium-containing splat and the nonlithium-containing fine atomized powder alloys is readily achieved. The nonlithium-containing alloys in splat form do not cold compact by wet-bag isostatic techniques but can be satisfactorily compacted in a steel die using a bottom knockout.

6. Development of a random texture in Al-Li PM splat alloy extrusions is not likely to be achieved, as sharp, well-defined crystallographic textures were found in two alloys extruded at only an 8:1 reduction ratio. These textures are comparable to those developed in an IM alloy extrusion of similar composition, extruded at a 35:1 reduction ratio.

7. An extrusion ratio of 8:1 for the lithium-containing splat alloys may be inadequate to obtain optimum interparticle bonding, and higher extrusion ratios may be required to disrupt the oxide particle networks corresponding to splat particulate interfaces.

8. The relationship between weight savings and change in strength, stiffness, fatigue, or toughness properties for an advanced tactical fighter was found to be similar to that previously derived for a patrol aircraft. For either type aircraft, an optimum combination of properties meeting either contract goal A or B will result in a weight savings of approximately 14 percent.

Appendix A

MINIMUM PROPERTY REQUIREMENTS FOR HIGHLY COMPRESSION LOADED STRUCTURES

A.1 INTRODUCTION

Certain parts of an aircraft structure, such as the wing upper surface, are loaded primarily in compression. For these structures, application of new aluminum alloys having higher specific stiffness will be considered to achieve significant weight savings. These alloys must also exhibit acceptable fatigue and fracture toughness properties to not compromise the intended weight savings. In this appendix, the minimum required fatigue strength (S-N), fatigue crack growth (da/dN versus ΔK), and fracture toughness (K_{Ic}) requirements are derived which are to be applied in alloy development as "secondary property" goals for such structures.

A.2 FATIGUE STRESS VERSUS CYCLIC LIFE

Evaluation of fatigue strength requirements in aircraft structures containing notches or holes is facilitated by use of an effective stress $\bar{\sigma}$ defined as follows:

$$\bar{\sigma} = \sigma_{max} (1 - R)^m = K_f S_{max} (1 - R)^m \qquad (A.1)$$

where

σ_{max} = maximum local stress at the edge of a notch

R = stress ratio; minimum stress divided by maximum stress

K_f = fatigue stress concentration factor

S_{max} = maximum gross area tensile stress

m = material constant = 0.425 for 7075-T6 aluminum (Ref. A-1)

A-1 J. C. Ekvall, T. R. Brussat, and S. T. Chui, "Summary of 1978 Independent Research on Fracture Mechanics, Fatigue, and Risk Analysis Methods," Lockheed-California Company Report, LR 28959 (to be published).

A large amount of S-N data for 7075-T6 aluminum sheet has been analyzed and expressed in terms of an effective stress versus cycles to failure (Ref. A-1). For specimens with notch radii from 0.090 to 0.158 in., the best fit equation for effective stress is as follows:

$$\log \bar{\sigma} = C - 0.165 \log N \qquad (\text{for } 5236 < N < 212,667) \qquad (A.2)$$

where

N = cycles to failure

C = 3.435 (for $\bar{\sigma}$ in MPa; = 2.596 for $\bar{\sigma}$ in ksi)

In the present derivation the properties of 7075-T6 are used as a baseline.

The most significant loading cycle affecting the fatigue life of aircraft structure is the ground-air-ground (GAG) cycle incurred once each flight. The average fatigue stresses during a GAG loading cycle on the wing upper surface of some aircraft types is given in Table A-1.

TABLE A-1. TYPICAL APPLIED STRESSES IN AIRCRAFT WING UPPER SURFACE DUE TO GAG CYCLES

Type of Aircraft	GAG Cycles in a Lifetime	Gross Area Stress				
		Maximum		Minimum		
		(MPa)	(ksi)	(MPa)	(ksi)	R
Fighter	10,000	41.4	6	-124	-18	-3.0
Patrol	20,000	67.6	9.8	-82.7	-12	-1.2
Transport	60,000	51.7	7.5	-82.7	-12	-1.6

It is assumed here that the effective stress given by Eq. (A.2) pertains to both the upper and lower surfaces of the wing. Starting with the GAG lifetime cycles (Table A-1), this is divided by the fraction of estimated fatigue damage* due to GAG cycles to

*Damage due to GAG cycles cited herein is from fatigue analyses of each type aircraft and is a reasonable estimate over service life.

obtain an equivalent number of GAG cycles. The allowable effective stress is calculated from this equivalent number of GAG cycles using Eq. (A.2). Using an R value typical of each type aircraft, and K_f assumed to be 4.35,* the allowable GAG maximum gross area stress is calculated from Eq. (A.1). These data are presented in Table A-2, where they are compared with the GAG cycle maximum applied tensile stress.

TABLE A-2. SUMMARY OF CALCULATED ALLOWABLE STRESSES FOR WING UPPER SURFACE STRUCTURE

Type of Aircraft	Estimated Damage Due to GAG Cycle (Fraction)	Equivalent Number of GAG Cycles	Allowable Effective Stress (MPa)	Allowable Effective Stress (ksi)	R	Allowable GAG Tensile Stress[a] (MPa)	Allowable GAG Tensile Stress[a] (ksi)	Applied GAG Tensile Stress (MPa)	Applied GAG Tensile Stress (ksi)	Increase to Equal LWR Wing Surface Allowable Stress (%)
Fighter										
Without Stores	0.30	33,330	488	70.8	-3.0	62	9.0	41	6.0	50
With Stores								55	8.0[b]	23[b]
Patrol	0.70	28,570	500	72.5	-1.2	82	11.9	68	9.8	21
Transport	0.90	66,670	435	63.1	-1.6	67	9.7	52	7.5	29

(a) Assuming $K_f = 4.35$.
(b) Assuming Wing Steres, see text.

*The value assumed is based on past service experience. For example, the Electra aircraft exhibits a K_f of about 4.3.

As seen in Table A-2, the wing upper surfaces of fighter aircraft are not fatigue critical; the fatigue stress could be increased by 50 percent when using the baseline 7075-T6 aluminum alloy. If the fighter performs most of its missions with wing stores,* the applied maximum tensile stress in a GAG cycle may be 8.0 ksi, typically, because of increased stress during taxiing. In this case, the wing upper surface applied stress could be increased only 23 percent before its fatigue life would reach the limit established by the wing lower surface maximum allowable stress. In such case, the margin between applied and allowable maximum tensile stress in the wing upper surface of the fighter is equivalent to the patrol and transport aircraft margins.

The requirement for screening minimum acceptable fatigue behavior of advanced aluminum alloys presently being developed is addressed in the following paragraphs.

Morrow and Johnson (Ref. A-2) have found that a large number of currently available aluminum alloys exhibit at least 10,000 cycles to failure when subjected to an alternating strain of ± 0.005. This is equivalent to an alternating stress of ± 362 to 414 MPa (52.5 to 60 ksi), assuming linear elastic behavior and a modulus of elasticity from 72.4 to 82.7 GPa (10.5 to 12×10^6 psi). If this alternating stress is assumed to be the maximum local stress σ_{max} at the edge of a notch then, from Eq. (A.1), the equivalent effective stress $\bar{\sigma}$ is 486 to 555 MPa (70.5 to 80.5 ksi), for R = -1.0 and m = 0.425.

This is 7 to 18 percent lower than the effective stress calculated from Eq. (A.2) for 10,000 cycles to failure. Thus, the fatigue (S-N) behavior of the developmental alloys does not have to be any better than those evaluated by Morrow and Johnson when considering structural applications such as the wing upper surface of aircraft. For preliminary screening of developmental alloys, S-N type fatigue testing is not required.

---

*Bombs, rockets, fuel tanks, etc., supported on the wing structure.

A-2 Jo Dean Morrow and T. A. Johnson, "Correlation Between Cyclic Strain Range and Low Cycle Fatigue Life of Metals," Mater. Res. and Stds., Vol. 5, No. 1, 1965, p. 30.

A.3 FATIGUE CRACK GROWTH

Fatigue crack growth rate between 2.5×10^{-8} and 2.5×10^{-6} m/cycle for aluminum alloys is reasonably approximated by the following equation.

$$\frac{da}{dN} = C' (\overline{\Delta K})^4 \qquad (A.3)$$

In the following, fatigue crack growth in the wing upper and lower surfaces will be related. An effective stress intensity range $\overline{\Delta K}$ is used, which is defined as follows:

$$\overline{\Delta K} = K_{max} (1 - \hat{R})^m = S_{max} \alpha (1 - \hat{R})^m \qquad (A.4)$$

where

K_{max} = stress intensity corresponding to the maximum stress S_{max} of the loading cycle

α = factor to account for crack geometry and crack length

$\hat{R}$ = maximum R, or -0.12, where R is the minimum to maximum stress ratio (Ref. A-3)

m = material constant = 0.425 for 7075-T6 aluminum (Ref. A-4)

For a given material the fatigue crack growth rate for the wing upper surface and wing lower surface are related to the maximum tension stress for the same crack length and crack geometry. In tension-compression stress cycles, the compressive stress component has a minor contribution to crack growth rate compared to an equivalent

---

A-3 T. R. Brussat, "An Approach to Predicting the Growth to Failure of Fatigue Cracks Subjected to Arbitrary Uniaxial Cyclic Loading," ASTM STP 486, May 1971, p. 122

A-4 E. K. Walker, "The Effect of Stress Ratio During Crack Propagation and Fatigue for 2024-T3 and 7075-T6 Aluminum," ASTM STP 462, 1970, p. 1

tensile stress component. For the ground-air-ground stress cycle, an equivalent value of $\hat{R}$ of -0.12 may be used. For both upper and lower wing surfaces (Ref. A-3), and from Eq. (A.2), the stress intensity is directly proportional to the maximum tensile stress. Considering only the GAG cycles given in Table A-1, the wing upper surface stresses would have to be increased to produce equal fatigue growth rates in the wing upper and lower surfaces (Table A-3).

TABLE A-3. STRESS INCREASE IN WING UPPER SURFACE REQUIRED FOR EQUIVALENT CRACK GROWTH RATE IN BOTH UPPER AND LOWER SURFACES OF THE WING

Type of Aircraft	Maximum Tensile Stress of GAG Cycle				Increase in Upper Wing Stress for Equivalent Fatigue Crack Growth Rates (%)
	Wing Lower Surface		Wing Upper Surface		
	(MPa)	(ksi)	(MPa)	(ksi)	
Fighter	124	18	41	6	300
Patrol	83	12	68	9.8	22
Transport	83	12	52	7.5	60

In the fighter or transport type aircraft, the increase in wing upper stress required for equivalent fatigue crack growth rates in both upper and lower surfaces is higher than for equivalent fatigue stress versus cycles to failure, 300 versus 50 percent, respectively. The percent increase in wing upper surface tensile stress for fatigue crack growth and fatigue stress versus cycles to failure is about the same for the patrol aircraft. Therefore, for initial evaluation of developmental alloys, for highly compression-loaded aircraft structural applications, fatigue crack growth tests are not required.

A.4 FRACTURE TOUGHNESS

The fracture toughness parameters of interest for assessing the residual strength of a structure are the plane strain (K_{Ic}) and plane stress (K_c) stress intensity factors.

The relation between K_{Ic} and the ultimate design stress applicable to aircraft structures is presented below.

In current aircraft design there is no standard requirement regarding the plane strain fracture toughness index of a material. However, some minimum value of K_{Ic} is desired so that the fracture strength of the structure will not be compromised because of the presence of normal manufacturing defects or material flaws. K_{Ic} of the material is particularly important for certain structural components, including stiffeners, spar caps, and rib truss members. In the present case, it is assumed that a 0.127 cm (0.05 in.) long crack in these members will not cause failure at the design ultimate load. This size crack is near the nondestructive inspection detection threshold and is to be assumed according to MIL-A-83444 unless one can demonstrate that a smaller crack size will be detected with the same high reliability.

The formula for stress intensity of a crack at a fastener hole is given by the following equation

$$K_I = S\sqrt{\pi a}\ \ f\ [a/(r_o + a)] \qquad (A.5)$$

where:

K_I = applied stress intensity, MPa $m^{1/2}$ (or ksi $\sqrt{in.}$)

$f\ [a/(r_o + a)]$ = 1.05 for a 0.127 cm (0.050 in.) long crack at the edge of a 0.476 cm (3/16 in.) diameter hole

a = crack length, assumed 0.127 cm (0.05 in.)

S = gross area stress in vicinity of the crack, MPa or ksi

Substituting these values in Eq. (A.5) yields the following

K_I = 0.663 S (SI units), or = 0.416 S (English units)

For members sized by allowable tensile stress, the gross area stress is approximately 75 percent of the material ultimate strength (F_{tu}). The corresponding plane strain fracture toughness index is given by the following equation:

$$K_I = 0.5\ F_{tu}\ \text{(SI units) or } = 0.31\ F_{tu}\ \text{(English Units)} \qquad \text{(A.6)}$$

For an aluminum alloy with an ultimate strength of 552 MPa (80 ksi), the stress intensity factor K_I is 27.5 MPa $m^{1/2}$ (25 ksi $\sqrt{in.}$), and defines the minimum required K_{Ic}. This is approximately the value of K_{Ic} in the L-T direction for aluminum alloys commonly used in aircraft structures. Somewhat lower values may be tolerated in the other grain directions.

A.5 SUMMARY

The minimum required fatigue strength (S-N), fatigue crack growth (da/dN versus ΔK), and fracture toughness (K_{Ic}) properties for primarily compression-loaded aircraft structures are the same as or less than those typically exhibited by commercially available aluminum alloys. In the preliminary screening of developmental alloys, there is no need to measure the fatigue strength or fatigue crack growth properties. The recommended minimum plane strain fracture toughness index K_{Ic} is 27.5 MPa $m^{1/2}$ (25 ksi $\sqrt{in.}$)

Appendix B
REFERENCES

1. R. E. Lewis, D. Webster, and I. G. Palmer, A Feasibility Study for Development of Structural Aluminum Alloys From Rapidly Solidified Powders for Aerospace Structural Applications, Lockheed Palo Alto Research Laboratory Final Report, Contract F33615-77-C-5186, Technical Report No. AFML-TR-78-102, Jul 1978
2. R. E. Lewis, Development of Advanced Aluminum Alloys from Rapidly Solidified Powders for Aerospace Structural Applications, Interim Technical Report for period Sep 1978 – Mar 1978, Air Force Contract F33615-78-C-5203, ARPA Order 3575, Mar 1979
3. F. R. Billman, private communication, 1978
4. B. H. Kear, P. R. Holiday, and A. R. Cox, "On the Microstructure of Rapidly Solidified IN-100 Powders," Met. Trans., Vol. 10A, Feb 1979, p. 191
5. H. Jones, Observations on a Structural Transition in Aluminum Alloys Hardened by Rapid Solidification," Mater. Sci. Eng., Vol. 5, 1969/70, p. 1
6. T. H. Sanders, Factors Influencing Fracture Toughness and Other Properties of Aluminum-Lithium Alloys, Final Report, Naval Air Development Center, Contract N-62268-76-C-0271 for Naval Air System Command, Jun 1979
7. Unpublished research, Alcoa Laboratories, Alcoa Center, PA
8. R. E. Sanders, Jr., G. J. Hildeman, and D. J. Lege, Elevated Temperature Al Alloy Development, AFML Contract F33615-77-C-5086, Technical Report for the Period Mar 29, 1978 to Mar 28, 1979
9. J. P. Hirth, "Nucleation, Undercooling and Homogeneous Structures in Rapidly Solidified Powders," Met. Trans. Vol. 9A, 1978, p. 401
10. K. Chattopadhyay and P. Ramachandrarao, "Metastable Phase Formation and Decomposition in a Rapidly Solidified Aluminum-Platinum Alloy," Mater. Sci. and Eng., Vol. 38, 1979, p. 7

11. W. B. Pearson, Handbook of Lattice Spacings and Structures of Metals, Pergamon Press, New York, 1958, p. 375

12. L. F. Mondolfo, Aluminum Alloys, Structure and Properties, Butterworths, Inc., Boston, 1976, p. 594

13. E. J. Coyne, Jr. and E. A. Starke, Jr. (unpublished research)

14. E. A. Starke, Jr., and G. Lütjering, in Fatigue and Microstructure, M. Meshii, ed., American Society for Metals, Metals Park, Ohio, 1979, p. 205

15. R. E. Sanders, Jr. and E. A. Starke, Jr., "The Effect of Intermediate Thermo-mechanical Treatments on the Fatigue Properties of a 7050 Aluminum Alloy," Met. Trans., Vol 9A, 1978, p. 1087

16. R. W. Walter, J. E. Mooney, R. A. Hamm, and R. R. June, "Wing Fuselage Critical Components Development," Boeing Co. Technical Report AFFDL-TR-78-146, Contract AFFDL-F38815-77-C-5228, Nov 1978

A-1 J. C. Ekvall, T. R. Brussat, and S. T. Chui, "Summary of 1978 Independent Research on Fracture Mechanics, Fatigue and Risk Analysis Methods," Lockheed-California Company Report, LR 28959 (to be published)

A-2 Jo Dean Morrow and T. A. Johnson, "Correlation Between Cyclic Strain Range and Low Cycle Fatigue Life of Metals," Mat. Res. and Stds., Vol. 5, No. 1, 1965, p. 30

A-3 T. R. Brussat, "An Approach to Producing the Growth to Failure of Fatigue Cracks Subjected to Arbitrary Uniaxial Cyclic Loading," ASTM STP 486, May 1971, p. 122

A-4 E. K. Walker, "The Effect of Stress Ratio During Crack Propagation and Fatigue for 2024-T3 and 7075-T6 Aluminum," ASTM STP 462, 1970, p. 1